Influence of Electrolyte on the Stability and Activity of WO_3 for Photoelectrochemical Oxidation Reactions

by

Andrew G. Breuhaus-Alvarez

A dissertation submitted in partial fulfillment
of the requirements for the degree of
Doctor of Philosophy
(Chemistry)
in the University of Michigan
2020

Doctoral Committee:

Professor Bart Bartlett, Chair
Professor Stephen Maldonado
Assistant Professor Charles McCrory
Assistant Professor Nirala Singh

Andrew G. Breuhaus-Alvarez
breuhaa@umich.edu
ORCID iD: 0000-0003-4664-6539

Dedication

To Eric Winterstein
"Carpe diem.... noctem.... whenever we're awake, really."

Acknowledgments

Thank you to my family for all of their support and love. Thank you Mom and Dad for always encouraging me and pushing me to do better. Thank you for all the opportunities I had, I definitely would not have gotten this far without you guys. Thanks to my brothers, Eric and Stephen, for your support as I pursued a science career.

Bart, huge thanks for mentoring me and giving me the chance to learn from you in your lab. You have created an environment that engourages creative ideas but also allows for challenging those ideas to ensure they are valid. The collaborative environment you have in your lab allowed me to learn not just from you, but from all the great people you took on as my fellow graduate and undergraduate researchers. Scientific communication has always been challenging for me and you were very patient and instructive as I improved my presenting and writing. Also, thank you to the rest of my committee – Professors Stephen Maldonado, Charles McCrory, and Nirala Singh. Also thanks to Professor Levi Thompson who was originally on my committee. All gave great comments and notes during my committee meetings which helped shape the overall trajectory of my thesis work.

Another major mentor in my life I need to thank is Professor John Gilbertson. Thanks DG for taking me on as an undergraduate researcher at WWU and showing me how to work in a chemistry lab. You encouraged me to go to grad school and I am very grateful that you did. Thanks to everyone from the DG lab back in the day for the memories – Zach, Ronan, Eddie, Matt, Veit, Jillian, Mayra, Yubin, Josh, Jared and others.

Thank you to everyone who I worked with in the Bartlett lab. The first Bartlett lab member I need to thank is Charles. You helped me out enormously when I first showed up and had no idea what I was doing. Thank you for being patient and making sure I actually understood what was going on as you were teaching me. Jimmy, thanks for welcoming me into the lab and for showing me around Ann Arbor when I had just moved here. Your comments and observations during my first group meetings were always helpful and I always learned something listening to you. Sam, for the very first couple days of my initial rotation in Bart's lab I was completely lost. I would come into lab, read papers but do no experiments because I didn't even know where to start. You noticed this around day three and you basically told me to find a CdS film synthesis, make it, perform an LSV in any electrolyte, and then tell you about it. That starting

point was simple but exactly what I needed and I consider that the very start of my PhD work. Aaron, thanks for being my workout buddy when I first showed up and helping me through the stresses of candidacy. Most importantly, you brought the board games for group hang out time. Adam, I am extremely lucky I got to sit next to you. I learned a lot of chemistry and experimental design just from our casual science conversations over the years. You are a great friend and were always willing to help me understand my data. You have that ability to seemingly instantly see exactly what is significant in the data, what is irrelevant, what is problematic, and how it connects with previous data. I learned a ton about experimental design from you. Asking for your opinion on data interpretation sometimes felt like I was cheating at grad school or something. John, thanks for being my friend and also #1 post doc. You were willing to help everyone in the lab with their projects and always had time to talk science. Our daily rec center breaks led to a lot of really in-depth science discussions that helped me move my work forward. To the current Bartlett lab – Nate, Kori, Brad, Christian, and Li, I'm really excited to see the work you guys are going to do. I enjoyed working with all of you and hearing about your projects but most importantly, you all were great to hang out with and I think I got incredibly lucky regarding the people I got to do my graduate work with. To Stringham, thanks for the good times getting Adam going with wacky stoires in lab and unwinding at the Blue Lep. Shobhana, thanks for your support, friendship and fun nights in Ann Arbor. Also thank you for patiently teaching rudimentary laser spectroscopy so I did not make a complete fool of myself. Josh, you were #1 undergrad researcher and were an enormous help in my thesis work. You got things done and helped reduce the grad school stress.

Table of Contents

List of Figures

List of Tables

List of Appendices

Abstract

Metal oxide semiconductors provide a platform for absorption of solar energy to generate a chemical potential gradient, driving an uphill chemical transformation in a photoelectrochemical (PEC) reaction. However, the stability of the metal oxide material is also an important consideration. In this thesis, tungsten oxide (WO_3) films were made by spin casting aqueous ammonium metatungstate solutions on fluorine tin oxide substrate. The tungsten oxide films were used to investigate water oxidation and chloride oxidation, two important reactions in solar fuel production.

WO_3 has generally been regarded as a poor choice of metal oxide light absorber for performing water oxidation due to degradation in the photocurrent density during normal operation. However in this work, electrochromic tungsten bronze impurities (H_xWO_3) were shown to oxidize during PEC water oxidation operation, resulting in a loss of donor density, causing the loss of photocurrent density observed. The regeneration of tungsten bronze donor species can induced by light in a photochromic mechanism, resulting in a recovery in the photocurrent density and demonstrates that photocurrent density loss during water oxidation is reversible. The rate of water oxidation was determined by detecting oxygen gas, the product of water oxidation, with flow cell gas chromatography. After photochromic regeneration of tungsten bronze donors, the rate of water oxidation recovered alongside the overall photocurrent. Because of the importance of tungsten bronze species in the PEC behavior of tungsten oxide, it is referred to as H_xWO_3 in the thesis chapters to better describe the material used.

Tungsten bronze donor species are electrochemically active and suppressing the rate of donor oxidation will increase the stability in PEC photocurrent. To this end, chloride oxidation was explored as a possible alternative to water oxidation for solar fuel formation. Improvement in PEC photocurrent stability was observed in 0.5 M sodium

chloride electrolytes compared to 0.1 M potassium phosphate electrolytes at the same pH. Chloride more rapidly injects electrons into the H_xWO_3 material, eliminating photogenerated holes before oxidation of tungsten bronze impurities can occur. The oxidation of donors was also prevented by applying an FeOOH electrocatalyst to the surface of the H_xWO_3 because the electronic states of FeOOH are well positioned to inject electron density into H_xWO_3, similar to chloride oxidation. Using chloride electrolytes with H_xWO_3 materials leads to higher stability in the photocurrent density during solar fuel producing reactions.

The hypochlorous acid produced by H_xWO_3 is a strong oxidant capable of performing many useful chemical transformations. The oxidation of aqueous primary and secondary alcohols was investigated using ethanol and 2-propanol and 1 M chloride electrolytes. The yield was monitored using ^{1}H-NMR. The yield of products was high for both ethanol and 2-propanol. Proton activity influenced the yield of acetic acid and acetone, but no influence was observed in the acetaldehyde yield. Because hypochlorous acid undergoes light induced homolytic cleavage, generating radical species, alcohol oxidation was also performed using a platinum electrode in the same electrolyte. Comparing the product yield of alcohol oxidation using platinum in the dark and under illumination, only the acetaldehyde yield exhibited a dependence on the illumination with no difference observed in the acetic acid and acetone yields. These observations were used to rationalize the mechanism of hypochlorous oxidation for the observed products.

Chapter 1.

Introduction

1.1. Current Energy Consumption Practices are Unsustainable With Current Energy Sources

Organic fuel sources found on Earth and used in human activity originated from terrestrial photosynthesizing organisms collecting diffuse solar radiation and using that energy to form chemical bonds to create energy stores such as sugars. This chemical energy is distributed throughout the biosphere and the result is the storage of solar energy in the Earths biomass. Chemical potential energy can be found in decomposed biomass, such as in petroleum and coal which formed over hundreds of millions of years, or in living biomass like forests, crops, livestock, and other living organisms.[1,2] The planet is essentially a battery that had been slowly charged by the sun, storing photon energy in bonds as chemical potential energy, but human activity is depleting that store of energy at an unsustainable rate.

The Earths total chemical energy reservoir is approximately $2,000$ ZJ, but only an approximate 40 ZJ is actually usable chemical potential energy because many fuel deposits are dispersed or inaccessible, preventing a net energy gain.[2,3] The 2019 world population was 7.7 billion people and the worldwide average per capita energy consumption rate for the same year was $7.6 \cdot 10^{10}$ J$\cdot$(person$\cdot$year)$^{-1}$.[4] This results in a worldwide yearly energy consumption rate of approximately 0.59 ZJ per year (19 TW) which means that 1.5% of currently remaining fossil fuel stores will be consumed annually if all human energy needs are met by fossil fuels only and energy consumption rates are static. Oil, coal, and natural gas sources provided at least 85% of human energy needs during 2019, human population growth follows near-exponential behavior, and per capita energy consump-

tion in developing countries is expected to increase as their economies grow, indicating that investing in alternative energy technologies will be required just to maintain the current standard of living in the first-world, let alone achieve growth.[2,4,5] Unchecked, the consequences of the over reliance on fossil fuels will be felt by those living today because the negative environmental and economic effects from fuel scarcity will be felt long before fuel stores are completely consumed.[2]

1.2. Alternative Energy Sources

1.2.1. Nuclear Energy

500 ZJ of recoverable nuclear potential energy exists on Earth and is an even larger reservoir of energy than chemical energy.[2] While a much larger store of energy, nuclear potential energy lacks the flexibility of chemical potential energy, preventing scale-up to the global level in order to meet the current 19 TW rate of worldwide energy consumption.[6] In order to completely meet the 19 TW required for current energy consumption rates, more than $15,000$ nuclear reactors would need to be constructed, a sizable increase from the 440 currently operational.[6] Nuclear reactors require about 20.5 km^2 of land to encompass the power station, exclusion zone, enrichment plant, ore processing, and support infrastructure which must be away from population centers and near a large body of freshwater for coolant requirements.[6,7] Finding $15,000$ sites around the world which satisfy operational and safety requirements is a challenging task and the land may be unavailable for centuries in the case of an accident.[6] Furthermore, the lifetime of a nuclear reactor is 50-60 years due to neutron embrittlement, which means that with $15,000$ nuclear reactors, one site would need to be built while another is decommissioned every day, an unrealistic undertaking considering construction takes 6-12 years and decommission takes 20-50 years.[6,8,9] Implementation of nuclear technology also faces strong public opposition, due to fears from infamous accidents such as Chernobyl and Fukushima, their link with nuclear weapons, and the distrust of nuclear materials which represent a hazardous risk that a person "could not see, touch, taste, or smell."[10,11] The resource cost and public distrust has led to the slow adoption of nuclear energy sources. As of 2019, only 4.3% of worldwide energy consumption needs is met by nuclear energy.[4]

1.2.2. Solar Energy

Solar energy is a continuous source of renewable energy. 120 PW, or $1.2 \cdot 10^5$ TW, of solar energy strikes the Earth's surface, on average.[12] The Sun provides approximately $6,000$ times our current 19 TW energy needs, but contributed only 1.1% to worldwide energy production in 2019.[4] The 120 PW of solar energy is, of course, the upper limit of power that could be sourced from the sun because sunlight is dispersed spatially over the Earth's surface. Furthermore, our day-night cycle restricts solar energy collection to periodic intervals. Despite these limitations, solar energy remains an extremely promising energy source with the proof-of-concept being the planet Earth's entire biosphere.

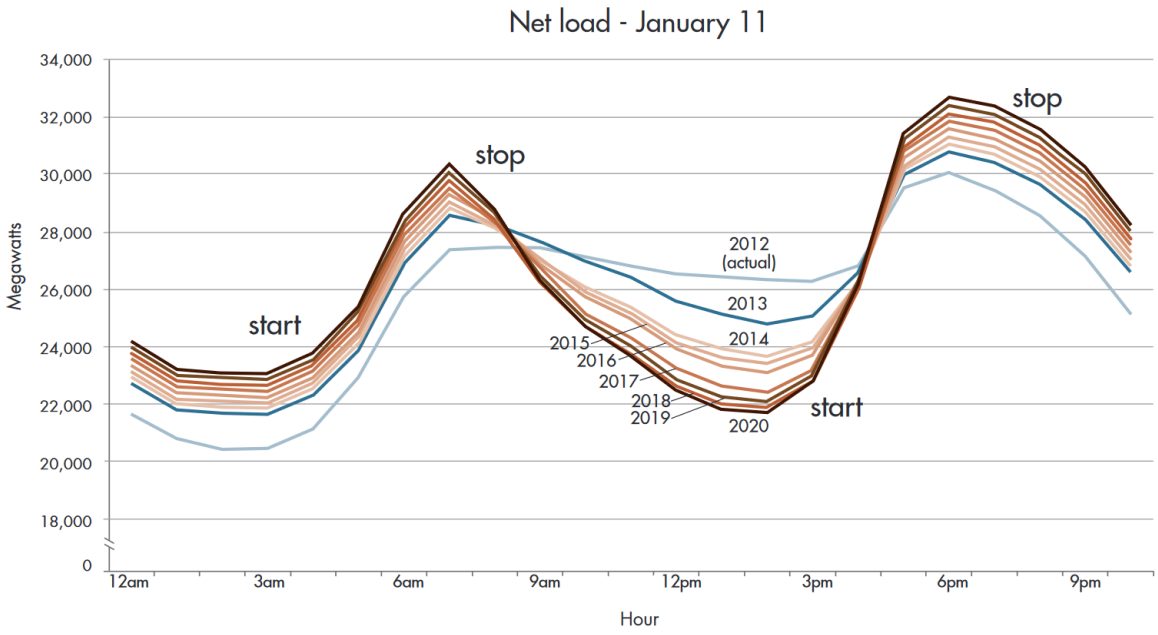

Figure 1.1: The net load on the California grid on January 11 for years 2012 through 2020. Solar energy sources suppress grid load during the day, but energy needs after the sun sets rapidly increases grid load. Reproduced from ref. 12

The consequence of periodic intervals of energy collection is shown in Figure 1.1 where the net load on the California energy grid on January 11$^{\text{th}}$ is tracked throughout the day for years 2012 through 2020. This plot is referred to as the duck curve. The "start" and "stop" of high energy production intervals are labeled on the figure. Increased production of energy is required during these intervals to meet rapid changes in grid

load. At 4:00 a.m., grid load begins to increase as people wake up and an increase of about $8,000$ MW is observed until 7:00 a.m. when collection of solar energy by photovoltaics begins becoming effective. This produces the depression in the grid load that extends between 7:00 a.m. and 4:00 p.m., at which point the grid begins to uptick. At 4:00 p.m., solar energy production is decreasing but people are still awake, leading to a rise by about $11,000$ MW of grid load until 6:00 p.m. when grid load begins trending to zero load until the cycle starts again. The "belly" of the duck curve in Figure 1.1 is projected to grow steadily through 2020 due to increased integration of solar technologies and the peak at 9:00 p.m. will also grow due to an increase in population, two features which increase the rate of ramp up in the grid load. Figure 1.1 illustrates how the periodic nature of sunlight prevents the overlap of solar energy collection with energy use. Seasonal changes in solar flux further complicate the issue. Effectively using solar energy to meet energy requires using an energy storage medium during periods of high solar flux for use during periods of high load and low solar flux.

1.3. Solar Fuel is Solar Energy Captured as Chemical Potential Energy

1.3.1. Forming Chemical Fuel Species

Chemical potential energy is stored during endergonic reactions due to the increase in free energy that occurs.

$$\mathrm{A} + \mathrm{B} \longrightarrow \mathrm{C} + \mathrm{D} \qquad\qquad \Delta G > 0 \tag{1.1}$$

In Figure 1.2, the formation of higher energy chemical species C and D from lower energy chemical species A and B is shown in a reaction coordinate diagram. In addition to the energy required to increase the chemical potential from the initial state to the final state (ΔG), additional energy must be expended to accommodate the formation of a transition state, represented by $\Delta G^{\ddagger}$. The height of the $\Delta G^{\ddagger}$ barrier in the reaction coordinate diagram affects the rate of the reaction. The barrier can be lowered by a catalyst, which is a substance that changes the reaction pathway used to convert A + B to C + D. This is demonstrated in the reaction coordinate diagram by the red trace.

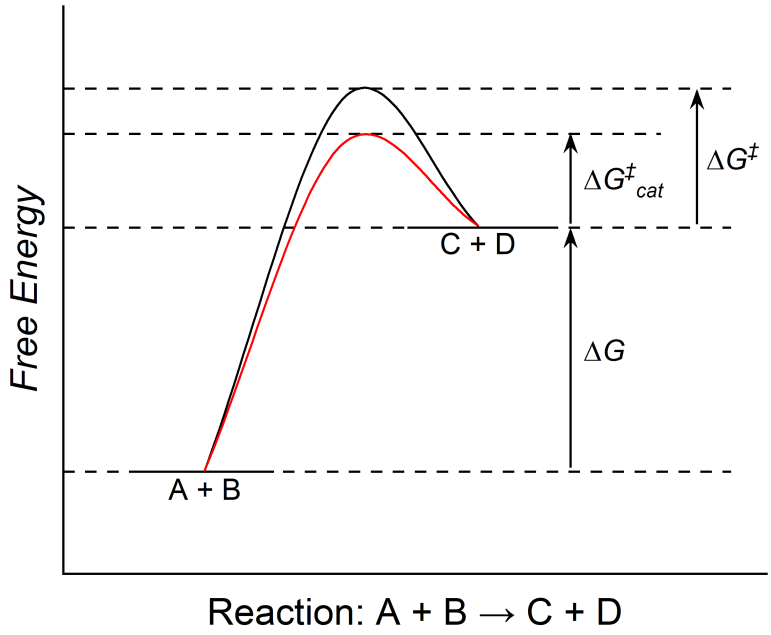

Figure 1.2: Reaction coordinate diagram demonstrating the change in free energy during an endergonic reaction. The red trace depicts a catalyzed reaction, resulting in a lower transition state energy given by $\Delta G^{\ddagger}_{\text{cat}}$.

During the reaction, the catalyst participates in a repeated cycle of elementary steps and the catalyst is regenerated at the end of each cycle.[13,14] The catalyst is unchanged by the overall reaction. The new set of elementary steps introduced by the catalyst lowers the $\Delta G^{\ddagger}$ barrier for the reaction ($\Delta G^{\ddagger}_{\text{cat}} < \Delta G^{\ddagger}$), increasing the rate of the reaction. To release the stored energy, the reaction would be reversed ($\text{C} + \text{D} \longrightarrow \text{A} + \text{B}$, $\Delta G_{\text{reverse}} = -\Delta G$) and the maximum non-expansion work that could be extracted would be $w = (\Delta G_{\text{reverse}} + \Delta G^{\ddagger}_{\text{reverse}})$.

1.3.2. Water and Chloride Represent Substrate With Low Environmental Impact

Due to the enormous and ever increasing energy consumption rates of human activity, any fuel producing reaction must be as environmentally benign as possible to minimize ecological damage due to the volume of production that will be required. The task of maintaining a sustainable society requires "*meeting the needs of the present generation*

without compromising the ability of future generations to meet their own needs."[15] With this is mind, two possible fuel generating reactions become particularly viable due to the chemical make up of our planet. The oceans contain a large quantities of water and chloride. Both of these can be used in endergonic chemical reactions to produce hydrogen gas, a fuel product.

$$2\,H_2O\,(l) \longrightarrow O_2(g) + 2\,H_2(g) \qquad \text{water splitting} \qquad (1.2)$$

$$2\,H_2O\,(l) + 2\,Cl^-(aq) \longrightarrow 2\,OH^-(aq) + Cl_2(g) + H_2(g) \qquad \text{chloralkali} \qquad (1.3)$$

Equation 1.2 is the water splitting reaction, and results in oxygen as a benign by-product. While environmental impact of gaseous oxygen is not severe, it is also not a particularly valuable product. In the chloralkali process described in Equation 1.3, hydrogen gas is produced alongside chlorine gas, which is a much more commercially valuable product than oxygen gas.[16,17]

Both the water splitting and chloralkali reactions are endergonic reactions, requiring an input of energy to drive the reaction forward. This can be done with an applied electrical potential using electrodes in an electrochemical cell. Using the chloralkali reaction as an example:

$$2\,Cl^-(aq) \longrightarrow Cl_2(g) + 2\,e^- \qquad E^\circ = 1.36 \text{ V vs NHE} \qquad \text{anode} \qquad (1.4)$$

$$2\,H^+(aq) + 2\,e^- \longrightarrow H_2(g) \qquad E^\circ = 0.00 \text{ V vs NHE} \qquad \text{cathode} \qquad (1.5)$$

$$2\,Cl^-(aq) + 2\,H^+(aq) \longrightarrow Cl_2(g) + H_2(g) \qquad E_{cell} = -1.36 \text{ V} \qquad \text{net} \qquad (1.6)$$

Equation 1.4 describes the oxidation of chloride at the anode to liberate chlorine gas and electrons. The electromotive force (emf) of the cell reaction is $E_{cell} = -1.36$ V and this value is assigned to the reaction as written in Equation 1.6. The cell reaction emf is the electrostatic potential of the cathode reaction with respect to the anode reaction, i.e. the reduction potential of the reaction occurring at the cathode minus the reduction potential of the reaction occurring at the anode. The emf is then directional and means that the reverse of Equation 1.6 ($Cl_2(g) + H_2(g) \longrightarrow 2\,Cl^-(aq) + 2\,H^+(aq)$) has an emf of $E_{cell} = 1.36$ V. The primary function of chloride oxidation in the overall energy generating scheme is to extract electrons. These electrons are then used in the

hydrogen evolution reaction (HER) occurring at the cathode, described by Equation 1.5, resulting in the generation of hydrogen gas. The net reaction given by Equation 1.6 is the chloralkali process in acid. The set of equations indicate that in a pH 0 aqueous solution, poising an ideal anode 1.36 V more positive than an ideal cathode will drive Equation 1.6. A real set of electrode materials will not be able to produce chlorine and hydrogen gas with exactly 1.36 V applied because of the extra energy required due to $\Delta G^{\ddagger}$ (Figure 1.2). The extra amount of potential that must be applied across the electrodes to supply this energy is the overpotential.

Instead of chloride oxidation, water oxidation may be performed to produce hydrogen gas in a similar way.

$$\mathrm{H_2O\,(l)} \longrightarrow \tfrac{1}{2}\mathrm{O_2(g)} + 2\,\mathrm{H^+(aq)} + 2\,\mathrm{e^-} \qquad E^\circ = 1.23\ \mathrm{V} \qquad \text{anode} \tag{1.7}$$

$$\begin{array}{lll} 2\,\mathrm{H^+(aq)} + 2\,\mathrm{e^-} \longrightarrow \mathrm{H_2(g)} & E^\circ = 0.00\ \mathrm{V\ vs\ NHE} & \text{cathode} \\ \hline \mathrm{H_2O\,(l)} \longrightarrow \tfrac{1}{2}\mathrm{O_2(g)} + \mathrm{H_2(g)} & E_{\mathrm{cell}} = -1.23\ \mathrm{V} & \text{net} \end{array} \tag{1.8}$$

In Equation 1.7, the oxidation of water at the anode is the oxygen evolution reaction (OER). The electrons which are produced at the anode during OER are used in Equation 1.5, HER, producing the solar fuel. The emf of the cell reaction is $E_{\mathrm{cell}} = -1.23$ V, so the ideal anode and cathode would need 1.23 V applied between them in a pH 0 solution to drive Equation 1.8. Storing photon energy in chemical bonds requires materials which can convert light into the electrochemical energy gradient required to drive the reaction with the lowest possible overpotential ($\Delta G^{\ddagger}$).

In Figure 1.3, the relationship between free energy and the reduction potentials of the reactions relevant to our fuel forming reactions is displayed. The cell potential for water splitting and the chloralkali reaction gives the energy stored in the product species. The free energy change in an electrochemical reaction at standard conditions can be computed from

$$\Delta G = -nFE_{\mathrm{cell}} \quad (\mathrm{kJ \cdot mole^{-1}}) \tag{1.9}$$

Where n is the number of electrons transferred in the reaction, $F = 96,485 \frac{\text{C}}{\text{mole e}^-}$ is Faraday's constant, and E_{cell} is the cell reaction emf. A non-spontaneous, endergonic reaction has a positive ΔG and a negative E_{cell}. A spontaneous, exergonic reaction has a negative ΔG and a positive E_{cell}. The production of solar fuel constitutes the non-spontaneous, endergonic reaction while the consumption of solar fuel constitutes the spontaneous, exergonic reaction. The plot in Figure 1.3 displays the potential energy of electrons. Forming a fuel species requires expending energy to move electron density from low energy configurations, such as in water or chloride anions, to the higher energy configuration in hydrogen bonds. When forming hydrogen with water splitting, water oxidation occurs (Eqn. 1.7: $\text{H}_2\text{O} \longrightarrow \frac{1}{2}\text{O}_2 + 2\,\text{H}^+ + 2\,\text{e}^-$), liberating protons into solution and producing the electrons which are used to perform proton reduction (Eqn. 1.5: $2\,\text{H}^+ + 2\,\text{e}^- \longrightarrow \text{H}_2$). Together, these reactions constitute the overall water splitting reaction, resulting in the production of O_2 at the anode and H_2 at the cathode at the cost of energy. To extract the stored free energy, the reactions are reversed. Hydrogen gas is spontaneously oxidized at the anode creating protons in solution and electrons which are collected by the electrode. The electrons from the oxidation of hydrogen are

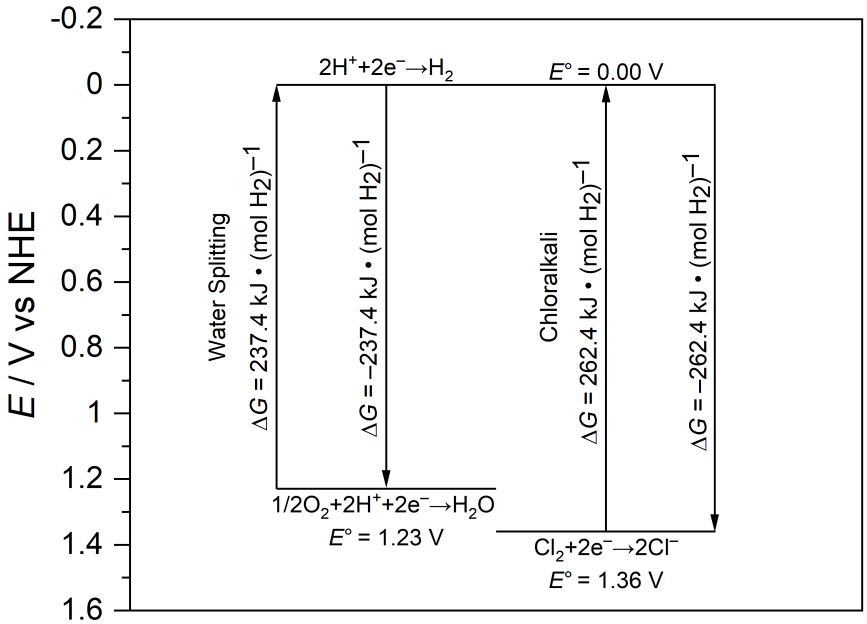

Figure 1.3: Energy diagram displaying the difference between reduction potentials relevant for HER production. Proton, oxygen, and chlorine reduction potentials are shown.

collected by the anode to be used in the spontaneous reduction of O_2 at the cathode. The electrons travel from the anode through an external circuit performing 237.4 kJ of work per mole of hydrogen oxidized as they travel to the cathode, minus efficiency losses such as $\Delta G^{\ddagger}$ for hydrogen oxidation and oxygen reduction. A similar process occurs when using the chloralkali reaction for energy storage. In this case, energy storage occurs when Cl^- is oxidized (Eqn. 1.4: $2\,Cl^- \longrightarrow Cl_2 + 2\,e^-$) at the anode and the collected electrons are used to perform proton reduction at the cathode. When energy is to be released, the chloralkali reaction runs in reverse. Hydrogen is oxidized spontaneously at the anode and the electrons from oxidation are collected by the anode and perform 262.4 kJ of work per mole of hydrogen oxidized as they travel through the external circuit to perform chlorine reduction at the cathode.

1.3.3. Performing Endergonic Reactions With Semiconductor Photocatalysts

A number of solar energy storage methods exists such as using photovoltaics to energize conventional storage media like batteries and flywheels.[5] A comparison of their viability is beyond the scope of this document. This work strictly pertains to the use of metal oxide semiconductors to absorb light in order to directly perform endergonic chemical reactions used in solar fuel production.

Metal oxides such as $WO_3, CuWO_4, Fe_2O_3,$ and $BiVO_4$ are examples of visible light absorbers used in photoelectrochemical research.[19] The absorption of solar energy by metal oxide semiconductors is made possible by the valence band (VB) and conduction band (CB) of the materials. Metal oxide solids are composed of a series of repeating units and as the number of discrete atomic orbitals grows to the macro level ($\approx 10^{23}$), a continuum of states begins to form as a band.[20] This is illustrated in Figure 1.4 using ethylene as a simple model.[18] In this example, symmetry allowed mixing of molecular orbitals as ethylene units co-facially agglomerate produces the states which make up the bands. The VB is the highest energy band with electron density and is analogous to the HOMO of a molecule. The CB of a solid is comprised of empty states, analogous to the LUMO of molecule. In semiconductors, the valence band is filled and the next available states for placing electron density are in conduction band or donor states.

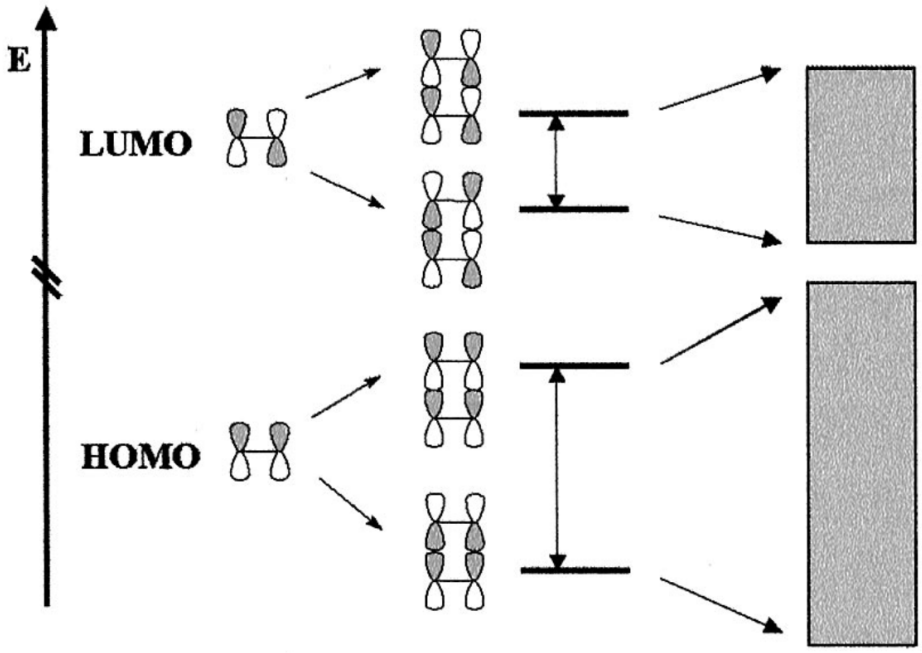

Figure 1.4: The bonding-antibonding interaction of HOMO/LUMO molecular orbitals between a growing number of ethylene units leads to bands of states. Reproduced from reference 18. Copyright (2002) National Academy of Sciences

In Figure 1.5a, the Fermi level is shown for an intrinsic semiconductor. An intrinsic semiconductor is not doped, but possess a fully filled valence band and a bandgap within the visible region. The Fermi level E_{F} gives a measure of the average electrochemical potential of electrons in the semiconductor. There is a 50% chance that this energy level would be occupied at any given time. This probability is given by the black trace in Figure 1.5a, which is a plot of $f(E)$, the Fermi distribution, over the CB and VB of an intrinsic semiconductor. The horizontal dashed line denotes the Fermi level in the middle of the bandgap. However, although $f(E)$ is non-zero within the bandgap, the density of states (DoS), $\rho(E)$, is zero in the bandgap in accordance with the definition of the bandgap. The electron population, $N(E)$, is the product of the fermi distribution and the DoS, which is zero within the bandgap.

$$N(E)dE = f(E) \cdot \rho(E)dE \tag{1.10}$$

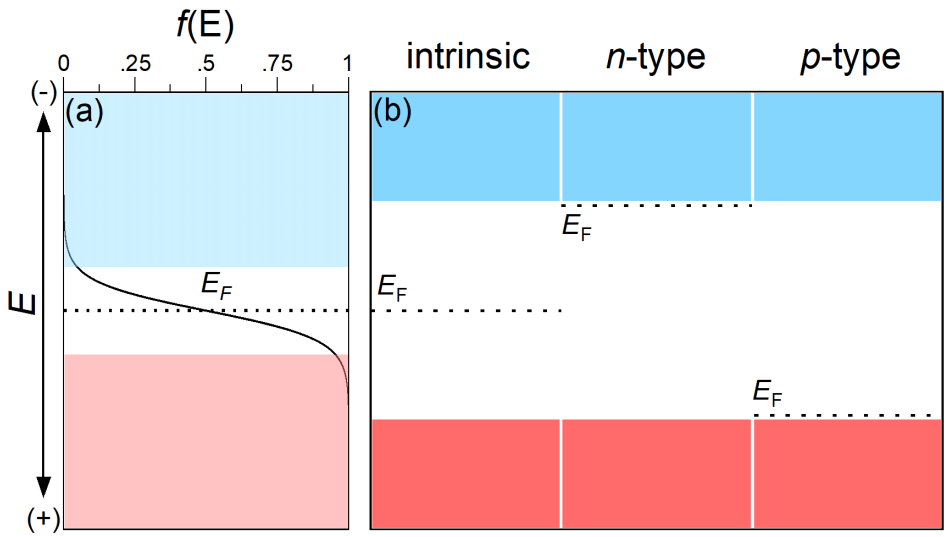

Figure 1.5: The Fermi function, $f(\mathrm{E})$, is plotted (a) for an intrinsic semiconductor, displaying the conduction band and valence band relative to the Fermi level of the semiconductor. The Fermi level, E_{F}, of (b) an intrinsic, n-type, and p-type semiconductor relative to the conduction and valence bands.

Also shown in Figure 1.5b is the band diagram of n-type and p-type semiconductors shown alongside an intrinsic semiconductor. An n-type semiconductor is formed by incorporating a minute amount (ppb) of electron donors into the material. this addition of electron density shifts the Fermi level to more negative potentials. In the case of p-type semiconductors, a minute amount of hole donors are added to the the Fermi level to more positive potentials. Silicon is an example of an intrinsic semiconductor and can be made n-type by doping phosphorus. Phosphorus (Group V) possesses one additional electron relative to the host silicon (Group IV). This additional electron constitutes the donor electron when phosphorus is incorporated into the silicon lattice, substituting in a minute amount of silicon sites. Silicon can be made p-type in an analogous manner using a Group III donor. For example, gallium (Group III) has one less electron than the host silicon and gallium sites will contain an absence of electron density, called a hole. The donor level is such that the Fermi level is within $k_B T$ of the CB or VB in the case of n-type or p-type respectively, where k_B is the Boltzmann constant and T is temperature. The result is that an appreciable amount of donors are ionized at ambient temperature, generating charge carriers. In n-type semiconductors, the majority charge carriers are electrons and in p-type, the majority charge carriers are holes. Illumination

causes an inversion in the identity of the majority carrier, and holes suddenly become the majority charge carrier in n-type materials upon illumination. The holes generated in illuminated n-type semiconductors make them well suited for performing oxidative reactions.

Between the conduction and valence band is a gap in energy where no states are predicted to exist. The energy gap between the CB and VB affects the minimum photon energy that may be absorbed. An electron in the VB may be raised in energy to the CB only if a photon with enough energy to traverse the energy gap is absorbed. The electrochemical reactions that can be driven by the metal oxide are dictated by the positions of the VB and CB on the potential energy scale. Figure 1.6 demonstrates

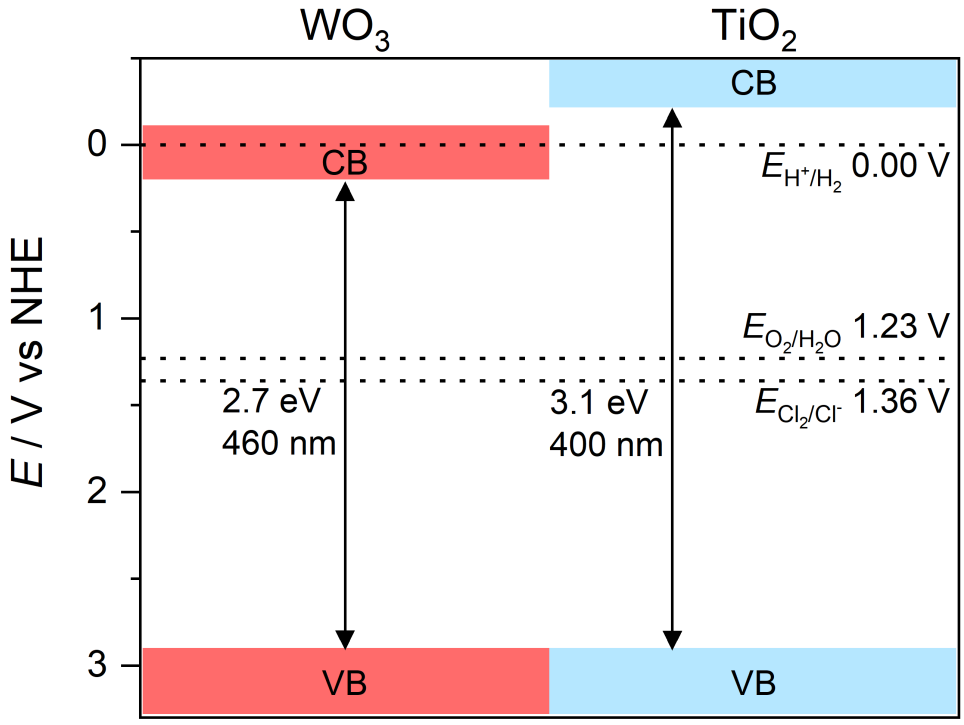

Figure 1.6: Band diagram depicting the valence and conduction band positions of WO_3 and TiO_2 relative to the reduction potentials relevant to water splitting and the chloralkali process. The band gap, E_{bg}, is also shown for both materials.

this relationship using WO_3 and TiO_2 as examples. The potential difference between the VB and CB of TiO_2 is greater than the potential difference in WO_3. The result is TiO_2 light absorption occurs in the UV region while WO_3 is able to absorb a greater

portion of solar flux because the WO_3 band gap is 460 nm, in the visible region. If an electron is promoted to the CB by photon energy, a hole will be left behind in the VB. Because the VB of both WO_3 and TiO_2 are both more positive than the reduction potential of O_2 and Cl_2, a photogenerated hole in their VB can reverse both reactions through the corresponding oxidation reactions. Electron density will be removed from water or chloride anion to eliminate the hole by the semiconducting materials, oxidizing the substrate and generating either O_2 (Eqn. 1.7) or Cl_2 (Eqn. 1.4). In the case of TiO_2 the electron promoted to the CB is at a more negative potential than the reduction of protons to hydrogen, and so a CB electron in TiO_2 is thermodynamically capable of performing HER when transferred to the cathode to complete the fuel forming reaction. From the band positioning of TiO_2, only UV light is required to produce solar fuel. In the case of WO_3 however, an electron at the CB edge is more positive than the proton reduction potential. Additional energy input is required to meet the free energy change needed to perform HER at the cathode. Both metal oxides function to photocatalyze the fuel forming reactions. In the appropriate conditions, illuminating the metal oxides converts photon energy to electrochemical potential and increases the rate of solar fuel production.

1.4. Prior Work In Solar Fuel Production Using Tungsten Oxide Materials

A number of mechanisms can introduce dopant species into a semiconductor. CdTe can be made *n*-type or *p*-type by introducing non-stoichiometry in the composition. A slight excess of Cd results in an *n*-type and a slight excess of Te results in *p*-type due to charge compensation for the non-stoichiometry.[21] In metal oxides, non-stoichiometry occurs due to oxygen vacancies.[22] This results in a reduction in the oxidation state of the counter-balancing cations. In tungsten oxide, perfectly stoichiometric WO_3 would contain only W^{6+}. However, a missing oxygen in the lattice constitutes an oxygen vacancy. The loss of O^{2-} must be charge compensated, resulting in two W^{5+} for every vacant oxygen site. Oxygen vacancies can be increased by forming the metal oxide in high temperature and low O_2 partial pressure.[22] Because this work uses tungsten oxide as the metal oxide light absorber in the bulk of the presented data, the purpose of this

section is to discuss prior work in the literature with respect to solar fuel production by tungsten oxide.

1.4.1. Water Oxidation Using Tungsten Oxide

Tungsten oxide was first noted as a potential light absorber for solar fuel reactions in 1976, shortly after the initial demonstration of light driven photoelectrolysis of water using TiO_2 by Fujishima and Honda in 1972.[23,24] The 2.7 eV bandgap of WO_3 made the material attractive over other water oxidation photocatalysts that were known at that point(TiO_2, $SrTiO_3$, $BaTiO_3$, and SnO_2).[24–27] Of these examples, the TiO_2 bandgap is closest in energy (3.1 eV) to WO_3 and only 4% of the solar spectrum energy may be used due to the wide bandgap. The 2.7 eV bandgap of WO_3 is smaller and allows for absorption of lower energy photons. This allows for 12% of the solar spectrum energy to be directed towards solar fuel production by WO_3.

The valence band maximum (VBM) of monoclinic WO_3 is 2.9 V vs NHE and places the conduction band minimum (CBM) at 0.2 V vs NHE.[28] A VBM of 2.9 V vs NHE is substantial considering the O_2, H^+/H_2O reduction potential lies at 1.23 V vs NHE (Equation 1.7). However, reports of WO_3 degrading dissolved organic pollutants by reactive hydroxyl radical species in the literature indicates that discussing water oxidation on WO_3 only in terms of the oxygen reduction potential is not sufficient to fully describe the chemistry occuring.[29–33] WO_3/Pt particles were shown to photocatalytically oxidize aqueous benzene to phenol. The WO_3/Pt particles generated hydroxyl radical selectively from the oxidation of water which subsequently reacted chemically with the dissolved benzene.[33] The hydroxyl radical based mechanism was supported by ^{18}O-labelled H_2O and O_2 experiments. No evidence of direct benzene oxidation by the WO_3/Pt particles was observed. In comparison, TiO_2 particles demonstrated complete oxidation of benzene to CO_2 due to strong adsorption of benzene to the TiO_2 surface which facillitated direct oxidation by TiO_2 photogenerated holes. Whether hydroxyl radical production is a minor parasitic reaction or the predominate pathway during the oxygen evolution on WO_3 is currently not certain. The use of a coumarin fluorescent radical trap was used to demonstrate the suppression of hydroxyl radical production

by application of an FeOOH electrocatalyst to the WO_3 material (WO_3|FeOOH).[34] In addition, the Tafel slope of WO_3 in potassium phosphate electrolyte was measured to be 251 ± 16 mV $\cdot$ dec^{-1} at the foot of the wave and the Tafel slope of WO_3|FeOOH was significantly lower at 82 ± 14 mV $\cdot$ dec^{-1}. Both the loss of hydroxyl radical and large shift in Tafel slope are correlated, suggesting that the oxidation of water to hydroxyl radical is not a minor reaction pathway during water oxidation by WO_3 surfaces. These results imply that when using WO_3 in solar fuel generation, the $OH^{\bullet}$, H^+/H_2O reduction potential must be considered.[35]

$$H_2O\,(l) \longrightarrow OH^{\bullet}(aq) + H^+(aq) + e^- \qquad E^\circ = 2.7 \text{ V vs RHE} \tag{1.11}$$

In Figure 1.7, the hydroxyl radical reduction potential is only 0.2 V more negative than the VBM of WO_3, resulting in substantially less overpotential for valence band holes compared to the 1.67 V overpotential implied by the oxygen reduction potential (Equation 1.7). The advantage of wide bandgap semiconductors is that the valence band is generally very positive and valence band holes drive chemical transformations with high

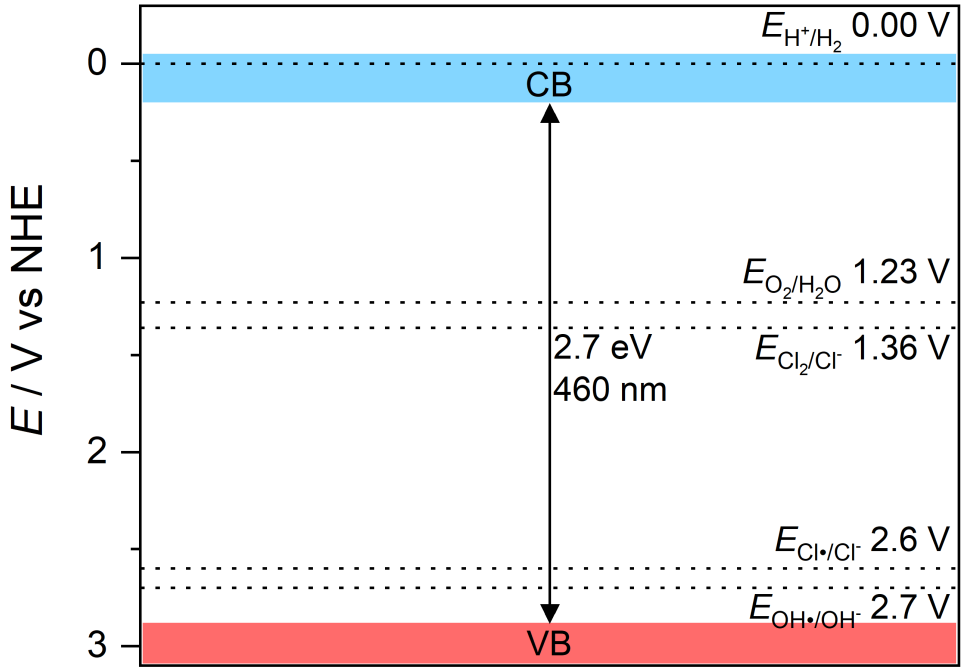

Figure 1.7: The band diagram of WO_3 with the relevant reduction potentials for solar fuel reactions.

overpotential. It is generally assumed that the large overpotential means the reaction kinetics at the electrode are not rate limiting for most reactions and only the light absorption and electron-hole mobility characteristics of the semiconductor need to be considered.[36] But if the formation of hydroxyl radicals formation is substantial on WO_3 surfaces, then reaction kinetics may be an important consideration in charge transfer between solution species and the WO_3 electrode.

Because WO_3 bandgap is 2.7 eV, only 12% of solar energy may be absorbed. Another drawback for WO_3 is the position of the CBM at 0.2 V vs NHE. WO_3 cannot perform the full solar fuel reaction as the CBM is more positive than the hydrogen reduction potential (Equation 1.5). Efforts have been made to augment the electronic structure of WO_3 by doping or structural modifications to make the CBM more negative than the hydrogen reduction potential and to raise the VBM in order to make the bandgap less than 2.7 eV.[28,37–42] The goal is create a material that may reduce protons with photogenerated CB electrons and also absorb a greater percentage of solar energy. However, if hydroxyl radical is a major reaction pathway in the oxidation of water on WO_3 surfaces, then raising the VBM could lower the overall rate of water oxidation despite an increase in the fraction of solar energy absorbed. If the VBM is raised but the mechanism of water oxidation is unchanged, the overall rate of oxidation will drop once the VBM becomes more negative than the hydroxyl radical reduction potential because there will be no thermodynamic driving force from the valence band holes to drive the water oxidation reaction pathway on WO_3. To get around this, an electrocatalyst such as FeOOH will be required in addition to electronic state augmentation to provide a hydroxyl free reaction pathway for charge transfer.

1.4.2. Chloride Oxidation Using Tungsten Oxide

While the body of work covering water oxidation with WO_3 is more extensive, examples of chloride oxidation by WO_3 exist in the literature. The faradaic efficiency for chloride oxidation varies widely, with examples from 30-100% in chloride containing electrolytes.[17,43–45] An increase in photocurrent stability is noted with chloride electrolytes and rationalized by the suppression of peroxide species being formed during

chloride oxidation.[44]

1.4.3. Tungsten Oxide Electrochromism

It is interesting to note that in the original WO_3 report, the electrochemical formation of hydrogen tungsten bronze was noted during cyclic voltammograms.

$$WO_3 + H^+ + e^- \longrightarrow HWO_3 \tag{1.12}$$

This is the electrochromic formation of tungten bronze. W^{+6} was reduced to W^{+5} alongside the intercalation of a proton to charge balance. In this example, the cation is a proton to form the hydrogen tungsten bronze but bronzes can be made with other Group I cations. In the original WO_3 report, no consideration was given towards the effect of the reduction of tungsten on the photoelectrochemical oxidation of aqueous substrates. However, x-ray photoelectron spectroscopy (XPS) experiments have demonstrated that the electronic strucutre and behavior of tungsten oxide can be modulated by different values of x for M_xWO_3, $0 \leq x \leq 1$.[46–50] Valence band XPS spectra are shown in Figure 1.8 and illustrate the this phenomena using hydrogen, lithium and sodium tungsten bronze.[46] In Figure 1.8a, the VB XPS of clean WO_3 is shown alongside VB XPS spectra of H_xWO_3 for $x = 0.3$ and $x = 0.5$. The VB of WO_3 can be seen clearly as the broad signal from 12 eV to about 2.7 eV binding energy. The VB XPS signal goes to zero at a binding energy of about 2.7 eV positive of the Fermi level and illustrates the bandgap between the CBM and the VBM. When H_xWO_3 is formed for $x = 0.3$, a correlated increase in the VB XPS signal at the Fermi level occurs due to an increase in the DoS at that energy. The electron density which enters the tungsten oxide material due to Equation 1.12 is placed into near the CBM, suggesting a doping mechanism for the metal oxide semiconductor. As the value of x increases, the tungsten bronze undergoes structural phase transitions. For $x \approx 0$, the tungsten oxide structure is monoclinic.[47] As x increases, the structure shifts to an orthorhombic structure for $0 < x < 0.05$ which then transitions to a tetragonal phase for $0.05 \leq x < 0.5$ and then finally the cubic perovskite phase for $x \geq 0.5$.[46,47] In Figure 1.8b, the VB XPS of lithium and sodium tungsten bronzes are shown. What is notable is that although different cations are used and different crystal phases are present, the overall electronic structure is preserved. The major difference between the spectra in Figure 1.8b is the increase in the DoS at the

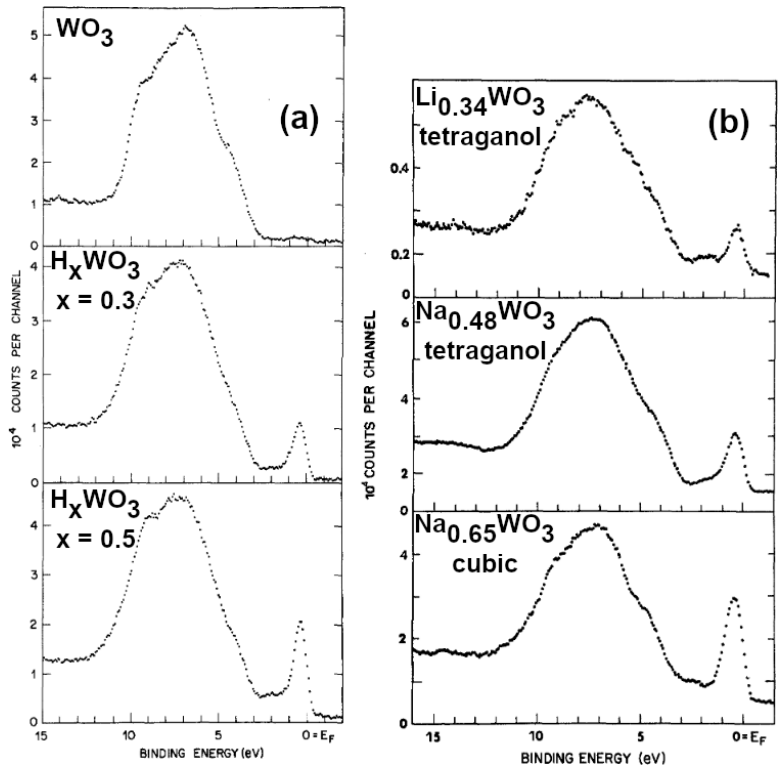

Figure 1.8: Valence band XPS of WO_3 and H_xWO_3 films (a) grown on a W substrate. The value of x is estimated from the conduction band peak area. Also shown are lithium and sodium tungsten bronze valence band XPS (b) of increasing values of x. Adapted with permission from Ref. 46

Fermi energy as x increases. The atomic orbitals of the Group I cation intercalated into the tungsten oxide do not factor into CB or VB considerations. In the case of sodium tungsten bronze, the sodium orbitals do not contribute to bonding because their energies lie approximately 12 eV above the Fermi level.[47] The extra electron density enters t_2g states and results in the sodium being fully ionized.[47] Tungsten oxide bronzes maintain their semiconducting character until the material is approximately 25% reduced ($xM^+ + WO_3 \longrightarrow M_xWO_3$, M = Group I cation, x = 0.25) at which point the material becomes metallic.[47,51–54]

A general feature in the photocurrent traces obtained during water oxidation when using tungsten oxide light absorbers is the steady loss of photocurrent during water oxidation.[17,45] The mechanism of degradation was uncertain, but proposed as being

caused by the accumulation of peroxide species on the surface of WO_3 during water oxidation, forming a blocking layer and inhibiting charge transfer.[44,55] Also proposed is the simple dissolution of WO_3 by the peroxide intermediates, resulting in irreversible destruction.[45,56] However, it is important to note that no direct evidence of peroxide intermediates has been demonstrated. As discussed earlier, the mechanism of water oxidation may depend on the formation of hydroxyl radical in the water oxidation reaction pathway. The low overpotential for valence band holes when oxidizing water to hydroxyl radical may result in reaction kinetics that dominate the rate limiting step. A build up of surface holes would then occur, increasing the rate of deleterious side reactions. The influence of electrochromism on the stability and rate of WO_3 photoelectrochemical reactions has not been explored previously in the literature, despite strong indications of a relationship given by the extensive photoelectron spectroscopy performed in the literature. If tungsten bronze species, which are electrochemically active, do behave as donors, then a build up of surface holes could oxidize them and hinder the rate of reaction at the WO_3 electrode.

1.5. Scope of This Thesis

In this work, the effect of the electrolyte on the stability of *n*-type WO_3 material and also the reaction selectivity for the OER and chloride oxidation are described.

In Chapter 2, the photocurrent decay seen during the OER on WO_3 materials is investigated. The electrochromic properties of WO_3 are demonstrated to affect photoelectrochemical metrics such as photosaturated current density and the potential of photocurrent onset. Tungsten bronzes (MWO_3, M = Group I cation) can be formed in the host WO_3 electrochemically and an increase in the donor density occurs due to the reduction of W^{+6} to W^{+5}. During solar fuel operation, the oxidation of tungsten bronze impurities occurs in a side reaction and a loss of donor density occurs resulting in the decay of photocurrent. However, the formation of tungsten bronze (HWO_3) is photo-driven and the donor density is replenished, restoring the photocurrent.

The work in this chapter serves as a starting point to highlight the interplay between between both the composition and electronic structure of WO_3 and the substrate to be

oxidized in solution. We continue this line of investigation in Chapter 3, where chloride oxidation is used to demonstrate that WO_3 stability is tied to the kinetics of the photoreactions occurring at the surface of the material. The rate of chloride oxidation is much faster than the rate of water oxidation, allowing for rapid consumption of photogenerated holes. By preventing a build-up of photogenerated through electron injection via chloride oxidation, the oxidation of tungsten bronze donor species is prevented.

Having shown that chloride oxidation occurs much more readily water oxidation on WO_3 surface, the reactivity of the hypochlorous acid product is investigated in Chapter 4. Ethanol and 2-propanol are used as oxidation substrates and we observe the selective formation of acetaldehyde and acetone, respectively.

References

[1] Feulner, G. Formation of Most of our Coal Brought Earth Close to Global Glaciation. *Proc. Natl. Acad. Sci. U.S.A.* **2017**, *114*, 11333–11337.

[2] Schramski, J. R.; Gattie, D. K.; Brown, J. H. Human Domination of the Bioshpere, Rapid Discharge of the Earth-Space Battery Foretells the Future of Humankind. *Proc. Natl. Acad. Sci. U.S.A.* **2015**, *112*, 9511–9517.

[3] Hall, C.; Klitgaard, K. *Energy and the Wealth of Nations: Understanding the Biophysical Economy*; Springer-Verlag: New York, 2012; pp 1–407.

[4] BP (2019) Statistical Review of World Energy. `https://www.bp.com/en/global/corporate/energy-economics/statistical-review-of-world-energy.html`, Accessed: 2020-08-18.

[5] Cook, T. R.; Dogutan, D. K.; Reece, S. Y.; Surendranath, Y.; Teets, T. S.; Nocera, D. G. Solar Energy Supply and Storage for the Legacy and Nonlegacy Worlds. *Chem. Rev.* **2010**, *110*, 6474–6502.

[6] Abbott, D. Is Nuclear Power Globally Scalable? *Proc. IEEE* **2011**, *99*, 1611–1617.

[7] Jacobson, M. Z. Review of Solutions to Global Warming, Air Pollution, and Energy Security. *Energy Environ. Sci.* **2009**, *2*, 148–173.

[8] Murty, K. L.; Charit, I. Structural Materials for Gen-IV Nuclear Reactors: Challenges and Opportunities. *J. Nuclear Mater.* **2008**, *383*, 189–195.

[9] Ramana, M. V. Nuclear Power: Economic, Safety, Health, and Environmental Issues of Near-Term Technologies. *Annu. Rev. Environ. Resources* **2009**, *34*, 127–152.

[10] McCombie, C.; Jefferson, M. Renewable and Nuclear Electricity: Comparison of Environmental Impacts. *Energy Policy* **2016**, *96*, 758–769.

[11] Weart, S. W. *Nuclear Fear: A History of Images*; Harvard University Press: Cambridge, Massachusetts, USA, 1988.

[12] World Energy Assessment Report: Energy and the Challenge of Sustainability. United Nations Development Program, 2003.

[13] Thomas, J. M.; Zamaraev, K. I. *Perspectives in Catalysis*; Blackwell Sci. Publ.: Oxford, 1992.

[14] Rideal, E. K.; Taylor, H. S. *Catalysis in Theory and Practice*; Macmillan: London, 1919.

[15] Brundtland, C. G. *The World Commission on Environmental Development*; Oxford University Press: Oxford, 1987.

[16] Bard, A. J.; Fox, M. A. Artificial Photosynthesis: Solar Splitting of Water to Hydrogen and Oxygen. *Acc. Chem. Res.* **1995**, *28*, 141–145.

[17] Lhermitte, C. R.; Sivula, K. Alternative Oxidation Reactions for Solar-Driven Fuel Production. *ACS Catal.* **2019**, *9*, 2007–2017.

[18] Brédas, J. L.; Calbert, J. P.; da Silva, F.; Cornil, J. Organic Semiconductors: Theoretical Characterization of the Basic Parameters Governing Charge Transport. *Proc. Natl. Acad. Sci. U.S.A.* **2002**, *99*, 5804–5809.

[19] Sivula, K.; van de Krol, R. Semiconducting Materials for Photoelectrochemical Energy Conversion. *Nat. Rev. Mater.* **2016**,

[20] Hoffmann, R. *Solids and Surfaces : a Chemist's View of Extended Bonding*; VCH Publishers: New York, NY, 1988.

[21] Rajeshwar, K. *Encyclopedia of Electrochemistry*; American Cancer Society, 2007; Chapter 1, pp 1–52.

[22] Walter, M. G.; Warren, E. L.; McKone, J. R.; Boettcher, S. W.; Mi, Q.; Santori, E. A.; Lewis, N. S. Solar Water Splitting Cells. *Chem. Rev.* **2010**, *110*, 6446–6473.

[23] Butler, M. A.; Nasby, R. D.; Quinn, R. K. Tungsten Trioxide as an Electrode for Photoelectrolysis of Water. *Solid State Commun.* **1976**, *19*, 1011–1014.

[24] Fujishima, A.; Honda, K. Electrochemical Photolysis of Water at a Semiconductor Electrode. *Nature* **1972**, *238*, 37–38.

[25] Mavroides, J. G.; Kafalas, J. A.; Kolesar, D. F. Photoelectrolysis of Water in Cells with $SrTiO_3$ Anodes. *Appl. Phys. Lett.* **1976**, *28*, 241–243.

[26] Nasby, R. D.; Quinn, R. K. Photoassisted Electrolysis of Water using a $BaTiO_3$ Electrode. *Mater. Res. Bull.* **1976**, *11*, 985–992.

[27] Möllers, F.; Memming, R. Electrochemical Studies of Semiconducting SnO_2-Electrodes. *Ber. Bunsenges Phys. Chem.* **1972**, *76*, 469–475.

[28] Ping, Y.; Galli, G. Optimizing the Band Edges of Tungsten Trioxide for Water Oxidation: A First-Principles Study. *J. Phys. Chem. C* **2014**, *118*, 6019–6028.

[29] Martins, A. S.; Cardeiro-Junior, P. J. M.; Bessegato, G. G.; Carneiro, J. F.; Zanoni, M. V. B.; Lanza, M. R. V. Electrodeposition of WO_3 on Ti Substrate and the Influence of Interfacial Oxide Layer Generated in situ: A Photolectrocatalytic Degradation of Propyl Paraben. *Appl. Surf. Sci.* **2019**, *464*, 664–672.

[30] Pan, D.; Xiao, S.; Chen, X.; Li, R.; Cao, Y.; Zhang, D.; Pu, S.; Li, Z.; Li, G.; Li, H. Efficient Photocatalytic Fuel Cell via Simultaneous Visible-Photoelectrocatalytic Degradation and Electricity Generation on Porous Coral-like WO_3/W Photoelectrode. *Environ. Sci. Technol.* **2019**, *53*, 3697–3706.

[31] Peleyeju, M. G.; Arotiba, O. A. Recent Trend in Visible-Light Photoelectrocatalytic Systems for Degradation of Organic Contaminants in Water/Wastewater. **2018**, *4*, 1389–1411.

[32] Guaraldo, T. T.; Gonçales, V. R.; Silva, B. F.; de Torresi, S. I. C.; Zanoni, M. V. B. Hydrogen Production and Simulatneous Photoelectrocatalytic Pollutant Oxidation Using TiO_2/WO_3 Nanostructured Photoanode Under Visible Light Irradiation. *J. Electroanal. Chem.* **2016**, *765*.

[33] Tomita, O.; Ohtani, B.; Abe, R. Highly Selective Phenol Production from Benzene on a Platinum-Loaded Tungsten Oxide Photocatalyst with Water and Molecular Oxygen: Selective Oxidation of Water by Holes for Generating Hydroxyl Radical as the Predominant Source of the Hydroxyl Group. *Catal. Sci. Technol.* **2014**, *4*, 3850–3860.

[34] Proctor, A. D.; Bartlett, B. M. Hydroxyl Radical Suppression During Photoelectrocatalytic Water Oxidation on WO_3|FeOOH. *J. Phys. Chem. C* **2020**, *124*, 17957–17963.

[35] Wardman, P. Reduction Potentials of One-Electron Couples Involving Free Radicals in Aqueous Solution. *J. Phys. Chem. Ref. Data* **1989**, *18*, 17957–197963.

[36] Butler, M. A. Photoelectrolysis and Physical Properties of the Semiconducting Electrode WO_2. *J. Appl. Phys.* **1977**, *48*, 1914–1920.

[37] Huda, M. N.; Yan, Y.; Moon, C.-Y.; Wei, S.-H.; Al-Jassim, M. M. Density-Functional Theory Study of the Effects of Atomic Impurity onthe Band Edges of Monoclinic WO_3. *Phys. Rev. B* **2008**, *77*, 195102.

[38] Paluselli, D.; Marsen, B.; Miller, E. L.; Rocheleau, R. E. Nitrogen Doping of Reactively Sputtered Tungsten Oxide Filmes. *Electrochem. Solid-State. Lett.* **2005**, *8*, G301–G303.

[39] Tang, J.; Ye, J. Correlation of Crystal Structures and Electronic Structures and Photocatalytic Properties of the W-Containing Oxides. *J. Mater. Chem.* **2005**, *15*, 4246–4251.

[40] Maruthamuthu, P.; Ashokkumar, M.; Gurunathan, K.; Subramanian, E.; Sastri, M. Hydrogen Evolution from Water with Visible Radiation in Presence of Cu(II)/WO_3 and Electron Relay. *Int. J. Hydrogen Energy* **1989**, *14*, 525–528.

[41] Wang, F.; Di Valentin, C.; Pacchioni, G. Doping of WO_3 for Photocatalytic Water Splitting: Hints from Density Functional Theory. *J. Phys. Chem. C* **2012**, *14*, 8901–8909.

[42] Wang, F.; Di Valentin, C.; Pacchioni, G. Semiconductor-to-Metal Transition in WO_{3-x}: Nature of the Oxygen Vacancy. *Phys. Rev. B* **2011**, *84*, 073103.

[43] Juodkazytė, J.; Petrulevičienė, M.; Parvin, M.; Šebeka, B.; Savickaja, I.; Pakštas, V.; Naujokaitis, A.; Virkutis, J.; Gegeckas, A. Activity of Sol-Gel Derived Nanocrystalline WO_3 Films in Photoelectrochemical Generation of Reactive Chlorine Species. *J. Electroanal. Chem.* **2020**, *871*, 114277.

[44] Jadwiszczak, M.; Jakubow-Piotrowska, K.; Kedzierzawski, P.; Bienkowski, K.; Augustynski, J. Highly Efficient Sunlight-Driven Seawater Splitting in a Photoelectrochemical Cell with Chlorine Evolved at Nanostructured WO_3 Photoanode and Hydrogen Stored as Hydride within Metallic Cathode. *Adv. Energy Mater.* **2019**, *10*, 1903213.

[45] Hill, J. C.; Choi, K.-S. Effect of Electrolytes on the Selectivity and Stability of n-type WO_3 Photoelectrodes for Use in Solar Water Oxidation. *J. Phys. Chem. C* **2012**, *116*, 7612–7620.

[46] Wertheim, G. K.; Campagna, M.; Chazalviel, J.-N.; Buchanan, D. N. E.; Shanks, H. R. Electronic Structure of Tetragonal Tungsten Bronzes and Electrochromic Oxides. *Appl. Phys.* **1977**, *13*, 225–230.

[47] Bullett, D. W. Bulk and Surface Electron States in WO_3 and Tungsten Bronzes. *J. Phys. C: Solid State Phys.* **1983**, *16*, 2197–2207.

[48] Bringans, R.; Höchst, H.; Shanks, H. R. Defect States in WO_3 Studied with Photoelectron Spectroscopy. *Phys. Rev. B* **1981**, *24*, 3481.

[49] Höchst, H.; Bringans, R.; Shanks, H. Electronic Structure of Na_xWO_3: A Photoemission Study Covering the Entire Concentration Range. *Phys. Rev. B* **1982**, *26*, 1702.

[50] Höchst, H.; Bringans, R.; Shanks, H.; Steiner, P. Failure of the Rigid Band Model in Na_xWO_3: an XPS Study. *Solid State Commun.* **1981**, *37*, 41–44.

[51] Webman, I.; Jortner, J.; Cohen, M. H. Electronic transport in alkali-tungsten bronzes. *Phys. Rev. B* **1976**, *13*, 713–724.

[52] Kamitakahara, W. A.; Harmon, B. N.; Taylor, J. G.; Kopp, L.; Shanks, H. R.; Rath, J. Concentration-Dependent Kohn Effect in Cubic Tungsten Bronzes. *Phys. Rev. Lett.* **1976**, *36*, 1393–1396.

[53] Mott, N. F. The degenerate electron gas in tungsten bronzes and in highly doped silicon. *Phil. Mag.* **1977**, *35*, 111–128.

[54] Weinberger, B. R. Nuclear-magnetic-resonance study of the cubic alkali tungsten bronzes. *Phys. Rev. B* **1978**, *17*, 566–574.

[55] Solarska, R.; Jurczakowski, R.; Augustynski, J. A highly stable, efficient visible-light driven water photoelectrolysis system using a nanocrystalline WO_3 photoanode and a methane sulfonic acid electrolyte. *Nanoscale* **2012**, *4*, 1553–1556.

[56] Seabold, J. A.; Choi, K.-S. Effect of a Cobalt-Based Oxygen Evolution Catalyst on the Stability and the Selectivity of Photo-Oxidation Reactions of a WO_3 Photoanode. *Chem. Mater.* **2011**, *23*, 1105–1112.

Chapter 2.

Kinetics and Faradaic Efficiency of Oxygen Evolution on Reduced H_xWO_3

Portions of this chapter have been published:
Breuhaus-Alvarez, A. G.; DiMeglio, J. L.; Cooper, J. J.; Lhermitte C. R.; Bartlett, B. M. *J. Phys. Chem. C* **2019**, *123*, 1142-1150.

2.1. Introduction

Materials for water oxidation are restricted to those that show appreciable photon absorptivity of the solar spectrum, proper band positioning for driving water oxidation, and high stability in the strongly oxidizing conditions required oxygen evolution. The 2.5 - 2.8 eV bandgap of tungsten oxide allows absorption of the UV/blue region of the solar spectrum and a valence band edge of approximately 3 V vs RHE is positive enough to oxidize water.[1–9] However, continuous decay in the photocurrent density is observed under potentiostatic conditions in all pH ranges even though WO_3 is acid-stable at pH < 5.[2] Soluble peroxytungstate intermediates are proposed as the primary mechanism for activity loss in acidic conditions, which WO_3 is normally stable in.[2,10] Alternatively, the formation of a blocking layer formed by accumulating peroxide species on the surface of WO_3 has also been proposed.[11,12] In addition, the Faradaic efficiency for the Oxygen Evolution Reaction (OER) is low, and is generally attributed to kinetically facile electrolyte anion oxidation.[13] The four-electron oxidation of water requires forming two O–O bonds (σ and π), which hinders the reaction. These problems reduce the adoption of WO_3 in water splitting applications unless they can be remediated.

Another property of WO_3 that has relevance to our findings is electrochromism, often exploited in smart windows and displays. Formal reduction of W^{6+} to W^{5+} under an

applied bias is accompanied by intercalation of H^+ or the group I metals cations Li^+, Na^+, or K^+ to maintain electroneutrality. This reversible reaction, described in Equation 2.1, gives rise to a color change from translucent yellow to a deep blue in the forward direction:

$$WO_3(s) + xM^+(aq) + xe^- \longleftrightarrow M_xWO_3(s) \tag{2.1}$$

where M is the intercalated cation or a proton. The color change is observed as the growth of a near-IR band and the density of states near the Fermi level increases as the tungsten t_{2g} band is filled.[14,15] This reaction can also be induced in photochromic process in solution, governed by Equations 2.2–2.5.[16–20]

$$WO_3(s) + h\nu \longrightarrow {WO_3}^*(s) + e^-_{CB} + h^+_{VB} \tag{2.2}$$

$$h^+_{VB} + \frac{1}{2}H_2O(l) \longrightarrow H^+(aq) + \frac{1}{4}O_2(g) \tag{2.3}$$

$$WO_3(s) + e^-_{CB} + H^+(aq) \longrightarrow HWO_3(s) \tag{2.4}$$

$$WO_3(s) + h\nu + \frac{1}{2}H_2O(l) \longrightarrow HWO_3(s) + \frac{1}{4}O_2(g) \tag{2.5}$$

Equations 2.2 and 2.3 represent light-induced water oxidation by a photogenerated hole, Equation 2.4 represents tungsten reduction by the conduction band electron and proton injection, and Equation 2.5 is the overall chemical reaction. Because the photoactivity of a semiconductor is closely tied to its electronic structure, this reductive proton intercalation reaction affects the activity for OER on WO_3.

In this manuscript, WO_3 photocatalysts were deposited on fluorine-doped tin oxide (FTO) conducting glass substrate by spin coating an ammonium metatungstate (AMT) sol. We report the reversibility of photocurrent decay observed during WO_3 photoelectrochemical (PEC) OER at pH 1. Our main findings are that photocurrent decay is observed during potentiostatic conditions with concomitant loss of O2 production. Irradiation at open circuit for several hours induces a photocurrent recovery, and, continuous headspace sampling by gas chromatography (GC) shows that the OER activity

also recovers.

2.2. Experimental

2.2.1. Chemicals

Sulfuric acid (95.0 – 98.0 w/w%) and anhydrous ethanol purchased from Fisher Scientific. Ammonium metatungstate $(NH_4)_6H_2W_{12}O_{40} \cdot xH_2O$, poly(ethylene glycol) M_w = 300 Da, PEG-300), 1000 ppm ICP standards for tungsten and bismuth, hydrogen peroxide (30% w/w), potassium chloride, and sodium hydroxide were purchased from Sigma Aldrich. Thermogravimetric analysis was performed on the received AMT and x was determined to be 3.1 (Figure A.1). In all experiments, water was filtered by a Millipore filtration system (18.2 $M\Omega \cdot cm^{-1}$). FTO (Pilkington Glass TEC-15) substrate was cut into 3×1 cm^{-1} strips. FTO substrate was first coarsely cleaned by scrubbing with an acetone wetted Kimwipe™. This cleaning procedure was followed by sonicating in a series of reagents: acetone, Sparkleen™ detergent, water, and acetone again for 10 minutes each, with each solvent wash followed by drying under a flowing N_2 stream. Ag/AgCl reference electrodes were purchased from CH Instruments and filled with saturated KCl aqueous solution. 99.95% pure Pt wire was purchased from Sure Pure Chemetals.

2.2.2. Synthesis of WO_3 Electrodes.

WO_3 electrodes were synthesized by spin coating an AMT sol. The precursor was prepared by adding 2.51 g (833 μg) AMT to a 100 mL round boton and then adding 10 mL of water to dissolve completely with vigorous stirring. Spearately, 6.6 g (22 mmol) of PEG-300 were dissolved in 10 mL of ethanol in a scintillation vial. The ethanol solution was slowly poured into the aqueous solution while stirring vigorously over the course of approximately 90 seconds, resulting in a faint, off-white sol precursor, which was 0.5 M in tungsten. Electrodes for PEC measurements were prepared by dropping 200 μL of precursor sol onto clean, 2.54 cm squares (6.45 cm^2) of FTO and then spun at 2500 rpm for 30 seconds using Laurell spin coater. X-ray photoelectron spectroscopy (XPS) and electrochemical impedance spectroscopy (EIS) experiments were performed on 1

cm^2 samples on WO_3 which were prepared by dropping and spinning 30 μL of precursor onto 1 cm $\times$ 1 cm area masked off on a 1 cm $\times$ 3 cm strip of clean FTO. The precursor was constantly and vigorously stirred then sealed tightly when not in use. The precursor was stored for no more than three days under ambient conditions. Following spin coat deposition, the electrodes were transferred to a muffle furnace preheated to 500 °C for thirty minutes. This deposition and annealing cycle was repeated ten times total to achieve films approximately 2 μm in thickness.

2.2.3. Materials Characterization.

X-ray diffraction (XRD) was recorded with a Panalytical Empyrean diffractometer at a power of 1.8 kW (45 kV, 40 mA) using Cu Kα (λ = 1.5418 Å) in $\theta - \theta$. XPS was collected using a Kratos Axis Ultra X-ray photoelectron spectrometer. The X-rays used were monochromatic Al K Kα X-rays (1486.7 eV) and measurements performed at an analysis chamber pressure of $\approx 1 \cdot 10^{-9}$ Torr. An electron flood gun was used to compensate for charging during data collection. Casa XPS software was used with a Shirley-type baseline to calculate the peak areas; binding energies were determined by setting adventitious carbon signal to 248.8 eV. UV-Vis-NIR spectra were recorded using a Cary 5000 spectrophotometer (Agilent) in reflectance mode with an external diffuse reflectance accessory. Samples prepared by thoroughly grinding 10 mg of WO_3 powder with 90 mg of barium sulfate with a mortar and pestle. Reflectance data was mathematically transformed using Kubelka–Munk function.

$$F(R)_{Kubelka-Munk} = \frac{(1-R)^2}{2R} \tag{2.6}$$

2.2.4. Photoelectrochemistry.

Three-electrode PEC experiments were performed using CH Instruments Series 760 E electrochemical workstation and a Newport-Oriel 150 W Xe arc lamp. The light source was affixed with an AM1.5G simulating solar filter (Newport) and adjusted to the appropriate irradiance using a thermopile detector (Newport 818P-015-19) and an optical power meter (Newport 1918-R). The 1 cm $\times$ 3 cm WO_3 electrodes used in XPS anal-

ysis were illuminated from the backside through a quartz window in a glass cell also containing the saturated Ag/AgCl reference electrode and Pt wire counter electrode. All other PEC experiments were performed in a custom-designed compression cell A.2. When measuring the OER rate, the counter electrode was separated from the reference and working electrode by a Nafion™ membrane (Fuel Cell Earth, NRE-212), and the working electrode compartment is sealed tightly. For experiments that do not require measuring the OER rate, the membrane was removed, and the cell was not tightly sealed against ambient atmosphere. Drift in the Ag/AgCl reference electrode was monitored by periodically measuring its potential against a fresh, unused Ag/AgCl electrode kept only in saturated KCl electrolyte. The electrolyte used in this work was prepared by adding H_2SO_4 to Millipore water until the pH reached 1.

2.2.5. Electrochemical Impedance Spectroscopy.

EIS measurements were performed on a Metrohm Autolab electrochemical station. Due to the surface intercalation chemistry at the WO_3 surface, Mott-Schottky (MS) analysis becomes more complex than modeling the system with a single RC Randles circuit in series with the solution resistance. For ideal semiconducting materials, the linear region of C_{sc}^{-2} vs E can be given by relating the space charge layer capacitance (C_{sc}^{-2}) with the applied potential (E) according to Equation 2.7.

$$\frac{1}{C_{sc}^{-2}} = \frac{2}{e\epsilon_0 N_D \epsilon_r}\left(E - E_{fb} - \frac{k_B T}{e}\right) \tag{2.7}$$

where e is the charge on on an electron ($1.602 \cdot 10^{19}$ C), ϵ_0 is the permittivity in vacuum ($8.85 \cdot 10^{-14}$ F cm^{-1}), N_D is the donor density in cm^{-3}, E_{fb} is the flat-band potential in V, k_B is the Boltzmann constant ($1.381 \cdot 10^{-23}$ J K^{-1}), T is temeprature (298 K), and ϵ_r is the relative permittivity of WO_3 (40).[21,22] However, impedance analysis reveals a frequency dependence in the slope on the frequency of the C_{sc}^{-2} vs E curves, which is proposed to arise from microroughness and inhomogeneity in the donor species.[23–26] A more accurate model for metal oxide semiconductors exhibiting non-ideal impedance responses can be given by replacing the capacitor in the Randles circuit with a constant

phase element (CPE). Then, the impedance of the CPE is given by Equation 2.8.[27]

$$\mathrm{Z_{CPE}} = \frac{1}{Y_0(j\omega)^{\alpha}} \tag{2.8}$$

Using ZView, a fit was performed on the impedance spectrum collected at each potential to obtain Y_0 and α as well as the solution (R_s) and polarization (R_p) resistances. Using the values determined from fitting, the effective capacitance for each potential was calculated using the expression determined by Brug *et al.* shown in Equation 2.9.[28]

$$C = {Y_0}^{\frac{1}{\alpha}} \left({R_s}^{-1} + {R_p}^{-1} \right)^{\frac{\alpha-1}{\alpha}} \tag{2.9}$$

The capacitance values from Equation 2.9 calculated at each potential were used to determine the donor density and flat-band potential in Equation 2.7. For these experiments, a 2.41 cm^2 electrode was used. When performing MS analysis, the solution used was a 0.5 M Na_2SO_4 solution set to pH 1 with H_2SO_4 in order to maintain high solution conductivity during impedance analysis.

2.2.6. Oxygen-Evolution Measurements.

Oxygen detection experiments were performed in a custom-designed two-compartment cell machined from poly(vinyl chloride) (PVC) Type 1 (McMaster-Carr, 8745K63) (A.2). This material has the advantage of high stability in harsh chemical environments. The design of this cell was inspired by a design used by the Jaramillo group.[29] A compression seal was maintained using Viton fluoroelastomer o-rings (McMaster-Carr, 1284N11). A Nafion™ membrane (Fuel Cell Earth, NRE-212) was used to separate the two compartments. The window of the working compartment was composed of the WO_3 electrode compression sealed against the cell and was back illuminated with 200 mW $\cdot$ cm^{-2} simulated sunlight. Flowing N_2 was passed at a constant rate of 2.000 mL $\cdot$ min^{-1} ensured by a mass flow controller (Omega, FMA-LP2614A) into the working compartment electrolyte, and the headspace was connected to a Thermo Fisher Trace 1310 gas chromatograph equipped with a 6 molecular sieve 13x packed column (SRI, 8600-PK3B). Helium carrier gas used at a flow rate of 30 mL $\cdot$ min^{-1} and oven temperature was kept constant at 40 °C. The flowing product stream was sampled by GC every 2.5 minutes.

The validity of this method was tested by performing water oxidation with nickel foil in 1 M NaOH (A.3).

2.2.7. Dissolved Tungsten Detection.

The extent of film dissolution was determined by comparing the quantity of tungsten in the electrolyte solution after photoelectrolysis against the total amount of tungsten contained in the film used to perform the experiment. The extent of chemical decomposition was also measured by soaking a WO_3 electrode in pH 1 sulfate electrolyte in the dark with no applied bias for the same time period as the performed electrolysis. The same control experiment was repeated, but under film illumination. Analysis was performed by inductively coupled plasma mass spectrometery (ICP-MS) using a PerkinElmer Nexion 2000. An internal standard of bismuth (20 ppb) was used. The electrolyte solution was serially diluted to bring the analyte signal into the range of the detector. WO_3 films were digested in a 5 mL solution composed of 2 mL of H_2O_2 (30 %) and 3 mL of 1 M NaOH by sonication for 1 hour at 65 °C. A series of tungsten standards were prepared by serial dilution of 1000 ppm W reference solution (Sigma-Aldrich).

2.3. Results and Discussion

WO_3 films were prepared by repeated spin coating of an AMT sol followed by annealing according to the balanced Equation:

$$(NH_4)_6H_2W_{12}O_{40} \cdot xH_2O\,(aq) + \frac{15}{2}\,O_2(g) \longrightarrow 12\,WO_3(s) + 6\,NO\,(g) + (13 + x)H_2O\,(g) \tag{2.10}$$

The optimal thickness was determined by comparing the photocurrent densities and onset potentials measured by linear sweep voltammetry (LSV) of films composed of different number of depositions under 1-sun illumination. 10 deposition cycles gave rise to the largest slope in the *j*-*E* curve with a photocurrent density that saturates at 0.8 $mA \cdot cm^{-2}$ at pH 1 (A.4). Top-down and cross-sectional SEM images of these films show that the resulting 2 μm films are flat and evenly cover the FTO substrate (A.5). The films obtained are monoclinic WO_3 by XRD (A.6).

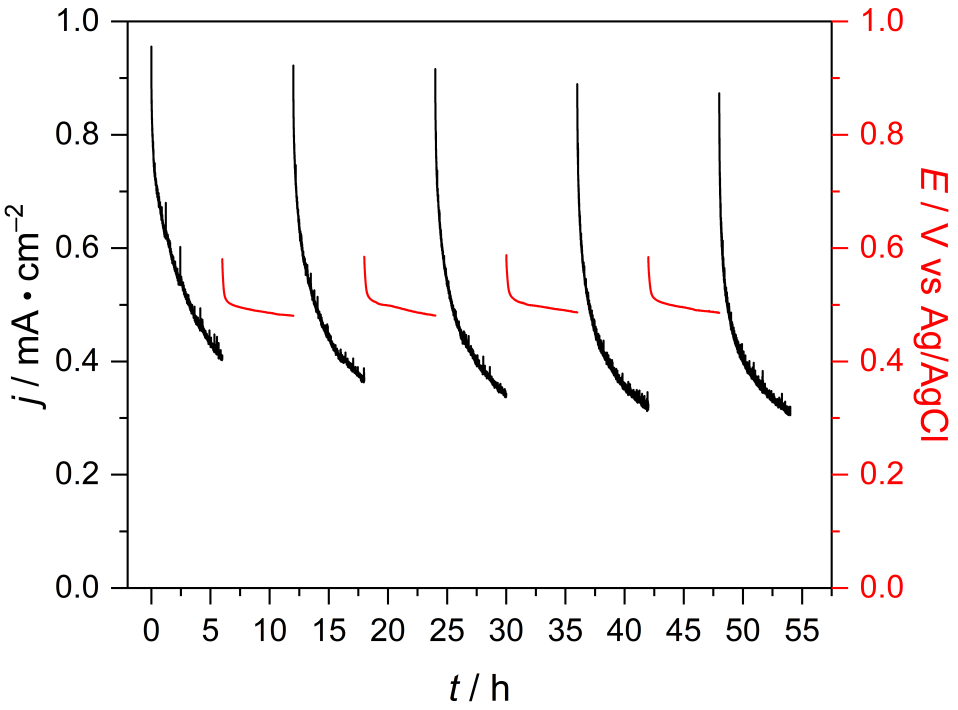

Figure 2.1: Consecutive cycles of WO_3 poised at 0.98 V vs Ag/AgCl (black) followed by open circuit potential measurement (red) under 2-sun illumination.

The photoelectrochemical characteristics of these films were determined in an aqueous sulfuric acid solution set to pH 1. First, controlled potential coulometry (CPC) at 0.98 V vs Ag/AgCl (1.2 V vs RHE) was recorded for 6 h under 200 mW $\cdot$ cm^{-2} simulated solar (2-sun) illumination. The first black trace of Figure 2.1 shows that the current density continually drops from 0.9 to 0.4 mA $\cdot$ cm^{-2} over the 6 h experiment. Then, the potential pulse is stopped and the open circuit potential (OCP) is recorded *while still under 2-sun illumination* for 6 more hours (Figure 2.1, red trace). It must be noted that there is a delay between the end of the CPC experiment and the beginning of the subsequent OCP experiment due to the potentiostat control software saving the data from the previous experiment and initial-izing the program for the subsequent experiment. It is during this short time window that the OCP rapidly drops from the 0.98 V vs Ag/AgCl the electrode had been poised at to around 0.6 V vs Ag/AgCl. In the recorded data, the OCP drops first sharply then smoothly by $\approx$ 100 mV (from 0.6 to 0.5 V vs Ag/AgCl). These CPC and OCP measurements are repeated several times

to reveal reversibility of photocurrent decay. Replicates of this experiment on different films are shown in the supporting information (Figure A.7).

The loss and recovery of the photocurrent density suggests the consumption and regeneration of a finite species within the WO_3 electrode rather than dissolution, which would be irreversible as products diffuse away from the electrode. The continuous shift in OCP over 6 h suggests that the WO_3 electrode is changing in a reversible manner by way of a photodriven process. We note that the peak current recorded at the beginning of each CPC measurement in Figure 2.1 decreases steadily with each cycle. This result could indicate some loss of photoactive material, perhaps by peroxytungstate intermediates as previously suggested in literature. ICP-MS analysis of the electrolyte carried out after 24 h of CPC at 0.98 V vs Ag/AgCl under 1-sun AM 1.5G illumination shows that 2.3% of WO_3 dissolves during the course of the electrolysis. As a control experiment, the extent of WO_3 dissolution in pH 1 sulfuric acid electrolyte for 24 h in the dark with no applied bias is 0.13%. For a WO_3 film under 1-sun illumination at no applied bias, 0.87% dissolves after 24 hours. Regardless, the amount of WO_3 lost during a given 6 h segment at 0.98 V vs Ag/AgCl in Figure 2.1 is then small, and the decrease in peak current with cycle number must arise from a non-destructive mechanism. We propose that under illumination at open circuit, the photochromic process described in Equations 2.2 - 2.5 occurs, causing a change in composition. The shift in OCP results from the increased concentration of reduced tungsten. To understand better the effect of illumination on the current recovery, we carried out a second CPC/OCP experiment with data shown in Figure 2.2. In this experiment, the electrode was poised at 0.98 V vs Ag/AgCl for 3.5 hours (black trace) followed by a 3.5-hour period at open circuit (red trace). The CPC/OCP cycle was repeated two more times and then the experiment ended with a CPC measurement. For the first two OCP measurements (Figure 2.2, gray region), the WO_3 electrode rested in the dark. During this period in the dark, the open circuit potential remained near the 0.98 V vs Ag/AgCl it had been poised at during the CPC measurement. The slight downward shift in open circuit potential is likely driven by diffusional equilibration of the ions within the permeable material.

During electrolysis at positive applied bias, cations are expelled and anions drawn into the electrical double layer. A shift in open circuit potential would come about from

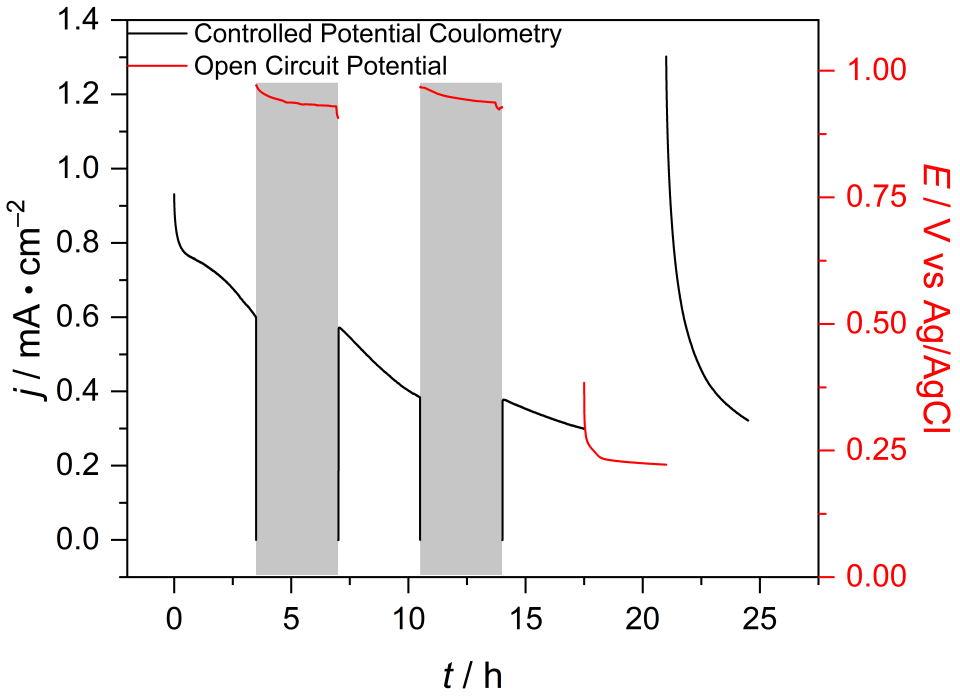

Figure 2.2: CPC of a WO_3 electrode poised (black trace) at 0.98 V vs Ag/AgCl in pH 1 sulfuric acid solution with the resulting current measured in 3.5-hour intervals. Between CPC sections, the electrode sat at open circuit, and the OCP (red trace) was measured for 3.5 hours. Regions shaded in gray are in the dark. For all other times, the film was illuminated with 2-sun light.

reprotonation of the WO_3 surface, which has a point of zero charge at approximately pH 2.5, and this likely accounts for the slight drop in OCP seen over the 3.5-hour period in the dark.[30,31] In the dark, there is no shift in the OCP and no recovery in photocurrent; photocurrent recovery is only observed under illumination conditions. Figure 2.3 shows the effects of light irradiance (E_e) and pH on the change in photocurrent density. These measurements were carried out by by recording an initial LSV sweep from the OCP to 1.5 V vs Ag/AgCl. Then, the films were left to rest under illumination for 15 minutes. Finally, the LSV trace was recorded again and the difference in current density (Δj) at 1.5 V vs Ag/AgCl between the two scans is plotted. In Figure 2.3a, a WO_3 film was placed in pH 0 sulfuric acid solution. These measurements were taken on the same film, recorded from low to high irradiance. The individual LSV sweeps are presented in Figure A.8. At pH 0, the proton concentration is high, Δj increases linearly with irradiance. This result suggests that the photocurrent recovery at high

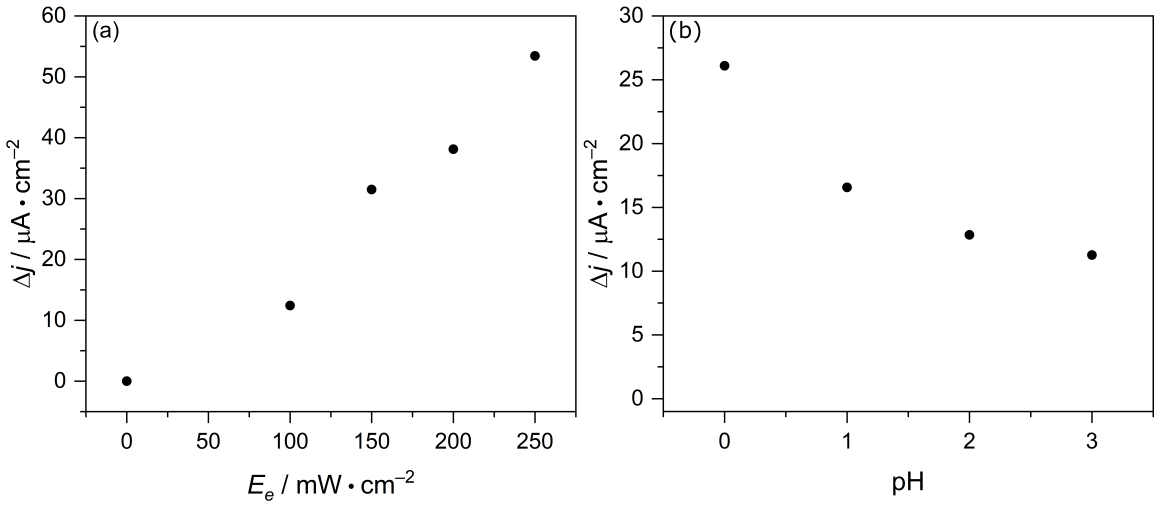

Figure 2.3: (a) Increase in photocurrent (Δj) as a function of irradiance at 1.5 V vs Ag/AgCl during LSV analysis after resting the film for 15 minutes under illumination at of OCP, pH 0. (b) Δj as a function of pH at at 1.5 V vs Ag/AgCl during LSV analysis at constant (2-sun) irradiance.

proton concentration is limited by the photon flux. In Figure 2.3b, the effect of pH was measured while maintaining a constant irradiance of 200 mW $\cdot$ cm^{-1}. As before, the initial LSV sweep was recorded, a 15-minute rest period under illumination applied, and the second LSV sweep was recorded. Measurements started with a pH 3 sulfuric acid electrolyte and were incrementally made more acidic. When changing electrolyte to the next (more acidic) solution, the cell was rinsed with approximately 400 mL of the next electrolyte solution to prevent shifts in the unbuffered electrolyte solution. Again, the individual LSV sweeps are shown in Figure A.8. As pH increases, the magnitude of photocurrent recovery decreases, suggesting that H^+ becomes limiting instead of light. These experiments highlight the light-driven nature of the photocurrent recovery as well as the dependence of the recovery on pH. In the literature, there exists some disagreement as to whether the photochromic effect in WO_3 is due to color center formation or proton intercalation,[17,19] but our results suggest that H^+ intercalation is the dominant factor, at least in aqueous acidic electrolytes.

In Figure 2.2, the continuous decay observed during the first three CPC has previously been ascribed to dissolution of the active material or formation of an inactive surface layer. However, the loss is reversible and the rapid shift in the Fermi level to

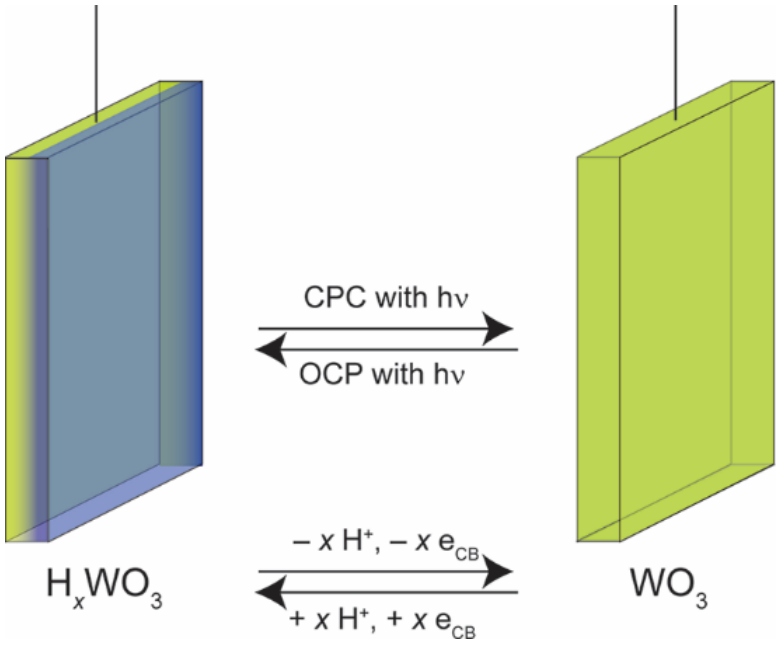

Figure 2.4: Reversible H^+ intercalation/deintercalation in WO_3.

more negative potentials during illuminated open circuit conditions indicates the donor density is increasing. Improving the photocurrent density in WO_3 by increasing the donor density has previously been shown through hydrogen treating WO_3 films.[8] They hydrogen treatment reduces W^{6+} to W^{5+} with concomitant introduction of oxygen vacancies, but the reaction requires high temperature (350 °C). In our experiments, the photocurrent decay occurs over a period of hours, indicating that the WO_3 electrode is undergoing a gradual change in composition. In electrochromic materials like WO_3, ion trapping and slow diffusion prevents the rapid deintercalation of ions from the host material and causes losses in the quan-tity of intercalated/deintercalated cations during repeated cyclic voltammograms for electrochromic applications. But, rejuvenating the electrochromism in WO_3 (reversing Equation 2.1) has been demonstrate by anodic galvanostatic or potentiostatic conditioning over a period of hours.[32–34] The conditions present during OER photocatalysis are sufficient to slowly remove trapped protons from H_xWO_3 and re-oxidize tungsten, resulting in a material with a more positive Fermi level, lower donor density, and lower photocurrent density, illustrated in Figure refscheme1. Then, Figure 2.5 shows the the galvanostatic experiment that forces deintercalation of protons in H_xWO_3 to determine the value of x in our H_xWO_3 films. 100 nA anodic

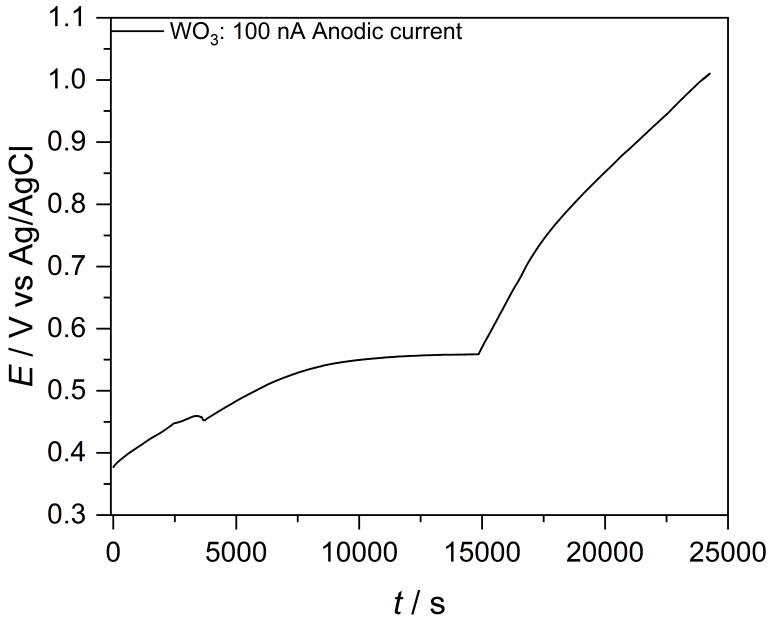

Figure 2.5: Galvanostatic conditioning experiment of WO_3 in the dark with pH 1 sulfuric acid electrolyte. The potential required to maintain 100 nA of anodic current through the 2.41 cm^2 H_xWO_3 electrode is recorded.

current was applied to a film in the dark. During galvanostatic conditioning, the potential rises slowly from 0.38 V vs Ag/AgCl until approximately 0.55 V vs Ag/AgCl as the reverse of reaction 2.1 occurs, and overall electrode composition changes gradually to WO_3. Then, at $1.5 \cdot 10^4$ seconds, an abrupt kink in the potential trace is observed, marking the end of H_xWO_3 oxidation. To calculate the percent of degree of protonation in the material by electrochemical techniques, the charge passed during the $1.5 \cdot 10^4$ seconds of H_xWO_3 oxidation in the galvanostatic experiment was converted to moles electrons removed per area ($6.4 \cdot 10^{-9}$ moles $e^- \cdot cm^{-2}$). Assuming every electron removed corresponds to a proton being deintercalated, this calculation gives the moles of H_xWO_3 per unit area. The electrode was then cut to a known area and the tungsten oxide was dissolved from the film. ICP-MS analysis was performed to determine the amount of tungsten per area ($3.5 \cdot 10^{-5}$ moles $W \cdot cm^{-2}$). Dividing the HWO_3 per area by total W per area gives x as $1.8 \cdot 10^{-4}$, or an HWO_3 content of 0.02% distributed throughout the 2 μm-thick film.

To probe the changes in donor density, we carried out Mott-Schottky analysis of EIS

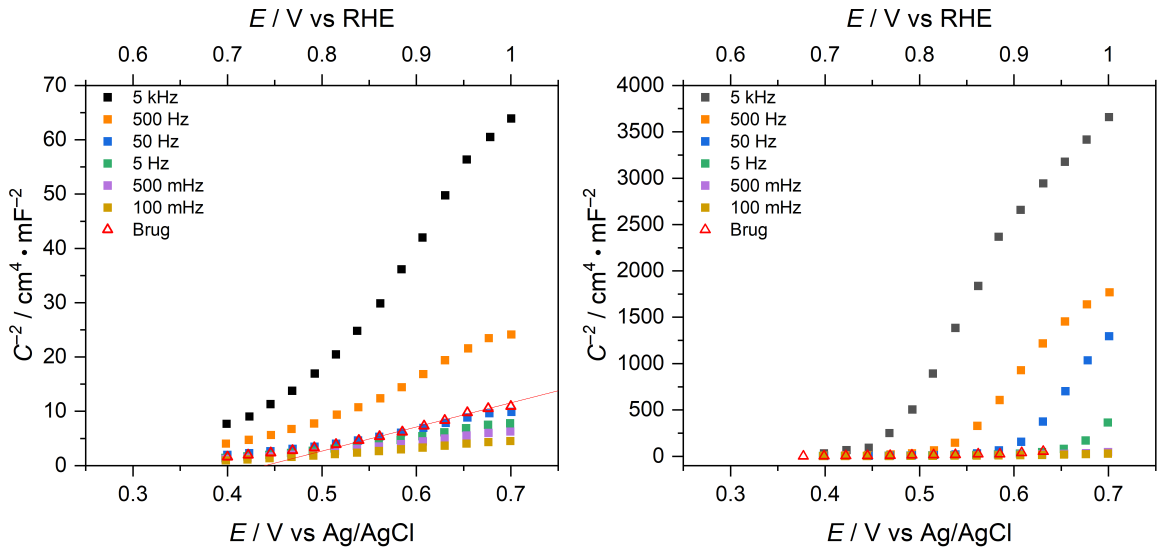

Figure 2.6: Mott-Schottky plots of EIS performed in the dark before (left) and after (right) CPC at 0.98 V vs Ag/AgCl for 24 hours, 1-sun illumination. Representative frequencies recorded at each potential are shown, and the equivalent circuit used for fitting is also illustrated.

measurements. The increase in the slope of the linear region of C^{-2} vs E following 24 h of CPC at 0.98 V vs Ag/AgCl under 100 mW $\cdot$ cm^{-2} (1-sun) illumination in Figure 2.6 shows that the donor density, N_D, decreases from an initial value of $2.8 \cdot 10^{22}$ cm^{-3} to $6.0 \cdot 10^{21}$ cm^{-3} and that the flat-band potential, E_{fb}, shifts positively from 0.36 V to 0.39 V vs Ag/AgCl (0.62 V to 0.65 V RHE). Capacitance values calculated using Equation 2.9 (hollow red triangles) are also plotted. When performing EIS, the solution used was a 0.5 M Na_2SO_4 solution. When the CPC experiment was performed, the cell was well rinsed with approximately 400 mL of pH 1 sulfuric acid before proceeding. After the CPC experiment, the electrolyte was replaced with the 0.5 M Na_2SO_4 pH 1 solution before repeating the Mott-Schottky analysis. The anodic shift in flat-band potential and the decrease in donor density indicate a more oxidized tungsten surface after the CPC experiment. XPS data (Figure A.9) fitted with a Shirley-type method show small shoulder peaks at a lower eV binding energy, corroborating the presence of W5+ at the surface. Integrating the W^{5+} peak areas yield a 2.2 mol-% content of W^{5+} in the as-prepared electrode, and it decreases to 1.4 mol-% after 24 hours of poising the same electrode at 0.98 V vs Ag/AgCl under 1-sun AM 1.5G illumination. While the 2.2% W^{5+} content measured in the as-prepared state is due to donor states from both

H_xWO_3 and oxygen vacancies, the 0.8% loss seen from electrolysis is expected to be solely from deintercatative H_xWO_3 oxidation since the oxygen activity is negligible at room temperature. The difference in measured H_xWO_3 content between the XPS and galvanostatic discharge experiment may be caused by the very low-profile depth of XPS analysis compared to galvanostatic discharge which analyzes the entire bulk film and we expect protonation to be greater at the surface.

The rapid decay of the photocurrent density during the first CPC cycle in Figure 2.1 suggests that the spin-coated films synthesized contain some intercalated protons (H_xWO_3) from the outset. Our WO_3 synthesis results from thermal decomposition of AMT. A previous report of differential thermal analysis coupled with mass spectrometry indicates that solid AMT reacts to liberate water at 116 °C and 143 °C. Then, endothermic release of N_2O occurs at 315 °C, and exothermic release of NO occurs at 441 °C.[35] No release of ammonia gas is observed between room temperature and 800 °C. During synthesis, the films are expected to contain a nitrogen : tungsten ratio of about 1 : 2 at the start of the annealing process. Our results suggest that the ammonium cation behaves as a reductant for W^{6+} to form H_xWO_3 in addition to reducing oxygen (Equation 2.10).

The effect of oxidizing H_xWO_3 while also oxidizing wa-ter is presented in the LSV traces recorded on the same electrode at different time points in Figure 2.7. The as-prepared electrode shows a saturated photocurrent density between $0.6 - 0.7$ mA $\cdot$ cm^{-2} (0.61 mA$\cdot$cm^{-2} at 1.2 V vs Ag/AgCl). After carrying out CPC under 1-sun illumination for 10 hours, the photocurrent density at 1.2 V vs Ag/AgCl drops to 0.38 mA $\cdot$ cm^{-2}. Here, it is likely limited by decreased number of charge carriers due to the oxidative deintercalation reaction. The potential at which the photocurrent density begins to saturate decreases from 1.1 V vs Ag/AgCl in the as-prepared state to 0.96 V vs Ag/AgCl after the CPC experiment, suggesting that OER operation reduces the carrier concentration. Furthermore, the photocurrent onset potential shifts from 0.50 V vs Ag/AgCl to 0.57 V vs Ag/AgCl following CPC, indicating a raised Fermi level following conversion of W^{5+} to W^{6+}. After resting at the OCP for 6 h, the photocurrent density at 1.2 V vs Ag/AgCl increases to 0.86 mA $\cdot$ cm^{-2}, which is attributed to intercalating protons to during illumination (Equation 2.5). With the recovery of W^{5+}, the photocurrent onset po-tential shifts to 0.47 V vs Ag/AgCl and photocurrent saturation potential shifts back

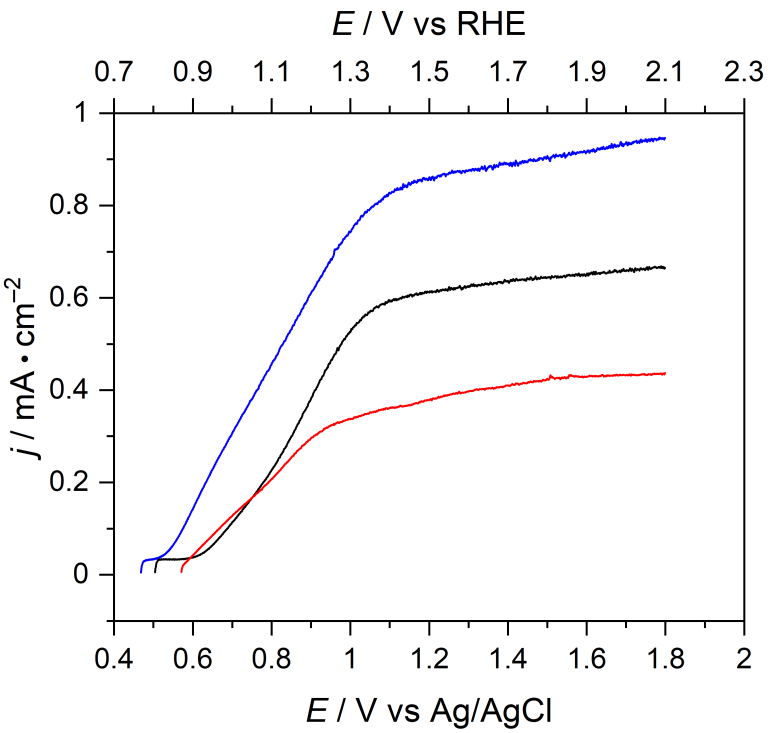

Figure 2.7: LSV traces of a WO_3 electrode in pH 1 aqueous sulfate solution and 1-sun illumination as-prepared (black), immediately following CPC at 0.98 V vs Ag/AgCl under 1-sun illumination (red), and after 6 hours of 1-sun illumination at OCP (blue).

to 1.1 V vs Ag/AgCl.

Replicates of this experiment are included as Figure A.10. In the replicates, there is slight variability in the onset potentials and photocurrent profiles as is common from film-to-film. However, the general trend of observing a decreased saturated photocurrent density and a more positive onset potential following extended CPC is observed in all cases. The onset potential shifts back to more negative values and the saturated photocurrent density also increases following 6 hours of 1-sun illumination at open circuit. The value of x in our H_xWO_3 spin coated electrodes is small, less than 1% by XPS and electrochemical methods, and yet it strongly affects the behavior of H_xWO_3 photoelectrodes in acidic aqueous media.

UV-Vis-NIR experiments with WO_3 films show absorption in NIR region, consistent with H_xWO_3 species. We acknowledge that diffuse reflectance is an imperfect analysis

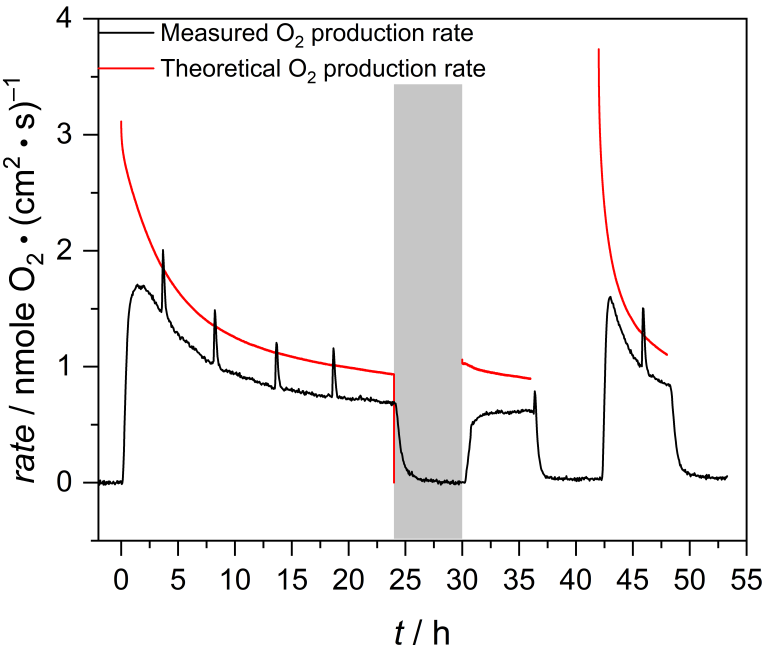

Figure 2.8: Measured OER rate (black) compared against theoretical OER rate assuming 100% Faradaic efficiency from the measured current during CPC at 0.98 V vs Ag/AgCl (red). Open circuit conditions between CPC experiments. The gray region is in the dark, while all other regions are under 2-sun illumination. Spikes in the measured rate of O_2 evolution are due to bursting gas pockets within the cell.

method for partially transmissive films and the NIR peak also contains the background absorbance from the underlying FTO substrate, but we note that diffuse reflectance measurements on WO_3 commercial powder (Figure A.11) also show an increased NIR band intensity at $\lambda > 1200$ nm (W $\rightarrow$ W MMCT) and an absorption increase for $\lambda < 420$ nm (O(2p) $\rightarrow$ W(t_{2g}) LMCT), consistent with the photochromic formation of H_xWO_3. UV-Vis results for spin coated WO_3 on FTO substrate as well as the FTO substrate itself are also shown for reference (Figure). The NIR absorption is present in our films but is convoluted by the FTO signal and the transmissive nature of the film.

We used flow-cell analysis by continuously passing the headspace to our gas chromatograph to determine the effect of H_xWO_3 formation on PEC OER .Large geometric area films of WO_3 (approximately 6.45 cm^2) were placed into the PVC oxygen-detection cell. Using ImageJ, the cell exposed window area was measured to be a 2.41 cm^2 after compressing the seals. The area exposed is fixed by the Viton fluorelastomer O-ring used

to seal the electrode to the cell. The rate of OER is determined by applying Equation 2.11 to the collected GC data:

$$rate = \frac{\text{peak area}}{m} \cdot \text{flow rate} \cdot \frac{p_0}{RT} \cdot \frac{1}{A} \tag{2.11}$$

where m is the slope of the calibration curve, the flow rate is the rate of sweeping N_2 flow, p_0 is the atmospheric pressure, R is the ideal gas constant, T is the temperature, and A is the electrode area. From Figure 2.7, the rate of OER drops from a measured peak rate of 1.7 to 0.7 nmol O_2 $cm^{-2} \cdot s^{-1}$ during 24-h illumination at 2-sun. The Faradaic efficiency for OER was calculated by integrating the area under the measured OER rate (black trace) to obtain the total num-ber of moles of O2 produced per electrode area and dividing by the area under the theoretical O_2 trace (red trace). The theoretical trace is determined by dividing the meas-ured current density by $4F$ since OER is a four-electron oxidation and F is Faraday's constant, 96,485 C mol^{-1}. Three separate CPC experiments, all poised at 0.98 V vs Ag/AgCl under 2-sun illumination, were performed in Figure 2.8. An initial CPC experiment was performed for 24 hours to determine the long-term behavior of OER on our WO_3 films. The measured rate of the OER (black) exhibits a decay with a profile similar to the theoretical rate (red). An average Faradaic efficiency of 74% results for this section. At the end of the 24-hour period, the film rested at open circuit in the dark for six hours, and the measured rate of the OER falls to zero, as expected. Following the open circuit rest in the dark, 0.98 V vs Ag/AgCl was reapplied under 2-sun illumination for another six hours. In this time period, the theoretical rate of the OER is slightly higher from where it ended in the previous CPC experiment, and measured rate trended towards the final value from the previous CPC experiment. The Faradaic efficiency in this 6-hour section is 68%. At the end of the second CPC experiment, the electrode was again left at open circuit, *but this time under 2-sun illumination.* During this time period, the measured rate of the OER is zero, as expected. The final CPC experiment was started at the end of the illuminated open-circuit rest period, and exhibits recovered photocurrent that is mirrored by a recovery in the measured rate of the OER with a Faradaic efficiency of 77%. The measured rate for this section peaked at a rate of 1.6 nmol O_2 $cm^{-2} \cdot s^{-1}$ and dropped to a rate of 0.8 nmol O_2 $cm^{-2} \cdot s^{-1}$ at the end of the 6-hour period. The recovery in photocurrent is consistent with the recovery seen in Figures 2.1 and 2.2.

Photochromic formation of H_xWO_3 species induces a recovery in photocurrent, which includes a concurrent recovery in OER activity.

Replicates of this experiment are presented as Figure A.13. The replicate trials show variability in Faradaic efficiency, but with the same trend in photocurrent recovery. In all cases, illuminating at open circuit induces a recovery in photocurrent by forming H_xWO_3, and subjecting the films to open circuit conditions in the dark results in no appreciable photocurrent recovery. Using the results from the three trials of the experiment in Figure 2.8, the Faradaic efficiency for each section was found to be $70 \pm 10\%$. During the four CPC cycles shown in Figure 2.2, the OER rate was also monitored (Figure A.14). For the first three CPC measurement, which took place after resting at OCP under illumination, the faradaic efficiency is 68%. Figure A.15 shows that after extended photoelectrolysis for 12 h, monoclinic WO_3 is still observed by XRD with no discernable chages to the film morphology by SEM imaging.

2.4. Conclusion

Our investigation into WO_3 activity was motivated by the exploring the effects of photochromism on the photoelectrochemical characteristics of WO_3 films used for the OER. Films prepared by spin coating from AMT start with intercalated protons introduced in the synthesis. They exhibit photocurrent decay during OER conditions, which results from oxidative deintercalation of these protons from H_xWO_3. The H_xWO_3 tungsten bronze makes up about 0.02% of the bulk material by mass. XPS and Mott-Schottky analysis affirms a decrease in W^{5+} during the OER. The rate of the OER decreases as the photocurrent density decays. However, photochromic reformation of H_xWO_3 at open circuit induces a recovery in the photocurrent density, showing that the loss in current density is due to the changing surface chemistry and not irreversible dissolution of the film. Improving the photoactivity of WO_3 will require stabilizing the electrochemically active donor species in the material in order to prevent their loss during operation.

References

[1] Sivula, K.; van de Krol, R. Semiconducting Materials for Photoelectrochemical Energy Conversion. *Nat. Rev. Mater.* **2016**, *1*, 15010.

[2] Lhermitte, C. R.; Garret Verwer, J.; Bartlett, B. M. Improving the stability and selectivity for the oxygen-evolution reaction on semiconducting WO_3 photoelectrodes with a solid-state FeOOH catalyst. *J. Mater. Chem. A* **2016**, *4*, 2960–2968.

[3] Alexander, B. D.; Kulesza, P. J.; Rutkowska, I.; Solarska, R.; Augustynski, J. Metal oxide photoanodes for solar hydrogen production. *J. Mater. Chem.* **2008**, *18*, 2298–2303.

[4] Maeda, K.; Higashi, M.; Lu, D.; Abe, R.; Domen, K. Efficient Nonsacrificial Water Splitting through Two-Step Photoexcitation by Visible Light using a Modified Oxynitride as a Hydrogen Evolution Photocatalyst. *J. Am. Chem. Soc.* **2010**, *132*, 5858–5868.

[5] Abe, R.; Higashi, M.; Domen, K. Overall Water Splitting under Visible Light through a Two-Step Photoexcitation between TaON and WO_3 in the Presence of an Iodate-Iodide Shuttle Redox Mediator. *ChemSusChem* **2011**, 228–237.

[6] Ma, S. S. K.; Maeda, K.; Abe, R.; Domen, K. Visible-light-driven nonsacrificial water oxidation over tungsten trioxide powder modified with two different cocatalysts. *Energy Environ. Sci.* **2012**, *5*, 8390–8397.

[7] Amano, F.; Li, D.; Ohtani, B. Fabrication and photoelectrochemical property of tungsten(VI) oxide films with a flake-wall structure. *Chem. Commun.* **2010**, *46*, 2769–2771.

[8] Wang, G.; Ling, Y.; Wang, H.; Yang, X.; Wang, C.; Zhang, J. Z.; Li, Y. Hydrogen-treated WO_3 nanoflakes show enhanced photostability. *Energy Environ. Sci.* **2012**, *5*, 6180–6187.

[9] Ji, X.; Ma, M.; Ge, R.; Ren, X.; Wang, H.; Liu, J.; Liu, Z.; Asiri, A. M.; Sun, X. WO_3 Nanoarray: An Efficient Electrochemical Oxygen Evolution Catalyst Electrode Operating in Alkaline Solution. *Inorg. Chem.* **2017**, *56*, 14743–14746.

[10] Hill, J. C.; Choi, K.-S. Effect of Electrolytes on the Selectivity and Stability of n-type WO3 Photoelectrodes for Use in Solar Water Oxidation. *J. Phys. Chem. C* **2012**, *116*, 7612–7620.

[11] Solarska, R.; Jurczakowski, R.; Augustynski, J. A highly stable, efficient visible-light driven water photoelectrolysis system using a nanocrystalline WO3 photoanode and a methane sulfonic acid electrolyte. *Nanoscale* **2012**, *4*, 1553–1556.

[12] Reinhard, S.; Rechberger, F.; Niederberger, M. Commercially Available WO_3 Nanopowders for Photoelectrochemical Water Splitting: Photocurrent versus Oxygen Evolution. *ChemPlusChem* **2016**, *81*, 935–940.

[13] Mi, Q.; Zhanaidarova, A.; Brunschwig, B. S.; Gray, H. B.; Lewis, N. S. A quantitative assessment of the competition between water and anion oxidation at WO_3 photoanodes in acidic aqueous electrolytes. *Energy Environ. Sci.* **2012**, *5*, 5694–5700.

[14] Takeda, H.; Adachi, K. Near Infrared Absorption of Tungsten Oxide Nanoparticle Dispersions. *J. Am. Ceram. Soc.* **2007**, *90*, 4059–4061.

[15] Bullett, D. W. Bulk and Surface Electron States in WO_3 and Tungsten Bronzes. *J. Phys. C: Solid State Phys.* **1983**, *16*, 2197–2207.

[16] Huang, R.; Shen, Y.; Zhao, L.; Yan, M. Effect of hydrothermal temperature on structure and photochromic properties of WO_3 powder. *Adv. Powder Technol.* **2012**, *23*, 211 – 214.

[17] Fleisch, T. H.; Mains, G. J. An XPS study of the UV reduction and photochromism of MoO_3 and WO_3. *J. Chem. Phys.* **1982**, *76*, 780–786.

[18] Bechinger, C.; Wirth, E.; Leiderer, P. Photochromic coloration of WO_3 with visible light. *Appl. Phys. Lett.* **1996**, *68*, 2834–2836.

[19] Gavrilyuk, A. Photochromism in WO_3 thin films. *Electrochim. Acta* **1999**, *44*, 3027–3037.

[20] Thummavichai, K.; Xia, Y.; Zhu, Y. Recent progress in chromogenic research of tungsten oxides towards energy-related applications. *Prog. Mater. Sci.* **2017**, *88*, 281 – 324.

[21] Gupta, T. *Copper Interconnect Technology*, 1st ed.; Springer-Verlag New York, 2009.

[22] Biaggio, S. R.; Rocha-Filho, R. C.; Vilche, J. R.; Varela, F. E.; Gassa, L. M. A study of thin anodic WO_3 films by electrochemical impedance spectroscopy. *Electrochim. Acta* **1997**, *42*, 1751 – 1758.

[23] Oskam, G.; Vanmaekelbergh, D.; Kelly, J. A reappraisal of the frequency dependence of the impedance of semiconductor electrodes. *J. Electroanal. Chem. Interf. Electrochem.* **1991**, *315*, 65 – 85.

[24] Hakiki, N.; Boudin, S.; Rondot, B.; Da Cunha Belo, M. The electronic structure of passive films formed on stainless steels. *Corros. Sci.* **1995**, *37*, 1809 – 1822.

[25] Sikora, J.; Sikora, E.; Macdonald, D. D. The electronic structure of the passive film on tungsten. *Electrochim. Acta* **2000**, *45*, 1875 – 1883.

[26] Nyikos, L.; Pajkossy, T. Fractal dimension and fractional power frequency-dependent impedance of blocking electrodes. *Electrochim. Acta* **1985**, *30*, 1533 – 1540.

[27] Harrington, S.; Devine, T. Analysis of Electrodes Displaying Frequency Dispersion in Mott-Schottky Tests. *J. Electrochem. Soc.* **2008**, *155*, 381 – 386.

[28] Brug, G.; van den Eeden, A.; Sluyters-Rehbach, M.; Sluyters, J. The analysis of electrode impedances complicated by the presence of a constant phase element. *J. Electroanal. Chem. Interf. Electrochem.* **1984**, *176*, 275 – 295.

[29] Hatsukade, T.; Kuhl, K. P.; Cave, E. R.; Abram, D. N.; Jaramillo, T. F. Insights into the electrocatalytic reduction of CO_2 on metallic silver surfaces. *Phys. Chem. Chem. Phys.* **2014**, *16*, 13814 – 13819.

[30] Anik, M.; Cansizoglu, T. Dissolution kinetics of WO_3 in acidic solutions. *J. Appl. Electrochem.* **2006**, *36*, 603 – 608.

[31] Macdonald, D.; Sikora, E.; Sikora, J. The kinetics of growth of the passive film on tungsten in acidic phosphate solutions. *Electrochim. Acta* **1998**, *43*, 2851–2861.

[32] Wen, R.; Granqvist, C.; Niklasson, G. Eliminating degradation and uncovering ion-trapping dynamics in electrochromic WO_3 thin films. *Nat. Mater.* **2015**, *14*, 996 – 1001.

[33] Wen, R.; Arvizu, M.; Luna, M.; Granqvist, C.; Niklasson, G. Ion Trapping and Detrapping in Amorphous Tungsten Oxide Thin Films Observed by Real-Time Electro-Optical Monitoring. *Chem. Mater.* **2016**, *28*, 4670–4676.

[34] Baloukas, B.; Arvizu, M.; Wen, R.; Niklasson, G.; Granqvist, C.; Vernhes, R.; Klemberg-Sapieha, J.; Martinu, L. Galvanostatic Rejuvenation of Electrochromic WO_3 Thin Films: Ion Trapping and Detrapping Observed by Optical Measurements and by Time-of-Flight Secondary Ion Mass Spectrometry. *ACS Appl. Mater. Interfaces* **2017**, *9*, 16995–17001.

[35] Hunyadi, D.; Sajó, I.; Szilágyi, I. Structure and thermal decomposition of ammonium metatungstate. *J. Therm. Anal. Calorim.* **2013**, *116*, 329–337.

Chapter 3.

Evaluating Chloride Oxidation as an Alternative to the Oxygen Evolution Reaction on H_xWO_3

3.1. Introduction

Production of solar fuels has largely focused on proton reduction at the cathode to form H_2 and gathering the re-quired at the anode through the oxygen evolution reaction (OER).

$$2\,H^+(aq) + 2\,e^- \longrightarrow H_2(g) \qquad E^\circ = 0\ V_{\,SHE} \tag{3.1}$$

$$2\,H_2O\,(l) \longrightarrow 4\,H^+(aq) + 4\,e^- + O_2(g) \qquad E^\circ = 1.23\ V_{SHE} \tag{3.2}$$

However, while the water oxidation produces no greenhouse gasses, the commercial value of the O_2 product is low, the thermodynamic potential for water oxidation is high (1.23 V vs RHE), and the reaction is slow due to multiproton, multi-electron nature of the reaction. Furthermore, carrying out the OER on different electrochemical and photoelectrochemical platforms typically exhibits significant degradation which limits the long-term viability of OER for solar fuel production. Degradation mechanisms include changes in oxidation state, dissolution, and migration of the active material.[1–3] Alternatives to the OER are then important, particularly those which produce valuable oxidation products at stable current densities. Examples include the oxidation of organic species like 5-hydroxymethylfurfural to 2,5-diformylfuran or the formation of various oxidation reagents like persulfate and sodium hypochlorite.[4–6]

The oxidation of chloride anion is an attractive alternative due to the large amounts of brine water on earth and the rapid kinetics of the two-electron oxidation of chloride to

chlorine or hypochlorite.[7–9]

$$2\,Cl^-(aq) \longrightarrow Cl_2(g) + 2\,e^- \qquad E^\circ = 1.36\ V_{SHE} \tag{3.3}$$

$$Cl^-(aq) + H_2O\,(l) \longrightarrow ClO^-(aq) + 2\,H^+(aq) + 2\,e^- \qquad E^\circ = 1.72\ V_{SHE} - 0.0591\ V \cdot pH \tag{3.4}$$

Chloride oxidation is industrially performed by the chloralkali process to produce Cl_2 gas and NaOH, both of which are required for over 50% of industrial chemical processes.[10] Apart from strongly acidic aqueous solutions, Cl_2 reacts in aqueous environments to produce hypochlorite anion in basic solutions or hypochlorous acid in more acidic conditions ($pK_a = 7.4$).[11]Also, recent work in our group has shown that the OER on H_xWO_3 proceeds by formation of hydroxyl radical species which means that the reaction competing against chloride oxidation is the formation of hydroxyl radical.[12,13]

$$H_2O\,(l) \longrightarrow OH^\bullet(aq) + H^+(aq) + e^- \qquad E^\circ = 2.7\ V \text{ vs RHE} \tag{3.5}$$

Chloride oxidation may proceed through a radical species as well.[13]

$$Cl^-(aq) \longrightarrow Cl^\bullet(aq) + e^- \qquad E^\circ = 2.\ V \text{ vs RHE} \tag{3.6}$$

However, the hydroxyl radical reduction potential is at a more positive potential than the chloride radical reduction potential. Therefore, chloride oxidation is expected to be the thermodynamically favored reaction on H_xWO_3 regardless if formation of a chloride radical is required in the chloride oxidation mechanism.

In this chapter, the oxidation of chloride by tungsten oxide generated by sol-gel processing, whose chemistry is best described as the formula H_xWO_3 in pH 4 solutions is demonstrated.[2] The valence band of H_xWO_3 (3.1 V vs NHE) is sufficiently positive to provide the overpotential required for the oxi-dative reactions presented in Equations 3.2-3.11.[14] Chloride oxidation is also kinetically simpler, requiring only the formation of a single σ bond compared to the σ and π bonds which must be formed during O_2 evolution. The kinetic and thermodynamic advantage of chloride oxidation allows for faster rates of hole transfer compared to water oxidation. The substantial increase in stability of H_xWO_3 photoactivity during chloride oxidation is a result of the rapid

electron injection from chloride preventing a build-up of surface holes which can cause deleterious side-reactions such as oxidation of donor species. This hypothesis is supported by demonstrating high stability of H_xWO_3 during oxidation of sodium sulfite, a rapid oxidation substrate, and application of an FeOOH electrocatalyst which shows similar enhancements in stability. FeOOH electrocatalysts are known for efficient hole collection when layered on metal oxide light absorbers.[15–17]

3.2. Experimental

3.2.1. Chemicals

In all experiments, the water was filtered by a Millipore filtration system (18.2 MΩ $\cdot$ cm^{-1}). Ethanol (200 proof) was purchased from Decon Laboratories. Phosphoric acid (85 w/w%) was purchased from EMD Millipore. Ammonium metatungstate $(NH_4)_6H_2W_{12}O_{40} \cdot xH_2O$ (AMT), poly(ethylene glycol) M_w = 300 Da, PEG-300), 1000 ppm ICP standards for iron, hydrogen peroxide (30% w/w), sodium chloride, and potassium sulfate, were purchased from Sigma Aldrich. The $FeSO_4 \cdot 7\,H_2O$ was purchased from the JT Baker Chemical Company and purified by dissolving in 0.5 M H_2SO_4 at 50 °C and then precipitated with ethanol. The crystallites were separated from the mother liquor with a Buchner funnel and then washed with ice water. The purified $FeSO_4 \cdot 7\,H_2O$ crystallites were spread in a Petri dish and allowed to dry overnight in the back of a fume hood. Fluorine tin oxide (FTO, Pilkington Glass TEC-15) substrate was cut into 2.54 × 2.54 cm^2 squares for H_xWO_3 spin coat synthesis. FTO substrate was first coarsely cleaned by scrubbing with an acetone wetted Kimwipe™. This cleaning procedure was followed by sonicating in the following solvents: acetone, Sparkleen™ detergent, water, and acetone again for 10 minutes each, with each solvent wash followed by drying under a flowing N_2 stream. Ag/AgCl reference electrodes were purchased from CH Instruments and filled with saturated KCl aqueous solution. 99.95% pure Pt wire (24 gauge, P/N 1981) was purchased from Sure Pure Chemetals.

3.2.2. Synthesis of H_xWO_3 Electrodes

H_xWO_3 electrodes were synthesized by spin coating using a procedure previously reported which can also be found in Chapter 2.[2] Spin coat solution was made by adding

2.51 g (833 μmol) AMT to a 100 mL round bottom and then adding 10 mL of water to dissolve completely with vigorous stirring. Separately, 6.6 g (22 mmol) of PEG-300 was dissolved in 10 mL of ethanol in a scintillation vial. The ethanol solution was slowly added to the aqueous solution by pipette while stirring vigorously over the course of approximately 3 minutes, resulting in a faint, off-white sol precursor, which was 0.5 M in tungsten. Electrodes for PEC measurements were prepared by dropping 200 μL of precursor sol onto clean, 2.54 cm squares (6.45 cm^2) of FTO and then spun at 2500 rpm for 30 seconds using a Laurel spin coater. After spin coating a layer, the film was placed into a 500 °C muffle furnace for thirty minutes. The spin coat and anneal procedure was repeated for a total of ten times to make the 1 μm thick films used in this work. The H_xWO_3 electrodes used in the detection of oxidized chloride products by the starch-iodide test were 1.5 cm squares (2.25 cm^2) and prepared in an identical manner except 70 μL of precursor sol was dropped onto a 2.25 cm^2 area masked off on a 1.5 cm $\times$ 2.54 cm piece of FTO.

3.2.3. Materials Characterization

XRD was recorded with a Panalytical Empyrean diffractometer at a power of 1.8 kW (45 kV, 40 mA) using Cu Kα ($\lambda = 1.5418\,$Å) in $\theta-\theta$. XPS was collected using a Kratos Axis Ultra X-ray photoelectron spectrometer. The X-rays used were monochromatic Al K Kα X-rays (1486.7 eV) and measurements performed at an analysis chamber pressure of $\approx 1 \cdot 10^{-9}$ Torr. An electron flood gun was used to compensate for charging during data collection. Casa XPS software was used with a Shirley-type baseline to calculate the peak areas; binding energies were determined by setting adventitious carbon signal to 248.8 eV. UV-Vis measurements were performed using a Cary 5000 spectrophotometer (Agilent) in reflectance mode with an integration sphere for diffuse reflectance. Solution UV-Vis measurements were performed in absorbance mode using a 700 µL micro cuvette. Transmission electron microscopy samples were prepared using a FEI Helios 650 Nanolab Focused Ion Beam (FIB) workstation. Transmission electron micrographs were collected with either a JEOL 2010F field emission analytical microscope operated at an acceleration voltage of 200 kV in parallel beam (TEM) mode or a Thermo Fisher Talos F200X G2 S/TEM operated in either TEM or STEM mode at 200 kV. Images were collected without insertion of condenser or intermediate lens apertures. However,

an objective aperture was used to enhance contrast during imaging. A Gatan *One View* camera was used for TEM image acquisition and HAADF detector for STEM imaging. Energy Dispersive X-Ray Spectroscopy (EDS) data was collected using a JEOL 2100 Probe-Corrected Analytical Electron Microscope in STEM mode at 200 kV.

3.2.4. Photodeposition of FeOOH Electrocatalyst

A galvanostatic anodic deposition technique was used to deposit the FeOOH electrocatalyst onto the H_xWO_3 semiconductor. A 405 nm LED light source was used to backside illuminate the H_xWO_3 light absorber during deposition at an intensity of 100 mW $\cdot$ cm^{-2}. The deposition solution was composed of 10 mM $FeSO_4 \cdot 7\,H_2O$ in 0.1 M Na_2SO_4 at pH 4.5. The exposed electrode area was 4.3 cm^2 and an anodic current density of 75 µA $\cdot$ cm^{-2} was passed for 1000 seconds. The deposition cell used was single compartment compression sealed cell machined from PVC plastic.

3.2.5. Photoelectrochemistry

All photoelectrochemistry was performed using a CH Instruments Series 760E electrochemical workstation and a Newport-Oriel 150 W Xe arc lamp affixed with an AM 1.5 G simulating solar filter (Newport , P/N 81094). Pt wire was used as a counter electrode and the reference electrode used was Ag/AgCl in saturated KCl with a Vycor frit. The power density was adjusted by using a thermopile detector (Newport, P/N 818P-015-19) and an optical power meter (Newport, P/N 1918-R). The cell used was a custom-designed compression cell that has been described previously.[2] During measurements of oxygen production, a Nafion™ membrane was inserted to separate the working electrode compartment from the counter electrode compartment and prevent reduction of oxygen on the platinum counter electrode.

3.2.6. Detection of Oxidized Chloride Products

To determine whether oxidation of Cl^- is the predominate reaction occurring on the surface of H_xWO_3 during controlled potential coulometry (CPC) in 0.5 M sodium chloride electrolyte, a starch-iodine test was used. This test is sensitive to both dissolved Cl_2 and hypochlorous acid. A two-compartment cell was used with a Nafion™ mem-

brane separating the two halves and 35 mL of pH 4, 0.5 M sodium chloride electrolyte was used in each compartment. The working electrode compartment was sealed tightly before starting the experiment. A 1-hour CPC experiment was then carried out at 1.23 V vs RHE under 2-sun AM 1.5 G illumination. Following CPC, 25 mL of the resulting working compartment electrolyte was removed and combined with potassium iodide to make a solution with an I^- concentration of 50 mM. The potassium iodide reacts with dissolved Cl_2 according to the equation

$$2\,I^-(aq) + Cl_2(aq) \longrightarrow I_2(aq) + 2\,Cl^-(aq) \tag{3.7}$$

or hypochlorous acid according to

$$HClO\,(aq) + 2\,I^-(aq) + H^+(aq) \longrightarrow Cl^-(aq) + I_2(aq) + H_2O\,(l) \tag{3.8}$$

In both reactions, there is a 1:1 correspondence between the 2-electron chloride oxidation product (Cl_2 or HClO) and I_2. From this resulting 25 mL solution, 5 mL was titrated with 10 mM $Na_2S_2O_3$ and a starch indicator. The thiosulfate reduces the generated iodine according to the equation

$$I_2(aq) + 2\,{S_2O_3}^{2-}(aq) \longrightarrow 2\,I^-(aq) + {S_4O_6}^{2-}(aq) \tag{3.9}$$

3.3. Results and Discussion

3.3.1. Film Composition and Morphology

Intercalated protons with associated W^{5+} donor states lead us to write the formula as H_xWO_3 for the synthesized films.[2] However, H_xWO_3 is not electrochemically innocent, and W^{+5} can be oxidized to W^{+6} with simultaneous deintercalation of protons into solution according to the reaction:

$$H_xWO_3(s) \longrightarrow WO_3(s) + xH^+(aq) + xe^- \tag{3.10}$$

The UV-Vis diffuse reflectance is shown in Figure B.1 in the appendix. The absorption onset begins a 450 nm and peaks at 364 nm. An FeOOH electrocatalyst was deposited onto H_xWO_3 from iron(II) sulfate in pH 4 solution to investigate mechanism by which the

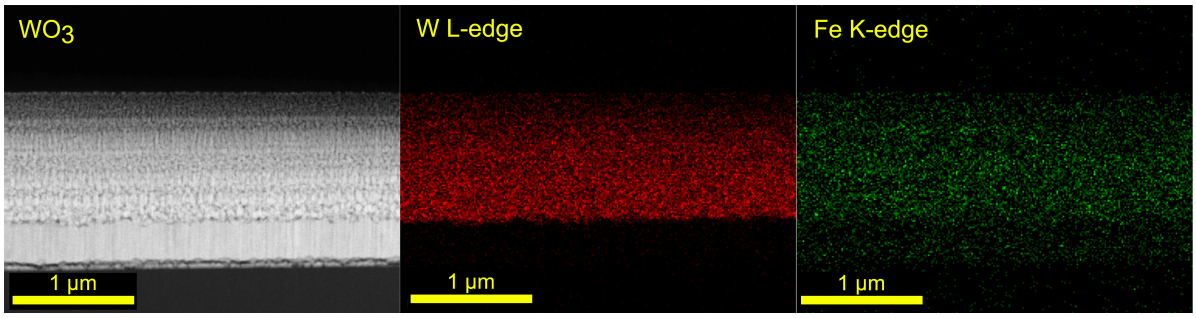

Figure 3.1: Side-on EDS mapping of FeOOH deposited onto H_xWO_3. Signal from the Fe Kα transition can be detected throughout the entirety of the oxide layers. An Fe impurity is also detected in the FTO layer.

photocurrent density may be stabilized. The deposited iron electrocatalyst is amorphous by XRD (Figure B.2) and ICP-MS analysis shows an initial iron loading of 0.237 $\pm$ 0.003 μmol $Fe^{3+} \cdot cm^{-2}$ on H_xWO_3. The side-on EDS maps in Figure 3.1 show that the iron is distributed throughout the entire film thickness, extending from the top surface of the film down to the FTO substrate. The deposition of FeOOH does not change the morphology of the underlying semiconductor film (Figure B.3) by TEM, with no obvious features appearing after FeOOH deposition. XPS analysis of the H_xWO_3 and H_xWO_3|FeOOH film surface is shown in Figure B.4 of the appendix. The H_xWO_3 W(4f) W^{+5} and W^{+6} signals are observed. Following deposition of FeOOH, the W(4f) W^{+5} signal is not distinguishable, indicating that the surface W(4f) W^{+5} was oxidized during FeOOH deposition. The H_xWO_3 O(1s) signal shows two species for the metal oxide oxygens as well as a road signal for oxygen from the adventitious carbon. After deposition of FeOOH, a new O(1s) signal is seen and assigned to the FeOOH oxygen species. Fe(2p) signal is also observed, and the intensity of the Fe(2p) signal does not noticeably change or decrease after CPC operation in NaCl and KP_i electrolyte.

3.3.2. Water Oxidation at pH 4

H_xWO_3 based films were analyzed in pH 4 solutions of 0.1 M potassium phosphate buffer. Flow-cell gas chromatography (GC) was used to measure the faradaic efficiency of the OER (FE_{OER}). The left axis of Figure 3.2 corresponds to the rate of OER measured by GC (solid traces) while the right axis corresponds to the measured current density (dashed traces). The data in black correspond to that recorded on H_xWO_3;

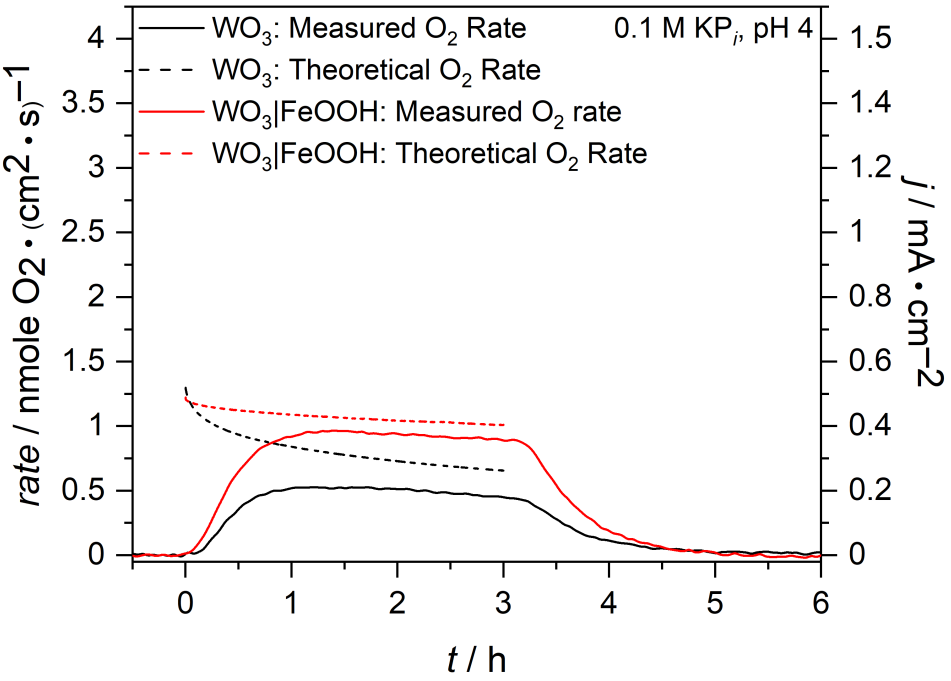

Figure 3.2: The OER activity on H_xWO_3 (black) and H_xWO_3|FeOOH (red) at 1.23 V vs RHE with AM 1.5 G illumination in 0.1 M KP_i buffer at pH 4. The current density measured during CPC (right axis) was converted to rate of OER (left axis) for the theoretical rate (dashed traces). The measured rate (solid traces) was determined by flow cell gas chromatography.

FE_{OER} measured from three trials is 67 ± 2%, similar to what we previously reported for H_xWO_3 in a pH 1 sulfuric acid solution (70 ± 10%).[2] The starting photocurrent density is 0.48 ± 0.02 mA · cm^{-2}, and its decreased by half to 0.24 ± 0.03 mA · cm^{-2} after three hours of CPC at 1.23 V vs RHE. As was seen previously with sulfate electrolyte, using a phosphate-based electrolyte results in the loss of photocurrent, consistent with the reaction in Equation 5.3.[2]

After forming H_xWO_3|FeOOH, the OER activity was measured again in a pH 4 0.1 M KP_i solution. The red traces of Figure 3.2 show a starting photocurrent density of 0.46 ± 0.03 mA · cm^{-2}, which decreases by 16% to 0.39 ± 0.01 mA · cm^{-2}, a less severe loss of photocurrent than seen with H_xWO_3 alone. Increased stability of H_xWO_3 following deposition of FeOOH has been reported before by our group previously, although the exact mechanism was uncertain at the time.[18] The FeOOH electrocatalyst increased FE_{OER} to 93 ± 2%, but resulted in no increase in the starting photocurrent density. This result

suggests that the rate of hole transfer on FeOOH is not substantially faster than on H_xWO_3 itself; however, FeOOH does reduce the overpotential for the OER as evidenced by the increase in FE_{OER}. This increase in reaction selectivity hints at a change in mechanism, which our group recently confirmed. OER on H_xWO_3 proceeds through a hydroxyl radical species (Equation 3.5) while OER on FeOOH and H_xWO_3|FeOOH does not form any detectable hydroxyl radical.[12] The formation of hydroxyl radical requires a large applied poten-tial (2.7 V), however FeOOH does not require this inter-mediate to preform OER, allowing for rapid removal of holes from the underlying H_xWO_3 because the formation of a high energy intermediate is bypassed. With a pathway for rapid removal of holes from H_xWO_3, the loss of donor species through Equation 5.3 is suppressed.

ICP-MS analysis showed the iron loading was initially 0.237 ± 0.003 moles Fe^{3+} · cm^{-2} after iron deposition and decreased to 0.103 ± 0.001 moles Fe^{3+} · cm^{-2} after the three-hour CPC at 1.23 V vs RHE. While the Fe content decreased by over 50% during the three-hour CPC experiment, the photocurrent only decreased by 16% and the measured rate of OER exhibited a similar amount of decay indicating that both the overall photoactivity and measured rate of OER do not show a strong linear relationship with the Fe loading. From this we conclude that not all the deposited iron contributes to the observed photoactivity occurring. XPS data (Figure B.4, appendix) shows that the Fe(2p) signal is still present following CPC in KP_i with no appearance of a shoulder at lower binding energies, indicating that no reduced Fe^{2+} resulted from OER operation.

3.3.3. Chloride Oxidation at pH 4

The propensity for H_xWO_3 and H_xWO_3|FeOOH to carry out chloride oxidation was measured in 0.5 M sodium chloride solution set to pH 4 with hydrochloric acid. A 0.1 M KP_i buffer could not be used because performing photoelectrochemical oxidation in a KP_i and chloride containing solution results in the complete loss of H_xWO_3 from the FTO substrate, likely due to hypochlorous acid facilitating the formation of water soluble phosphotungstate species. The rate of OER was measured in the chloride electrolyte to determine the extent of chloride oxidation. Because the only species in solution active towards oxidation are water and chloride anions, the suppression of the OER when moving to chloride electrolytes suggests that chloride is oxidized preferentially.

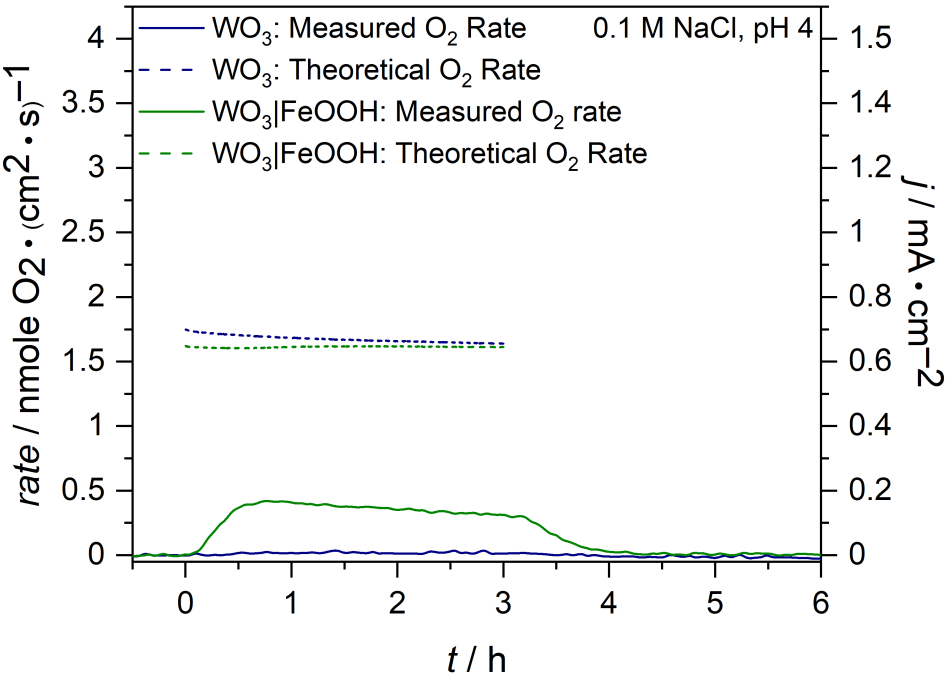

Figure 3.3: The OER activity on H_xWO_3 and H_xWO_3|FeOOH in 0.5 M NaCl at pH 4. CPC performed at 1.23 V vs RHE with AM 1.5 G illumination. The addition of chloride suppresses the OER measured by GC. Other experimental conditions and graphical notations are the same as those described in the caption of Figure 3.2.

Figure 3.3 shows that FE_{OER} on H_xWO_3 in salt water is only $2 \pm 1\%$, hinting that hole transfer between H_xWO_3 and the solution is occurring by chloride oxidation. This was confirmed by using a starch–iodine test to detect oxidized chloride species. Comparing the total charge passed during the CPC experiment (4.3 C, CPC shown in Figure B.5 of the appendix) against the volume of 10 mM thiosulfate titrated (320 ± 2 µL) shows that H_xWO_3 faradaic efficiency for the two-electron oxidation of chloride is 100% in pH 4, 0.5 M NaCl electrolyte with no OER occurring. This result is in agreement with previous work.[19,20] The solution UV-Vis of the working compartment 0.5 M electrolyte is shown in Figure B.6 of the supporting information and suggests that the predominant product formed is likely hypochlorous acid. The λ_{max} for Cl_2, HClO and ClO^- are 229 nm, 233 nm, and 290nm, respectively.[21] While the λ_{max} for Cl_2 and HClO are close in wavelength, at a pH of 4 we do not expect Cl_2 to be formed.

Because OER on H_xWO_3 requires the formation of hydroxyl radical to proceed on the H_xWO_3 surface, the oxidation of chloride has both a kinetic and thermodynamic advan-

tage over water oxidation on the bare H_xWO_3 electrode. The current density starts at 0.60 ± 0.10 mA $\cdot$ cm^{-2} and decreases by 5% to 0.57 mA $\pm$ 0.08 mA $\cdot$ cm^{-2}. An increase in stability in salt water is observed because of the rapid rate with which chloride can inject electrons into H_xWO_3, which prevents the oxidative proton deintercalation reaction to form to HxWO3 (Equation 5.3).

The FeOOH electrocatalyst was again used to investigate hole transfer on H_xWO_3. After deposition of an iron electrocatalyst (Figure 3.3, red traces), the total photocurrent in 0.5 M NaCl is essentially unchanged while FE_{OER} increases to 23 $\pm$ 1%. The initial photocurrent is 0.57 ± 0.06 mA $\cdot$ cm^{-2} and shows good stability, ending at 0.57 ± 0.06 mA $\cdot$ cm^{-2} after three hours. The FeOOH electrocatalyst reduces the overpotential for OER, increasing the rate of OER by directing a larger percentage of surface holes toward oxygen evolution. As a control experiment, the FeOOH electrocatalyst was deposited on clean FTO with no light absorbing layer and exhibited FE_{OER} of 23% (Figure B.7, appendix) in a solution of 0.5 M NaCl at pH 4. Our results show that the H_xWO_3 surface exhibits near zero preference for water oxidation in the presence of chloride ion while H_xWO_3|FeOOH exhibits the same FE_{OER} as the FeOOH control in 0.5 M NaCl at pH 4.

Together, these results suggest that FeOOH is capable of rapidly removing holes away from the H_xWO_3-solution interface such that chemistry occurs at the FeOOH-solution interface. If hole transfer were still occurring at the H_xWO_3-solution interface, the FE_{OER} would be expected to follow the following relationship

$$\eta_{\text{Faradaic}} = 0.02(1-\theta) + 0.23 \cdot \theta \tag{3.11}$$

where θ is the surface coverage of the iron catalyst and 0.02 and 0.23 are the faradaic efficiencies of H_xWO_3 and FeOOH in 0.5 M NaCl at pH 4, respectively. However, the behavior we observe is consistent with complete surface coverage ($\theta = 1$) despite a low quantity of iron catalyst loading. ICP–MS shows an initial loading of 0.23 ± 0.02 μmole Fe $\cdot$ cm^{-2} and XPS analysis (Figure B.4) shows minimal attenuation of the W(4f) signal, indicating that FeOOH surface coverage is low. The OER activity data in Figures 3.2 and 3.3 are representative of the other two trials shown in the appendix (Figure B.8).

3.3.4. Sulfite oxidation on H_xWO_3

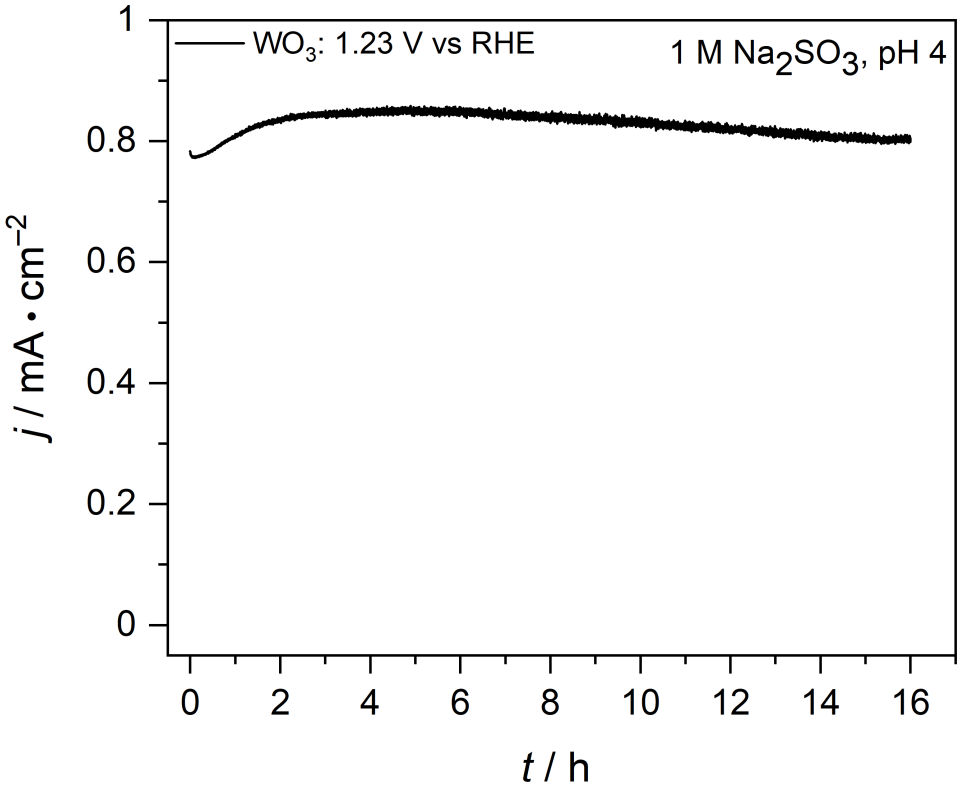

Figure 3.4: 16-hour CPC experiment of H_xWO_3 poised at 1.23 V vs RHE under AM 1.5 G illumination in 1 M Na_2SO_3 at pH 4.

Sodium sulfite is a redox active species with rapid oxidation kinetics, similar to chloride oxidation. Figure 3.4 shows the CPC trace of H_xWO_3 in a 1 M Na_2SO_3 at 1.23 V vs RHE for sixteen hours. Sulfuric acid was used to set the solution to a pH of 4. Over sixteen hours, the photocurrent density does not show the large decay that we observe when the OER is the dominant reaction. Moreover, the linear sweep voltammetry (LSV) trace taken after this sixteen-hour experiment shows a more negative photocurrent onset potential and a very slight increase in the saturated photocurrent density when compared to the initial LSV trace recorded (Figure B.9). These two features indicate that the rate of electron injection from sulfite anion is fast enough that H_xWO_3 material is actually slightly *reduced* rather than oxidized during this reaction. Improvement in the photoelectrochemical stability of light absorbing electrodes by the careful selection of

substrate has been demonstrated before with cadmium chalcogenide electrodes. Photoelectrochemical stability of the cadmium chalcogenide light absorbers can be significantly enhanced by addition of aqueous reducing agents such as hydroquinone, iodide, and sulfite.[22–24] These substrates improve photoelectrochemical stability by rapidly injecting electrons into the material, eliminating holes from oxidizing the cadmium chalcogenide light absorber before the active material could be oxidized. The enhancement in stability was shown to trend with the reduction potential of the oxidized substrate. The more negative the substrate Ox/Red reduction potential (Red being the oxidation substrate), the greater the enhancement in the photoelectrochemical stability.[25] The results from the cadmium chalcogenide light absorbers translates to H_xWO_3, where we observed increased stability by providing a thermodynamically more favorable oxidation substrate over liquid water, either chloride or sulfite.

Chloride oxidation improves the PEC photocurrent stability in the same fashion as sulfite oxidation. The shift in FE_{OER} from 67% to 2% when switching from phosphate to chloride electrolyte supports this assertion; chloride oxidation proceeds much faster than water oxidation in 0.5 M chloride electrolyte. This shift in FE_{OER} is accompanied by a significant increase in stability. Both the ClO^-/Cl^- and $Cl^\bullet/Cl^-$ couples are more negative than the $OH^\bullet,H^+/H_2O$ couple, providing a thermodynamic preference for chloride oxidation and allowing for rapid elimination of valence-band holes before they can perform the slower water oxidation reaction.

3.3.5. Mechanistic Implications of FeOOH for H_xWO_3 in Acidic and Saline Solution.

Figure 3.5 shows the LSV traces recorded before and after the CPC experiments on H_xWO_3. The initial H_xWO_3 LSV recorded in 0.1 M KP_i (solid black trace) shows a photocurrent onset at $\approx$ 0.2 V vs Ag/AgCl, and saturates at 0.80 V vs Ag/AgCl, which is approximately 1.23 V vs RHE. Following the three-hour CPC at 1.23 V vs RHE in 0.1 M KP_i, the LSV response of H_xWO_3 (dashed black trace) shows a similar profile but at a much lower current density at all potentials, and the curve shifts to a more positive potential for all features in the current profile. The current density at 0.80 V vs Ag/AgCl was initially 0.48 mA $\cdot$ cm^{-2} and decreased to 0.27 mA $\cdot$ cm^{-2} at the same

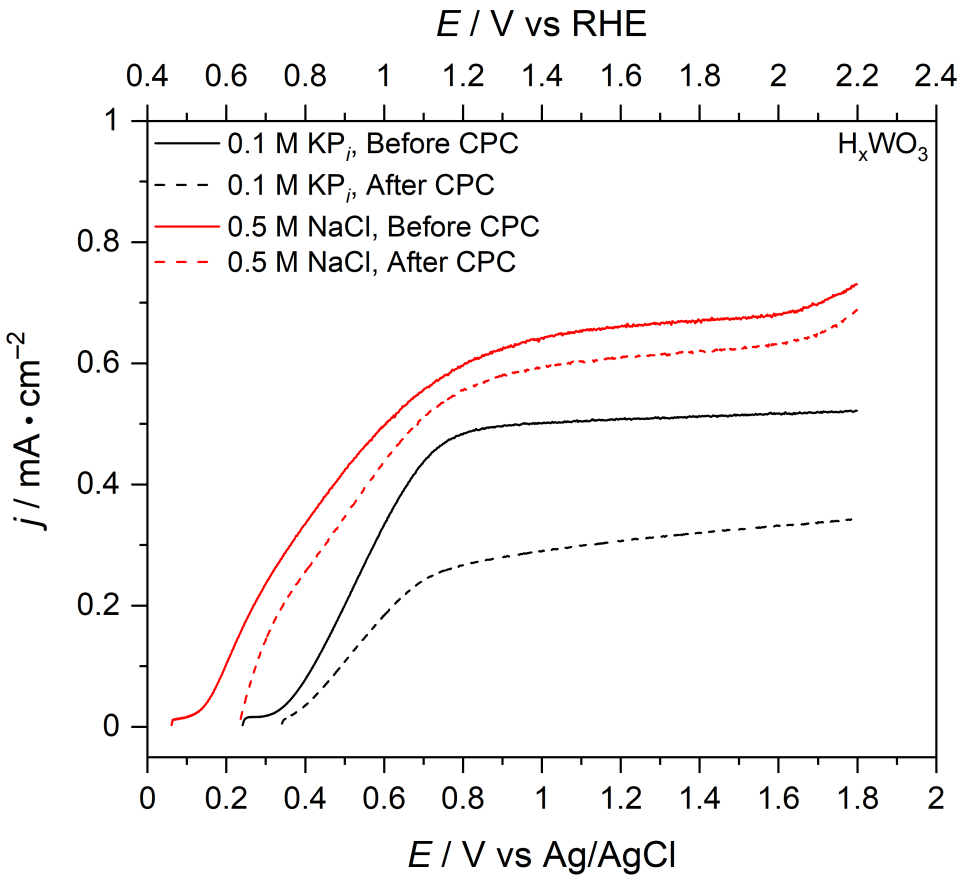

Figure 3.5: LSV traces recorded in the same electrolyte as the CPC exper-iment plots of H_xWO_3 before (solid lines) and immediately after (dashed lines) three-hour CPC at 1.23 V vs RHE under AM 1.5 G illumination. The electrolytes are 0.1 M KP_i (black) and 0.5 M NaCl (red) at pH 4.

potential due to the oxidation of H_xWO_3 donor impurities during the CPC experiment. The loss of H_xWO_3 donor species also results in the positive shift in current onset potential as well as a lower saturated photocurrent density.

When the electrolyte contains 0.5 M NaCl, the initial LSV for H_xWO_3 (solid red trace) shows a more negative photocurrent onset potential due to the lower overpotential requirements for chloride oxidation on H_xWO_3. The photocurrent at 0.8 V vs Ag/AgCl is initially 0.60 mA $\cdot$ cm^{-2}, and is approaching saturation, although the start of this limit is less well defined as it is in the case of H_xWO_3 OER in 0.1 M KP_i. Following three-hour CPC of WO3 at 1.23 V vs RHE in 0.5 M NaCl, the LSV response (dashed

red trace) shows a similar profile and a photocurrent that is 0.55 mA · cm^{-2} at 0.80 V vs Ag/AgCl. The loss of saturated photocurrent is not as severe when compared to when the electrolyte was 0.1 M KP_i.

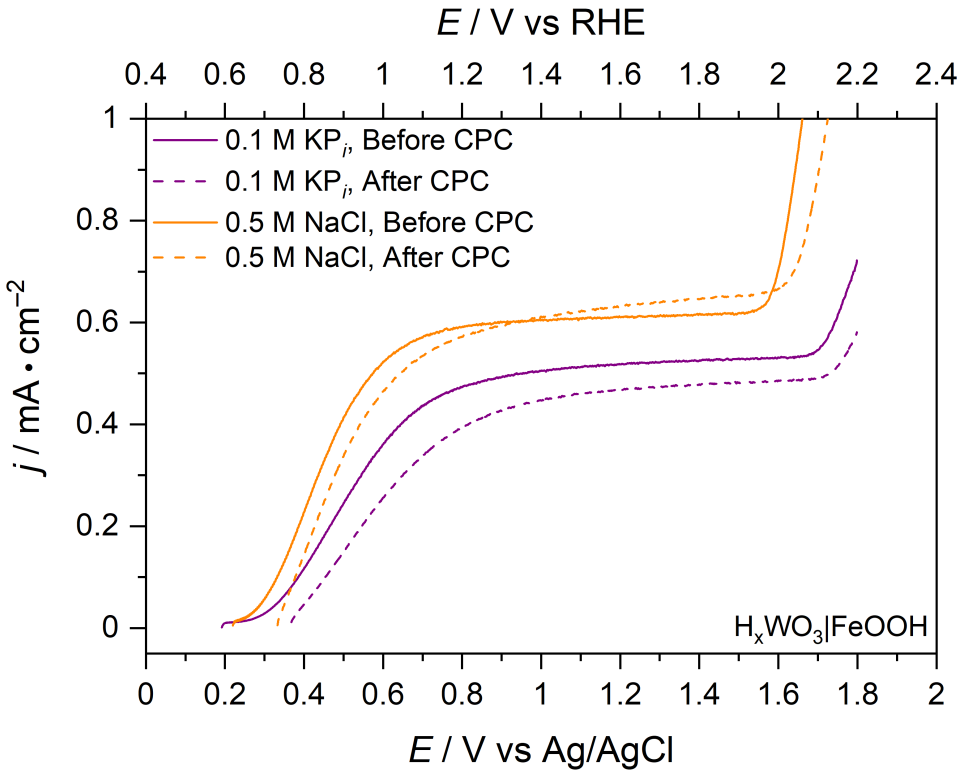

Figure 3.6: LSV traces recorded in the same electrolyte as the CPC experiment plots of H_xWO_3|FeOOH before (solid lines) and immediately after (dashed lines) three-hour CPC at 1.23 V vs RHE under AM 1.5 G illumination. The electrolytes are 0.1 M KP_i (purple) and 0.5 M NaCl (orange) at pH 4.

Figure 3.6 shows improved stability in H_xWO_3 photocurrent with deposition of the FeOOH electrocatalyst. The LSV traces are recorded before and after the CPC experiments on H_xWO_3|FeOOH 0.1 M KP_i (purple traces) and 0.5 M NaCl (orange traces). With FeOOH deposited, the onset potential converged to 0.2 V vs Ag/AgCl for both electrolyte solutions. When 0.1 M KP_i is the electrolyte, the initial current density (solid purple trace) at 0.8 V vs Ag/AgCl is 0.47 mA · cm^{-2} and decreased to 0.39 mA · cm^{-2} (dashed purple trace) after three-hours of CPC at 1.23 V vs RHE in the phosphate electrolyte. This loss of photocurrent density was less than what was seen with

H_xWO_3 in the same electrolyte, due to the removal of surface holes by FeOOH which prevented oxidation of H_xWO_3 donor sites. Adding 0.5 M NaCl to the electrolyte with H_xWO_3|FeOOH results in the smallest change in LSV trace before- and after CPC due to a combination of surface hole removal by FeOOH and by fast chloride oxidation. The initial photocurrent at 0.80 V vs Ag/AgCl is 0.59 mA $\cdot$ cm^{-2}, and shows a very slight decrease to 0.57 mA $\cdot$ cm^{-2} after three-hours of CPC at 1.23 V vs RHE, highlighting the preservation of donor sites in H_xWO_3 by chloride oxidation.

The LSV results in Figures 3.5 and 3.6 are summarized by the scheme shown in Figure 3.7. When interfacial hole transfer is slow, a build-up of photogenerated holes occurs on the surface of H_xWO_3. The oxidation of tungsten bronze donors is then able to proceed through recombination of electron density from the bronze donor and the photogenerated hole. The kinetics of water oxidation at the surface of H_xWO_3 with potassium phosphate electrolyte at pH 4 are slow which allows for a build up of surface holes. This increases the rate tungsten bronze donor oxidation, leading to the large difference in the H_xWO_3 LSV photoresponse is seen in Figure 3.5, black traces. The rate of tungsten bronze oxidation can be suppressed by increasing the rate of interfacial hole transfer as illustrated in Figure 3.7. In this work, we demonstrated two methods to increase the rate of interfacial hole transfer. A more rapid substrate can be used or an electrocatalyst can be applied (or both). Chloride oxidation in 0.5 M sodium chloride at pH 4 is fast and removes holes from the H_xWO_3 surface rapidly. The differences in the H_xWO_3 LSV photoresponse with chloride electrolyte (Figure 3.5, red traces) were not as severe as the H_xWO_3 potassium phosphate example (Figure 3.5, black traces). Application of an FeOOH electrocatalyst also enhanced the rate of interfacial hole transfer. The photocurrent profile of H_xWO_3|FeOOH in potassium phosphate electrolyte (Figure 3.6, purple traces) is well preserved following water oxidation compared to H_xWO_3 alone in the same electrolyte (Figure 3.5, black traces). The best preservation of photocurrent was seen with H_xWO_3|FeOOH in 0.5 M chloride electrolyte (Figure 3.6, orange traces). In this case, both chloride oxidation and the FeOOH interface provide routes for rapid interfacial hole transfer out of the H_xWO_3 material.

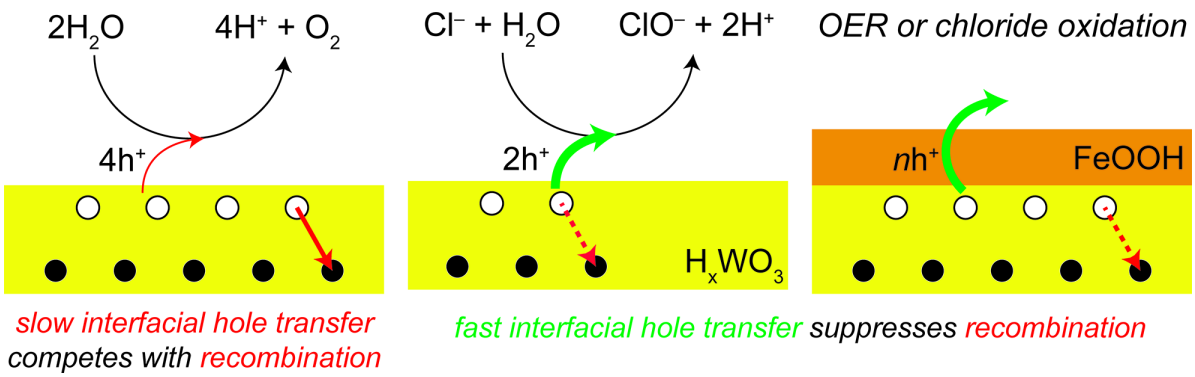

Figure 3.7: H_xWO_3 stability is affected by the rate of interfacial hole transfer.

3.4. Conlcusion

Our comparison of chloride oxidation versus water oxidation on H_xWO_3 demonstrated that while the concentration of dissolved chloride is lower than liquid water, the kinetic simplicity of chloride oxidation results in a near complete loss of FE_{OER} when the electrolyte is changed from pH 4 0.1 M KP_i ($FE_{OER} = 67 \pm 2\%$) to pH 4 0.5 M NaCl ($FE_{OER} = 2 \pm 1\%$) due to the chloride anion being a more accessible oxidation substrate. A starch-iodine test was used to confirm 100% faradaic efficiency of chloride oxidation in pH 4 0.5 M NaCl. Furthermore, H_xWO_3 exhibits much greater stability in photocurrent over three-hours of CPC at 1.23 V vs RHE when oxidizing chloride anion compared to water oxidation. The rapid kinetics of chloride oxidation eliminates holes before the oxidation of H_xWO_3 can occur, maintaining the donor density of the material. This was corroborated with sulfite oxidation, another rapid oxidation substrate, which also showed elevated photocurrent stability due to rapid electron injection from the sulfite substrate suppressing oxidation of H_xWO_3. Application of FeOOH to the surface of H_xWO_3 shows a similar phenomenon due to the scavenging of photogenerated holes in H_xWO_3 by the FeOOH electrocatalyst before oxidation of donor species can occur. By changing the substrate from water to chloride anion, a more valuable oxidation product can be formed and a significant increase in light absorber stability can be achieved.

References

[1] Claudel, F.; Dubau, L.; Berthomé, G.; Solà-Hernández, L.; Beauger, C.; Piccolo, L.; Maillard, F. Degradation Mechanisms of Oxygen Evolution Reaction Electrocatalysts: A Combined Identical-Location Transmission Electron Microscopy and X-Ray Photoelectron Spectroscopy Study. *ACS Catal.* **2019**, *9*, 4688–4698.

[2] Breuhaus-Alvarez, A.; DiMeglio, J.; Cooper, J.; Lhermitte, C.; Bartlett, B. Kinetics and Faradaic Efficiency of Oxygen Evolution on Reduced H_xWO_3 Photoelectrodes. *J. Phys. Chem. C* **2018**, *123*, 1142–1150.

[3] Lee, D.; Choi, K.-S. Enhancing long-term photostability of $BiVO_4$ photoanodes for solar water splitting by tuning electrolyte composition. *Nat. Energy* **2018**, *3*, 53–60.

[4] Barwe, S.; Weidner, J.; Cychy, S.; Morales, D.; Dieckhöfer, S.; Hiltrop, D.; Masa, J.; Muhler, M.; Schuhmann, W. Electrocatalytic 5-(hydroxymethyl)furfural oxidation using high surface area nickel boride. *Angew. Chem. Int. Ed.* **2018**, *57*, 11460–11464.

[5] Wang, S.; Zhang, N.; Tao, L.; Chen, W.; Zhou, L.; Liu, Z.; Zhou, B.; Huang, G.; Zou, Y.; Lin, H. Electrochemical Oxidation of 5-Hydroxymethylfurfural on Nickel Nitride/Carbon Nanosheets: Identified Pathway by in Situ Sum Frequency Generation Vibrational Spectroscopy. *Angew. Chem. Int. Ed.* **2019**, *58*, 15895–15903.

[6] Desilvestro, H.; Graetzel, M. Photoelectrochemistry of polycrystalline n-WO_3. Electrochemical characterization and photoassisted oxidation processes. *J. Electroanal. Chem.* **1987**, *238*, 129–150.

[7] Debiemme-Chouvy, C.; Hua, Y.; Hui, F.; Duval, J.-L.; Cachet, H. Electrochemical treatments using tin oxide anode to prevent biofouling. *Electrochim. Acta* **2011**, *56*, 10364–10370.

[8] Dionigi, F.; Reier, T.; Pawolek, Z.; Gliech, M.; Strasser, P. Design Criteria, Operating Conditions, and Nickel-Iron Hydroxide Catalyst Materials for Selective Seawater Electrolysis. *ChemSusChem* **2016**, *9*, 962–972.

[9] Lhermitte, C.; Sivula, K. Alternative Oxidation Reactions for Solar-Driven Fuel Production. *ACS Catal.* **2019**, *9*, 2007–2017.

[10] Worrell, E.; Phylipsen, D.; Einstein, D.; Martin, N. *Energy Use and Energy Intensity of the U.S. Chemical Industry*; Technical Report, 2000.

[11] Perrin, D. D. *Ionisation Constants of Inorganic Acids and Bases in Aqueous Solution*; Elsevier Science, 2013.

[12] Proctor, A. D.; Bartlett, B. M. Hydroxyl Radical Suppression During Photoelectrocatalytic Water Oxidation on WO_3|FeOOH. *J. Phys. Chem. C* **2020**, *124*, 17957–17963.

[13] Wardman, P. Reduction Potentials of One-Electron Couples Involving Free Radicals in Aqueous Solution. *J. Phys. Chem. Ref. Data* **1989**, *18*, 17957–197963.

[14] Bamwenda, G.; Sayama, K.; Arakawa, H. The effect of selected reaction parameters on the photoproduction of oxygen and hydrogen from a WO_3–Fe_2^+–Fe_3^+ aqueous suspension. *J. Photoch. Photobio. A* **1999**, *122*, 175–183.

[15] Laskowski, F. A. L.; Nellist, M. R.; Qui, J.; Boettcher, S. W. Metal Oxide/(oxy)hydroxide Overlayers as Hole Collectors and Oxygen-Evolution Catalysts on Water-Splitting Photoanodes. *J. Am. Chem. Soc.* **2019**, *141*, 1394–1405.

[16] Kim, T. W.; Choi, K.-S. Nanoporous $BiVO_4$ Photoanodes with Dual-Layer Oxygen Evolution Catalysts for Solar Water Splitting. *Science* **2014**, *343*, 990–994.

[17] Francas, L.; Corby, S.; Selim, S.; Lee, D.; Mesa, C. A.; Godin, R.; Pastor, E.; Stephens, I. E. L.; Choi, K.-S.; Durrant, J. R. Spectroelectrochemical Study of Water Oxidation on Nickel and Iron Oxyhydroxide Electrocatalysts. *Nat. Commun.* **2019**, *10*, 1–10.

[18] Lhermitte, C.; Verwer, J.; Bartlett, B. Improving the Stability and Selectivity for the Oxygen-Evolution Reaction on Semiconducting WO3 Photoelectrodes with a Solid-State FeOOH Catalyst. *J. Mater. Chem. A* **2015**, *4*.

[19] Hill, J. C.; Choi, K.-S. Effect of Electrolytes on the Selectivity and Stability of n-type WO3 Photoelectrodes for Use in Solar Water Oxidation. *J. Phys. Chem. C* **2012**, *116*, 7612–7620.

[20] Yourey, J. E.; Pyper, K. J.; Kurtz, J. B.; Bartlett, B. M. Chemical Stability of $CuWO_4$ for Photoelectrochemical Water Oxidation. *J. Phys. Chem. C* **2013**, *117*, 8708–8718.

[21] Belz, M.; Boyle, W.; Klein, K.; Grattan, K. Smart-sensor approach for a fibre-optic-based residual chlorine monitor. *Sens. Actuators B Chem.* **1997**, *39*, 380–385.

[22] Sitabkhanm, F. The Effect of Illumination on the Anodic Dissolution of Cadmium Sulphide in the Presence of a Redox System. *Ber. Bunsenges Phys. Chem.* **1972**, *76*, 389–393.

[23] Fujishima, A.; Sugiyama, E.; Honda, K. Photosensitized Electrolytic Oxidation of Iodide Ions on Cadmium Sulfide Single Crystal Electrode. *Bull. Chem. Soc. Jpn.* **1971**, *44*.

[24] Tenne, R.; Hodes, G. Photoelectrochemistry of CdSe in Sulfite Electrolyte. *Ber. Bunsenges Phys. Chem.* **1985**, *89*, 74–78.

[25] Inoue, T.; Watanabe, T.; Fujishima, A.; Honda, K. I.; Kohayakawa, K. Suppression of Surface Dissolution of CdS Photoanode by Reducing Agents. *J. Electrochem. Soc.* **1977**, *124*, 719–722.

Chapter 4.

Oxidation of Ethanol and Isopropanol using a Green Reaction Pathway via Chloride Oxidation

4.1. Introduction

The oxidation of alcohols to their corresponding aldehydes, ketones, and carboxylic acids are of high importance in the production of pharmaceuticals and fine chemicals.[1–3] Traditional alcohol oxidation reagents include the Jones reagent, Swern reagent, and the Dess-Martin periodinane.[4–6] However, while these reagents remain important tools in research and small scale synthesis, their use in industrial synthesis is impractical; The Jones reagent generates carcinogenic Cr(VI), Dess-Martin periodinane is shock sensitive, and all reagents require stoichiometric quantities.[7] New synthesis methods must adhere to green chemistry principles in order to reduce environmental impact and the cost of waste disposal. Catalytic reaction pathways greatly reduce the amount of waste produced relative to the amount of product generated. Organocatalytic examples of alcohol oxidations also exist, TEMPO (2,2,6,6-tetramethylpiperidnyloxyl) and a bromide co-catalyst can efficiently oxidize primary and secondary alcohols while using sodium hypochlorite (NaClO) as the terminal oxidant.[8] While the TEMPO based oxidation method is an enormous improvement from stoichiometric chromium oxidants, a stoichiometric amount of chloride anion is produced, preventing the reaction from being completely catalytic. Molecular oxygen has also been demonstrated as a possible terminal oxidant in alcohol oxidations by palladium and gold nanoparticles, which exhibited high selectivity and activity for the aerobic oxidation of alcohols.[9,10] While molecular oxygen seems to be an obvious choice for the terminal oxidant due to the reduced environmental impact, its use comes with added safety concerns as mixtures of oxygen and vapor from volatile organic solvents form flammable hazards.[11] Sodium hypochlorite

and hypochlorous acid constitute soluble oxidants and do not form explosive gas mixtures with organic solvents, allowing for a safer alcohol oxidation pathway while only producing a chloride waste product.

In chapter 3, we demonstrated the oxidation of chloride occurs with near unity Faradaic efficiency on H_xWO_3 during photoelectrochemical oxidations, generating hypochlorous acid. In this chapter, chloride oxidation by H_xWO_3 is performed in acidic aqueous media with a sodium chloride electrolyte, resulting in the production of hypochlorous acid (pKa = 7.4).[12]

$$Cl^-(aq) + H_2O(l) \longrightarrow ClO^-(aq) + 2\,H^+(aq) + 2\,e^- \qquad E^\circ = 1.72\ V_{SHE} \qquad (4.1)$$

Hypochlorous acid is a reactive oxidant and is a viable oxidation reagent for alcohol oxidations, resulting in a chloride mediated oxidation pathway. Ethanol and 2-propanol are used in this chapter as model substrates for primary and secondary alcohols. We measured the production of acetaldehyde and quantitative ^{1}H-NMR to determine the product yield. We used 405 nm light to illuminate H_xWO_3 metal oxide films at an irradiance of 100 $mW \cdot cm^{-2}$ in order to perform photoelectrochemical oxidation of chloride in 1 M NaCl and Na_2SO_4 electrolytes at pH 3. We also used 1 M HCl electrolyte to investigate the effect of proton activity on the oxidation of our model substrates by hypochlorous acid. The 405 nm light used to photoexcite the H_xWO_3 semiconductor was determined to play a part in the rate of ethanol oxidation but did not affect the rate of 2-propanol oxidation. We attributed this to light induced photolysis of hypochlorous acid which forms radical species.

4.2. Experimental

4.2.1. Chemicals

In all experiments, the water was filtered by a Millipore filtration system (18.2 $M\Omega \cdot cm^{-1}$). Ethanol (200 proof) was purchased from Decon Laboratories. Ammonium metatungstate $(NH_4)_6H_2W_{12}O_{40} \cdot xH_2O$ (AMT) and poly(ethylene glycol) M_w = 300 Da, PEG-300) were purchased from Sigma Aldrich. Hydrochloric Acid (37 w/w%) and sodium chloride were purchased from Fisher Scientific. Fluorine tin oxide (FTO, Pilk-

ington Glass TEC-15) substrate was cut into 1.5 × 2.54 cm^2 strips for H_xWO_3 spin coat synthesis. FTO substrate was first coarsely cleaned by scrubbing with an acetone wetted Kimwipe™. This cleaning procedure was followed by sonicating in the following solvents: acetone, Sparkleen™ detergent, water, and acetone again for 10 minutes each, with each solvent wash followed by drying under a flowing N_2 stream. Ag/AgCl reference electrodes were purchased from CH Instruments and filled with saturated KCl aqueous solution. Pt disk electrodes (2 mm diameter) were also purchased from CH Instruments./ 99.95% pure Pt wire (24 gauge, P/N 1981) was purchased from Sure Pure Chemetals.

4.2.2. Synthesis of H_xWO_3 Electrodes

H_xWO_3 electrodes were synthesized by spin coating an AMT sol. The precursor was prepared by adding 2.51 g (833 μg) AMT to a 100 mL round boton and then adding 10 mL of water to dissolve completely with vigorous stirring. Spearately, 6.6 g (22 mmol) of PEG-300 were dissolved in 10 mL of ethanol in a scintillation vial. The ethanol solution was slowly poured into the aqueous solution while stirring vigorously over the course of approximately 90 seconds, resulting in a faint, off-white sol precursor, which was 0.5 M in tungsten. Electrodes for PEC measurements were prepared by dropping 70 μL of precursor sol onto a clean, 1.5 cm square area (2.25 cm^2) of FTO which was masked off on a 1.5 × 2.54 cm^2 strip and then spun at 2500 rpm for 30 seconds using Laurell spin coater. The precursor was constantly and vigorously stirred then sealed tightly when not in use. Following spin coat deposition, the electrodes were transferred to a muffle furnace preheated to 500 °C for thirty minutes. This deposition and annealing cycle was repeated ten times total to achieve films approximately 1 μm in thickness.

4.2.3. Photoelectrochemistry

All photoelectrochemistry was performed using a CH Insturments Series 760E electrochemical workstation and a custom built light source. The light source consisted of four 405 nm LED emitters (Osram Sylvania, LZ1-10UB00-01U7) attached to a CPU heatsink and powered by a 700 mA constant current LED driver (ERP Power, ESS015W-0700-18). The 405 nm light was adjusted to an irradiance of 100 $mW \cdot cm^{-2}$ with a ther-

mopile detector (Newport 818P-015-19) and an optical power meter (Newport 1918-R). The custom made photoelectrochemical cell featured two compartments with a Nafion™ membrane separating the working electrode and counter electrode compartments. 35 mL of electrolyte was used in each compartment for all product quantification experiments and was dispensed using volumetric glassware. The Ag/AgCl reference was kept in the working electrode compartment and positioned near the H_xWO_3 working electrode. The H_xWO_3 electrode was positioned such that it was backlit by the LED emmitters through the cells quartz window. The solution electrolytes used in this work were 1 M NaCl set to pH 3 with hydrochloric acid, 1 M HCl, and 1 M Na_2SO_4 set to pH 3 with sulfuric acid.

4.2.4. Electrochemistry

2 mm diameter platinum electrodes were used in all electrochemical experiments. Chlorine gas forms due to comproportionation of hypochlorous acid and chloride, generating gas bubbles which can cover the platinum electrode and interfere with the electrolysis. In an effort to control this, the solution volume was reduced from 35 mL to 15 mL for the platinum electrode experiments and 6 mA of anodic current was passed galvanostatically for three hours through the platinum working electrode. The total amount of charge passed was 64.8 C for all galvanostatic experiments. The potential required to maintain 6 mA of current through the platinum working electrode was recorded versus a Ag/AgCl reference electrode. Reducing the electrolyte volume allowed for a lower operating current while maintaining a similar amount of charge passed per solution volume in three hours when compared to the H_xWO_3 electrode experiments. A Nafion™ membrane was used to separate the working electrode compartment from the counter electrode compartment. A stir bar was used to vigorously stir the working compartment solution and the platinum electrode was kept as close as possible to the spinning stir bar to remove gas bubbles from the platinum electrode surface. When the effect of 405 nm light on ethanol and 2-propanol oxidation was being investigated, the platinum electrode was positioned such that the irradiance was 100 $mW \cdot cm^{-2}$ at the platinum electrodes location.

4.2.5. Quantification of Products

Quantfication of products was done using quantitative single pulse ^{1}H-NMR performed on a 700 MHz Varian NMR using a relaxation delay of 25 seconds and a pulse angle of 90°. A typical NMR sample was composed of 200 μL of 100 mM sodium formate dissolved in D_2O as an internal standard and 300 μL of electrolyte from the working compartment. However, in the case of 1 M HCl electrolyte used with ethanol substrate, the NMR sample was augmented to 100 μL of working compartment electrolyte, 300 μL of 100 mM sodium formate in D_2O internal standard and 100 μL of 1 M NaOH. The NaOH was required to neutralize the solution, as the acetaldehyde product undergoes acid catalyzed polymerization which interferes with quantification.[13]

4.3. Results and Discussion

4.3.1. Oxidation of Ethanol and 2-Propanol

To begin investigating the effectiveness of chloride as a mediator for alcohol oxidation, constant potential coulometry (CPC) experiments were performed at 1 V vs Ag/AgCl under 405 nm light at an intensity of 100 $\mathrm{mW \cdot cm^{-2}}$. The yield of each product species was calculated according to the equation

$$\text{percent yield} = \frac{n \cdot (\text{moles of product})}{F^{-1} \cdot (\text{charge passed})} \cdot 100 \tag{4.2}$$

Where F is Faradays constant ($96485 \frac{\mathrm{C}}{\text{mole } e^-}$) and n is the number of electrons transferred to form the product. The oxidation of ethanol to acetaldehyde is a two-electron oxidation while the oxidation of ethanol to acetic acid is a four-electron oxidation.

$$\mathrm{CH_3CH_2OH} \longrightarrow \mathrm{CH_3COH} + 2\,\mathrm{H^+} + 2\,\mathrm{e^-} \qquad n = 2 \tag{4.3}$$

$$\mathrm{CH_3CH_2OH} + \xrightarrow{\mathrm{O^-}} \mathrm{CH_3COOH} + 2\,\mathrm{H^+} + 4\,\mathrm{e^-} \qquad n = 4 \tag{4.4}$$

The oxidation of 2-propanol to acetone is a 2-electron oxidation.

$$\mathrm{CH_3CHOHCH_3} \longrightarrow \mathrm{CH_3COCH_3} + 2\,\mathrm{H^+} + 2\,\mathrm{e^-} \qquad n = 2 \tag{4.5}$$

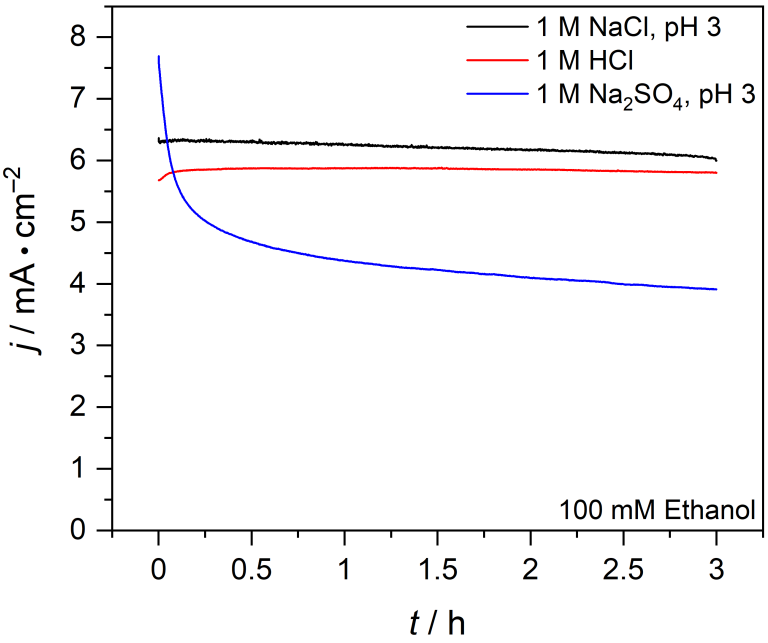

Figure 4.1: Oxidation of 100 mM ethanol during a 3-hour constant potential coulometry experiments of H_xWO_3 in 1 M NaCl, pH 3 (black); 1 M HCl (red); and 1 M Na_2SO_4, pH 3 (blue). A potential of 1 V vs Ag/Cl was applied to the H_xWO_3 film while under 100 mW·cm^{-2}.

The product yields (mean and standard deviation) during ethanol oxidation are shown in Table 4.1 while the product yields during 2-propanol oxidation are shown in Table 4.2. The results in both tables show that product yields during both ethanol and 2-propanol oxidation are significantly higher in Cl^- based electrolytes when compared to $SO_4{}^{2-}$ electrolyte. When comparing between 1 M NaCl, pH 3 and 1 M HCl electrolytes, there is no significant difference in the charge passed; t(3) = 0.84, p = .46, and the acetaldehyde yield shows no significant difference either; t(4) = 1.01, p = .37. However, 1 M HCl electrolyte results in a significant decrease in the yield of acetic acid; t(4) = -9.0, p = .0001, due to high proton activity suppressing the rate of acetic acid formation. Proton

Table 4.1: Oxidation of 100 mM ethanol by H_xWO_3 in 1 M NaCl, Na_2SO_4, and HCl electrolytes

3 Trials	Charge Passed/C	Acetaldehyde Yield/%	Acetic Acid Yield/%
1 M NaCl, pH 3	150 ± 14	50 ± 3	39 ± 2
1 M HCl	146 ± 7	48 ± 3	27 ± 2
1 M Na_2SO_4, pH 3	108 ± 8	16 ± 2	7 ± 4

Table 4.2: Oxidation of 100 mM 2-propanol by H_xWO_3 in 1 M NaCl, Na_2SO_4, and HCl electrolytes

3 Trials	Charge Passed/C	Acetone Yield/%
1 M NaCl, pH 3	226 ± 9	92 ± 4
1 M HCl	210 ± 5	72 ± 5
1 M Na_2SO_4, pH 3	120 ± 3	16 ± 2

activity does not significantly impact the rate determining step of ethanol to aldehyde oxidation but the rate determining step in the oxidation of ethanol to acetic acid is significantly hindered by proton activity. The photocurrent response of H_xWO_3 during ethanol oxidation is shown in Figure 4.1. When the electrolyte used in ethanol oxidation is 1 M Na_2SO_4, the photocurrent response of H_xWO_3 shows an initially steep decline in photocurrent which begins to taper off after decreasing by nearly 50%. This is the same phenomenon described in chapter 2, where water oxidation conditions were shown to be sufficient to remove donor species in the H_xWO_3 material (reversal of Equation

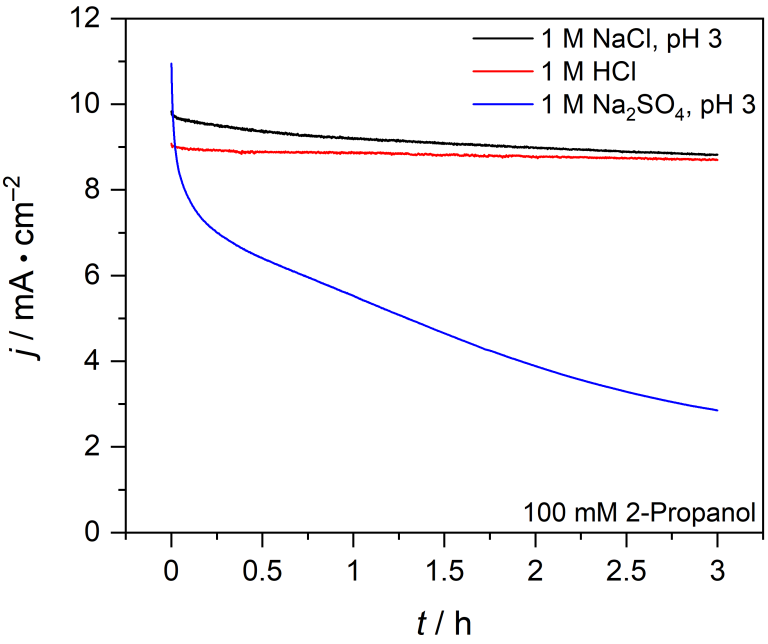

Figure 4.2: Oxidation of 100 mM 2-propanol during 3-hour potential coulometry experiments of H_xWO_3 in 1 M NaCl, pH 3 (black); 1 M HCl (red); and 1 M Na_2SO_4, pH 3 (blue). All experimental parameters were identical to those used in Figure 4.1 but were performed with 2-propanol as the substrate.

2.1). The tungsten bronze impurities serve as donors, increasing the donor density in the material.[14,15] As the donor species is oxidized, the photoactivity of the H_xWO_3 electrode decreases.[14] In chapter 3, we demonstrated that chloride oxidation prevents the oxidation of W^{+5} donor species by rapid electron injection into surface holes, eliminating them before they can perform any deleterious reactions. Water oxidation proceeds through a high energy hydroxyl species, hindering the reaction and causing a buildup of surface holes in H_xWO_3.[16] In sulfate electrolyte the faradaic efficiency of the oxygen evolution reaction is about 70%, placing the upper limit of the faradaic efficiency of sulfate anion oxidation at approximately 30%.[14] The rate of sulfate anion oxidation is then even more hin-dered than water oxidation. Here we demonstrate a yield of 16% for the oxidation of ethanol in 1 M sulfate electrolyte, indicating a slow rate of ethanol oxidation, regardless if it occurs by direct oxidation on the H_xWO_3 surface or by peroxydisulfate formed during sulfate oxidation, the overall rate of ethanol oxidation is low.[17] In 1 M sodium chloride and hydrochloric acid electrolytes however, we observed high stability throughout the three-hour CPC experiment and also high product yields. Chloride oxidation rapidly injects electrons into valence band holes, resulting in rapid oxidation and suppresses deleterious donor species oxidation (reversal of Equation 2.1) The yield of acetaldehyde and acetic acid showed a large increase in yield with chloride electrolyte, highlighting the participation of the Cl^- anion in the oxidation mechanism. No chlorinated species were observed by ^{1}H-NMR.

The oxidation of 2-propanol was also investigated in chloride and suflate electrolytes and the acetone yield mean and standard deviation are shown in Table 4.2. The photocurrent response of H_xWO_3 during the CPC experiment is shown in Figure 4.2 and demonstrates elevated stability in chloride electrolytes when compared to the sulfite electrolyte. As in the case of 100 mM ethanol, the addition of 100 mM 2-propanol does not hinder chloride oxidation. We do note that more charge was passed when 100 mM 2-propanol was the substrate compared to 100 mM ethanol substrate. However, Figure C.3 in the appendix shows linear sweep voltammograms of H_xWO_3 in 1 M NaCl, pH 3 with and without substrate and demonstrates that the presence of ethanol or 2-propanol does not affect the chloride oxidation chemistry occuring on the metal oxide surface. The linear sweep voltammograms in Figure C.3 were performed in a cell with no Nafion™ membrane inserted between the working electrode compartment

and counter electrode compartment. The difference in photoactivity is then due to the interaction of the Nafion™ and the dissolved alcohol which results in interference with the photoelectrochemistry. The yield of 2-propanol oxidation to acetone in 1 M NaCl, pH 3 is 92 ± 4 %, which is not significantly different from the sum of acetaldehyde and acetic acid yields for the same electrolyte in Table 4.1 (89 ± 4 %); t(4) = 1.26, p = .26, and suggests that the net product yield is not strongly dependent on the identity of the alcohol. The formation of acetone is affected by the proton activity, showing a significant decrease in acetone product yield when using a 1 M HCl electrolyte; t(4) = -5.89, p = .002. The oxidation of 2-propanol to acetone then exhibits a dependence on proton activity, similar to production of acetic acid from ethanol.

4.3.2. Characterization of Free Chlorine Species Produced by H_xWO_3 in Chloride Electrolytes

Our oxidation of ethanol and 2-propanol demonstrated the highest conversion of alcohol to product in the presence of chloride, highlighting the importance of the anion in the overall oxidation of ethanol and 2-propanol. In chapter 3, we demonstrated that the oxidation of chloride on H_xWO_3 electrodes forms hypochlorous acid occurs with near unity faradaic efficiency, suggesting that HClO is responsible for performing the oxidation of ethanol and 2-propanol we see here. The generation of HClO by H_xWO_3 in 1 M NaCl, pH 3 and 1 M HCl is demonstrated in Figure 4.3. Shown are the UV-Vis spectra of pH 3, 1 M NaCl and 1 M HCl, the two chloride electrolytes used in this work, after 1 V vs Ag/AgCl CPC for one hour under 405 nm light at an irradiance of 100 $mW \cdot cm^{-2}$. No substrate was added. Also shown in Figure 4.3 is the UV-Vis spectra of 0.2 mM $Ca(ClO)_2$ dissolved in both electrolytes. All examples show a λ_{max} of 233 nm, assigned to the UV absorption by HClO, with no evidence of Cl_2 (λ_{max} = 229 nm) or ClO^- (λ_{max} = 290 nm) UV absorption occurring.[18] The UV-Vis traces shown in Figure 4.3 were taken either immediately after the CPC finished or immediately after making the $Ca(ClO)_2$ solution. But when a solution of pH 3, 1 M NaCl, 20 mM $Ca(ClO)_2$ is allowed to equilibrate for forty-five minutes, the UV absorption broadens significantly and a shift in λ_{max} towards lower wavelengths occurs (Figure C.1). This indicates that the comproportionation of HClO and Cl^- ($HClO\,(aq) + Cl^-(aq) + H^+(aq) \longrightarrow Cl_2(aq) +$

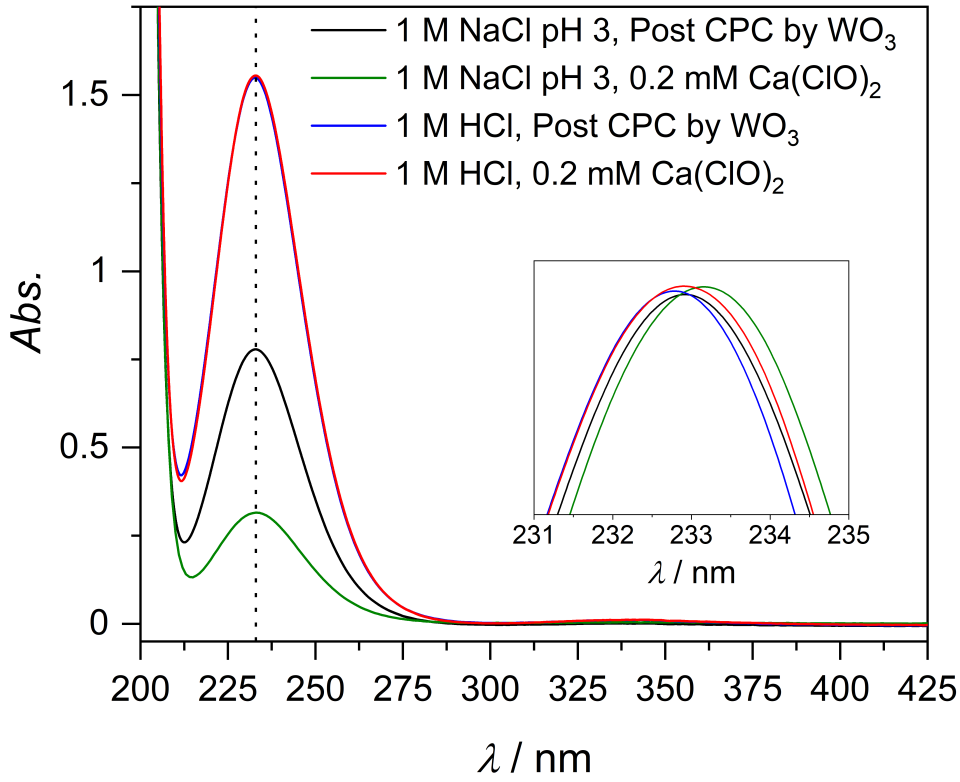

Figure 4.3: UV-Vis spectra of chloride containing electrolytes after being used in a substrate free CPC experiment with H_xWO_3. These are compared against the same electrolyte with 0.2 mM $Ca(ClO)_2$. The vertical dotted line denotes λ_{max} = 233 nm and is assigned to the absorption by HClO. The inset displays the normalized absorption feature at 233 nm for the four spectra.

$H_2O(l)$) is fairly slow. In Figure 4.3, the UV absorption feature at 229 nm of Cl_2 is absent after CPC electrolysis of the electrolyte by H_xWO_3 and we conclude that oxidation of Cl^- by H_xWO_3 produces HClO without significant Cl_2 production, even in 1 M HCl electrolyte. However, Cl_2 does form by comproportionation and may contribute to the oxidation of ethanol and 2-propanol.

4.3.3. The Effect of Light on the Rate of Oxidation

To determine if the energy input from the 405 nm light source contributes to the oxidation of ethanol, control experiments were performed with a platinum disk to compare the change in product distribution when the working compartment was under 405 nm,

100 mW·cm^{-2} irradiation and in the dark. The platinum electrolysis of 100 mM ethanol and 100 mM 2-propanol was performed galvanostatically at 6 mA anodic current for 3 hours and the product yields are displayed in Table 4.3. The product yields tabulated for platinum oxidation of ethanol and 2-propanol are from three separate trials for each light and substrate combination in 1 M NaCl at pH 3. A constant current of 6 mA and 15 mL of electrolyte in the working compartment was chosen because this would pass 4.5 C per volume of electrolyte over the three-hour experiment, similar to the amount of charge passed per volume of electrolyte during the H_xWO_3 CPC experiments tabulated in Tables 4.1 and 4.2. The results show that the 405 nm light being used to photoexcite the H_xWO_3 electrode also assists in the oxidation of ethanol but not 2-propanol. We assign the difference in yield to the photon energy rather than any thermal energy from the LED emitters because the solution temperature rises by only 3 °C over three hours during the irradiated experiments. While yield of acetaldehyde doubles due to the inclusion of 405 nm light during oxidation of ethanol, the change in acetic acid yield is statistically insignificant; $t(4) = .95$, $p = .4$, indicating that phenomenon responsible for the enhancement in acetaldehyde production does not strongly affect the production of acetic acid. The difference in the yield of acetone from 2-propanol oxidation that results from 405 nm irradiation of the electrolyte solution shows a similarly insignificant difference; $t(4) = .22$, $p = .83$. While the percent yield for oxidation of ethanol and 2-propanol on H_xWO_3 and platinum in chloride electrolytes were not exactly the same, this is likely because the production of hypochlorous acid on platinum is not faradaic as it is on H_xWO_3. This does not affect our conclusions, as we are interested in the change in yield and the oxidation of chloride by H_xWO_3 and platinum is not expected to be affected by 405 nm irradiation. The irradiation of HOCl and ClO^- by light creates $Cl^\bullet$

Table 4.3: Alcohol oxidation by a platinum electrode with and without irradiation by 405 nm light in 1 M NaCl, pH 3

3 Trials	No $h\nu$	$h\nu$
100 mM ethanol		
Acetaldehyde Yield / %	25 ± 5	56 ± 2
Acetic Acid Yield / %	21 ± 6	25 ± 2
100 mM 2-propanol		
Acetone Yield / %	74 ± 5	73 ± 5

and $OH^{\bullet}$, both strong oxidants, through homolytic cleavage of the Cl–O bond.[19,20]

$$HOCl + h\nu \longrightarrow OH^{\bullet} + Cl^{\bullet} \tag{4.6}$$

$$OCl^{-} + h\nu \longrightarrow O^{\bullet -} + Cl^{\bullet} \tag{4.7}$$

$$O^{\bullet -} + H_2O \longrightarrow OH^{\bullet} + OH^{-} \tag{4.8}$$

Any generated $OH^{\bullet}$ and $Cl^{\bullet}$ radical species are expected to be extremely reactive and a number of possible subsequent reactions have been identified during free chlorine photolysis.[20] The reactions which may occur between radical species and liquid water, aqueous chloride, or hypochlorous acid are generally extremely rapid with rate constants on the order of 10^9 $M^{-1}s^{-1}$.[20]

$$OH^{\bullet} + HOCl \longrightarrow ClO^{\bullet} + H_2O \qquad k = 8.5 \cdot 10^4 - 2.0 \cdot 10^9 \text{ } M^{-1}s^{-1} \tag{4.9}$$

$$OH^{\bullet} + Cl^{-} \longrightarrow HOCl^{-\bullet} \qquad k = 4.3 \cdot 10^9 \text{ } M^{-1}s^{-1} \tag{4.10}$$

$$HOCl^{-\bullet} \longrightarrow OH^{\bullet} + Cl^{-} \qquad k = 6.1 \cdot 10^9 \text{ } s^{-1} \tag{4.11}$$

$$Cl^{\bullet} + HOCl \longrightarrow ClO^{\bullet} + H^{+} + Cl^{-} \qquad k = 3 \cdot 10^9 \text{ } M^{-1}s^{-1} \tag{4.12}$$

$$Cl^{\bullet} + Cl^{-} \longrightarrow {Cl_2}^{-\bullet} \qquad k = 6.5 \cdot 10^9 - 2.1 \cdot 10^{10} \text{ } M^{-1}s^{-1} \tag{4.13}$$

$${Cl_2}^{-\bullet} \longrightarrow Cl^{\bullet} + Cl^{-} \qquad k = 6.0 \cdot 10^4 - 1.1 \cdot 10^5 \text{ } s^{-1} \tag{4.14}$$

$${Cl_2}^{-\bullet} + H_2O \longrightarrow Cl^{-} + HOCl^{-\bullet} + H^{+} \qquad k = 2.4 \cdot 10^1 \text{ } M^{-1}s^{-1} \tag{4.15}$$

Because the radical species may form a variety of oxidizing agents, it is difficult to accurately determine the exact reactive species or group of reactive species responsible for the alcohol oxidation yields observed. In our 1 M chloride electrolytes, we would expect the equilibrium $OH^{\bullet} + Cl^{-} \rightleftharpoons HOCl^{-\bullet}$ because the forward rate of reaction (Eqn. 4.10) and reverse rate of reaction (Eqn. 4.11) are at the same order of magnitude. Any chloride radical generated is likely scavenged in 1 M chloride electrolytes by the reaction $Cl^{-\bullet} + Cl^{-} \rightleftharpoons {Cl_2}^{-\bullet}$, because the rate of the forward reaction (Eqn. 4.13) is 4 to 6 orders of magnitude greater than the rate of the reverse reaction (Eqn. 4.14).[20] While the major absorption maxima of aqueous free chlorine species (Cl_2, HClO, ClO^{-}) exist at $\lambda < 300$ nm, enhancement in free chlorine oxidation rates by longer wavelength light has been demonstrated before.[19–23] Under 365 nm irradiation, production of $OH^{\bullet}$ and $Cl^{\bullet}$ increases with decreasing pH due to the higher quantum yield of HOCl cleavage

(Equation 4.6) compared to ClO^- cleavage (Equation 4.7).[19] The UV-Vis spectrum of a 20 mM solution of $Ca(ClO)_2$ is shown in Figure C.2 for both electrolytes used. The 405 nm light output by the LED emitters overlaps with the foot of the HClO absorption feature at $\lambda_{max} \approx 325$ nm in both electrolytes and helps to explain the increased product yield observed when the solution is under 405 nm light irradiation. It is important to note that our LED emitters output light centered about 405 nm at a power density of 100 $mW \cdot cm^{-2}$, whereas AM 1.5 G light (terrestrial solar simulation) produces ≤ 405 nm light at a power density of 5.2 $mW \cdot cm^{-2}$. While the full-width half-max of the spectral distribution emitted by LED units used are not given by the manufacturer, the value is generally about $10 - 30$ nm for off-the-shelf units which increases the fraction of light that could be absorbed by the HClO absorption feature shown in Figure C.2.

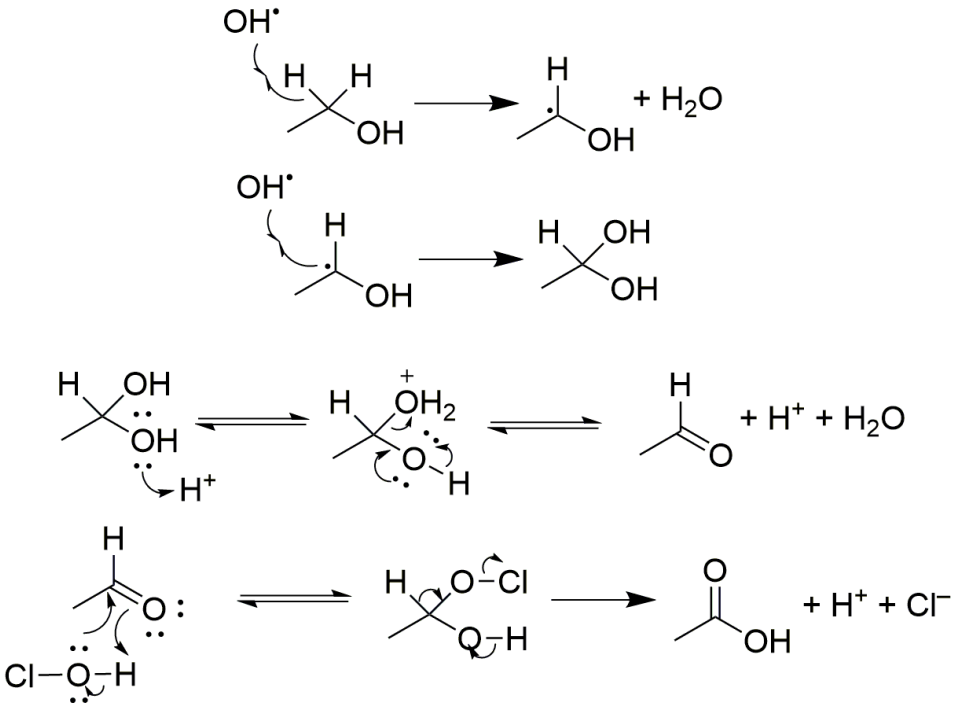

Figure 4.4: The oxidation of ethanol to acetaldehyde followed by the subsequent oxidation to acetic acid.

From the yields of ethanol oxidation on H_xWO_3, we see that only the formation of acetic acid is affected by changes in proton activity while acetaldehyde yield was in-

dependent of proton activity. Also, the oxidation of ethanol by platinum in chloride electrolytes demonstrated that irradiation only affected the production of acetaldehyde and had no effect on the yield of acetic acid. Increases in yield caused by illumination of hypo-chlorous acid have been used to identify rate limiting steps in which radicals may participate.[24] During the formation of acetaldehyde, the initial oxidation step is likely rate limiting, with the second oxidation and loss of water occurring rapidly. The initial oxidation can be performed by radical species which caused the increase in acetaldehyde yield observed in Table 4.3 when the working compartment was irradiated by 405 nm light during ethanol oxidation with platinum electrodes. A decrease in acetic acid yield was observed in Table 4.1 due to an increase in proton activity. The rate limiting step in the oxidation of acetaldehyde to acetic acid is likely the oxidation step illustrated in Figure 4.4, which results in the loss of a proton and chloride anion. The rate of this step would be expected to be hindered by protons but not accelerated by a higher concentration of radical species.

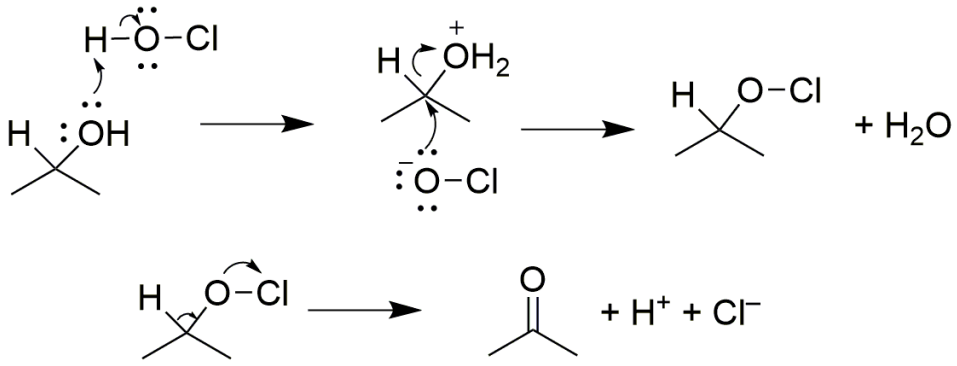

Figure 4.5: The oxidation of 2-propanol to acetone

The oxidation of 2-propanol to acetone follows similar behavior as the formation of acetic acid from ethanol. An increase in proton activity suppresses the yield of acetone while no effect is observed when oxidation of 2-propanol is performed using platinum electrodes in the dark and under 405 nm irradiation. In Figure 4.5, no radical species is required in the mechanism and the rate limiting step is likely the oxidation step, which generates protons and thereby causing a dependence on the proton activity.

4.4. Conclusions

We have demonstrated the photocatalyzed production of hypochlorous acid and the utility it presents in performing useful oxidative transformations. The enhancement in H_xWO_3 stability investigated in Chapter 3 provided the motivation to investigate the reactivity of the chloride oxidation products. In contrast to the OER investigated in Chapter 2, chloride oxidation products on H_xWO_3 are highly soluble in water, allowing for the opportunity to investigate further reactions. Hypochlorous acid was demonstrated to constitute the main product of H_xWO_3 oxidation of chloride by UV-Vis analysis of the working compartment solution. Hypochlorous acid was the main product even in 1 M HCl, though comproportionation was shown to produce Cl_2 gas in a subsequent reaction. Ethanol and 2-propanol served simple model substrates for primary and secondary alcohols and the product yields were monitored by ^{1}H-NMR. For both substrates, high conversion was obtained and no chlorinated products were observed for our substrates. The 405 nm light used to photoexcite the H_xWO_3 light absorbers was shown to influence the rate of acet-aldehyde formation but did not affect the rate of acetic acid formation or the formation of acetone during 2-propanol oxidation. High intensity irradiation increases the concentration of radicals by homolytic cleavage of hypochlorous acid. Because the rate determining step in the formation of acetaldehyde may be performed by radical oxidants, irradiation increases the yield. The mechanism of acetic acid and acetone formation both require the addition of hypochlorite. Radicals do not take part in this mechanism and no change in acetic acid or acetone yield is observed between dark and 405 nm irradiation of the working compartment electrolyte during oxidation with platinum electrodes.

Chloride oxidation and water oxidation both represent green solar fuel substrate. This chapters work demonstrated the utility of the hypochlorous product in performing oxidations of non-benzyllic organic substrate. The gaseous O_2 product from water oxidation presents challenges due to the low solubility of O2 in water and the hazards from mixtures O2, hydrogen, and any potential hydrocarbons. The high solubility of hypochlorous acid allows for safe use of the strong oxidant in organic oxidations.

References

[1] Ley, S.; Norman, J.; Griffith, W.; Marsden, S. Tetrapropylammonium Perruthenate, $Pr_4N^+RuO_4^-$, TPAP: A Catalytic Oxidant for Organic Synthesis. *Synthesis-stuttgart* **1994**, 639–666.

[2] Arends, I.; Sheldon, R. *Modern Oxidation Methods*; John Wiley & Sons, Ltd, 2005; Chapter 4, pp 83 – 118.

[3] Hudlicky, M. *Oxidations in Organic Chemistry*; American Chemical Society: Washington DC, 1990.

[4] Bowden, K.; Heilbron, I. M.; Jones, E. R. H.; Weedon, B. C. L. Researches on Acetylenic Compounds. Part I. The Preparation of Acetylenic Ketones by Oxidation of Acetylenic Carbinols and Glycols. *J. Chem. Soc.* **1946**, 39–45.

[5] Mancuso, A.; Huang, S.-L.; Swern, D. Oxidation of long-chain and related alcohols to carbonyls by dimethyl sulfoxide "activated" by oxalyl chloride. *J. Org. Chem.* **1978**, *43*, 2480–2482.

[6] Dess, D. B.; Martin, J. C. Readily accessible 12-I-5 oxidant for the conversion of primary and secondary alcohols to aldehydes and ketones. *J. Org. Chem.* **1983**, *48*, 4155–4156.

[7] Sheldon, R. Fundamentals of Green Chemistry: Efficiency in Reaction Design. *Chem. Soc. Rev.* **2012**, *41*, 1437–51.

[8] Anelli, P.; Biffi, C.; Montanari, F.; Quici, S. Fast and selective oxidation of primary alcohols to aldehydes or to carboxylic acids and of secondary alcohols to ketones mediated by oxoammonium salts under two-phase conditions. *J. Org. Chem.* **1987**, *52*, 2559–2562.

[9] Mori, K.; Hara, T.; Mizugaki, T.; Ebitani, K.; Kaneda, K. Hydroxyapatite-Supported Palladium Nanoclusters: A Highly Active Heterogeneous Catalyst for Selective Oxidation of Alcohols by Use of Molecular Oxygen. *J. Am. Chem. Soc.* **2004**, *126*, 10657–10666.

[10] Christensen, C. H.; Jørgensen, B.; Rass-Hansen, J.; Egeblad, K.; Madsen, R.; Klitgaard, S. K.; Hansen, S. M.; Hansen, M. R.; Andersen, H. C.; Riisager, A. Formation of Acetic Acid by Aqueous-Phase Oxidation of Ethanol with Air in the Presence of a Heterogeneous Gold Catalyst. *Angew. Chem., Int. Ed.* **2006**, *45*, 4648–4651.

[11] Alfonsi, K.; Colberg, J.; Dunn, P.; Fevig, T.; Jennings, S.; Johnson, T.; Kleine, H.; Knight, C.; Nagy, M.; Perry, D.; Stefaniak, M. Green chemistry tools to influence a medicinal chemistry and research chemistry based organisation. *Green Chem.* **2008**, *10*, 31–36.

[12] Perrin, D. D. *Ionisation Constants of Inorganic Acids and Bases in Aqueous Solution*; Elsevier Science, 2013.

[13] Scheithauer, A.; Brächer, A.; Grützner, T.; Zollinger, D.; Thiel, W.; Von Harbou, E.; Hasse, H. Online ^{1}H NMR Spectroscopic Study of the Reaction Kinetics in Mixtures of Acetaldehyde and Water Using a New Microreactor Probe Head. *Ind. Eng. Chem. Res.* **2014**, *53*, 17589–17596.

[14] Breuhaus-Alvarez, A.; DiMeglio, J.; Cooper, J.; Lhermitte, C.; Bartlett, B. Kinetics and Faradaic Efficiency of Oxygen Evolution on Reduced H_xWO_3 Photoelectrodes. *J. Phys. Chem. C* **2018**, *123*.

[15] Bullett, D. W. Bulk and surface electron states in WO_3 and tungsten bronzes. *J. Phys. C: Solid State Phys.* **1983**, *16*, 2197–2207.

[16] Proctor, A. D.; Bartlett, B. M. Hydroxyl Radical Suppression During Photoelectrocatalytic Water Oxidation on WO_3|FeOOH. *J. Phys. Chem. C* **2020**, *124*, 17957–17963.

[17] Mi, Q.; Coridan, R. H.; Brunschwig, B. S.; Gray, H. B.; Lewis, N. S. Photoelectrochemical Oxidation of Anions by WO_3 in Aqueous and Non-Aqueous Electrolytes. *Energy Environ. Sci.* **2013**, *6*.

[18] Belz, M.; Boyle, W.; Klein, K.; Grattan, K. Smart-sensor approach for a fibre-optic-based residual chlorine monitor. *Sens. Actuators B Chem.* **1997**, *39*, 380–385.

[19] Bulman, D.; Mezyk, S.; Remucal, C. The Impact of pH and Irradiation Wavelength on the Production of Reactive Oxidants during Chlorine Photolysis. *Environ. Sci. Technol.* **2019**, *53*, 4450 – 4459.

[20] Remucal, C.; Manley, D. Emerging investigators series: The efficacy of chlorine photolysis as an advanced oxidation process for drinking water treatment. *Environ. Sci.: Water Res. Technol.* **2016**, *2*, 565 – 579.

[21] Izadifard, M.; Langford, C.; Achari, G. Alternative View of Chlorine Oxidation Stimulated by Longer Wavelength Light. *J. Environ. Chem. Eng.* **2016**, *142*, 04016048–1 – 04016048–4.

[22] Forsyth, J.; Zhou, P.; Mao, Q.; Asato, S.; Meschke, J.; Dodd, M. Enhanced Inactivation of Bacillus subtilis Spores during Solar Photolysis of Free Available Chlorine. *Environ. Sci. Technol.* **2013**, *47*, 12976 – 12984.

[23] Shu, Z.; Li, C.; Belosevic, M.; Bolton, J.; El-Din, M. Application of a Solar UV/Chlorine Advanced Oxidation Process to Oil Sands Process-Affected Water Remediation. *Environ. Sci. Technol.* **2014**, *48*, 9692 – 9701.

[24] Horton, J. A.; Laura, M. A.; Kalbag, S. M.; Petterson, R. C. Reaction of Hypochlorous Acid with Ketones. Novel Baeyer-Villiger Oxidation of Cyclobutanone with Hypochlorous Acid. *J. Org. Chem.* **1969**, *34*.

Chapter 5.

Conclusions and Outlook

5.1. Summary of Presented Work

The focus of the work in this thesis has been to ascertain how the thermodynamics and kinetics of two important solar fuel forming reactions interplay on H_xWO_3 surfaces. H_xWO_3 was used for the entirety of the work as this allowed for a consistent surface with which to perform our experiments. While the two electron oxidation of chloride (1.36 V vs NHE) is thermodynamically more challenging than water oxidation (1.23 V vs NHE), water oxidation proceeds through high-energy intermediates. The result is that during water oxidation, electrochemically active donor species from H_xWO_3, become oxidized and the overall donor density decreases as protons deintercalate.

$$H_xWO_3 \longrightarrow WO_3 + xH^+ + xe^- \tag{5.1}$$

As the donor density continuously drops during the OER, the overall photocurrent density drops as well. By introducing a rapid oxidation substrate, a build-up of surface holes can be prevented from occurring, reducing the rate of deleterious oxidation reactions. Chloride can serve as a rapid oxidation, substrate and the stability is enhanced in chloride electrolytes that have similar concentration to seawater. The product of chloride oxidation is hypochlorous acid, a reactive oxidant in its own right.

In Chapter 2, we used sulfate electrolyte to demonstrate a faradaic efficiency of $70 \pm 10\%$ duing the OER alongside a concurrent loss of photocurrent density. This loss of photocurrent density was shown to be highly reversible and the recovery was induced by light irradiation. H_xWO_3 may auto-oxidize during the OER ($H_xWO_3 \longrightarrow WO_3 + xH^+ + xe^-$). When H_xWO_3 absorbs light in electrolyte under zero applied potential

bias, the loss of donor species may be reversed by photogenerated electron-hole pairs. Holes in the valence band can perform water oxidation without any additional potential input. Conduction band electrons can reduce W^{+6} in the tungsten oxide material. This leads to the overall reformation of H_xWO_3 ($xH^+ + xe^- + WO_3 \xrightarrow{h\nu} H_xWO_3$). By flow cell GC analysis, the OER activity increases alongside the overall photocurrent density.

In Chapter 3, the mechanism of photocurrent degradation was investigated more in depth by performing chloride oxidation and using an FeOOH electrocatalyst to perform water oxidation. Chloride oxidation served as a rapid oxidation substrate, promoting photocurrent stability by rapidly eliminating holes in the material. A similar phenomenon was seen after applying FeOOH onto the surface of H_xWO_3. The electrocatalyst FeOOH rapidly removes holes from the surface of H_xWO_3 in a similar fashion to chloride oxidation. The positioning of FeOOH bands on WO_3 promotes rapid charge transfer between the H_xWO_3 and FeOOH which allows for rapid removal of surface holes. When oxidizing sulfite, we again saw stabilization in the photocurrent. The combined thermodynamic and kinetic ease of sulfite oxidation resulted in a slight reduction of the H_xWO_3 material.

In Chapter 4, the results from Chapters 2 and 3 were used to direct an investigation into primary and secondary alcohol oxidation via chloride oxidation. Chloride oxidation on H_xWO_3 results in hypochlorous acid exclusively, even in 1 M HCl electrolyte. Chloride oxidation was performed in aqueous solutions containing ethanol and 2-propanol to react the produced hypochlorous acid with alcohol substrates. The reactivity of hypochlorous is extremely high, and the product yields are very high as a result. Light was shown to play a part in acetaldehyde formation only. Using platinum electrodes, we were able to investigate the effect of irradiation on the electrolyte during chloride oxidation. Irradiation did not affect conversion of ethanol to acetic acid nor did it affect the conversion of 2-propanol to acetone.

5.2. Forceful Incorporation of Cationic Species in WO_3

The result from Chapter 2 indicate that the electrochromic properties of WO_3 is important to the photocatalytic abilities of WO_3. Tungsten oxide bronzes can be formed from

a variety of group I elements by electrochemical intercalation of the cation into WO_3.

$$WO_3 + M^+ + e^- \longrightarrow MWO_3 \qquad M = \text{Group I Cation} \tag{5.2}$$

This suggests that the donor density of WO_3 light absorbers can be raised or lowered by electrochemical intercalation or deintercalation. Proton bronze (HWO_3) impurities were shown to increase the OER photocurrent but it is uncertain if this is general to all tungsten bronze materials. Two methods were attempted in introducing cationic dopants. The first was to add the nitrate salt of a group I cation to synthesis solution. The second was to use the same H_xWO_3 film used in Chapters 2 through 4 and forcibly intercalate cations electrochemicaly.

5.2.1. Tungsten Bronze by Chemical Synthesis

In the inital attempts at augmenting WO_3, oxygen annealing was performed to remove the proton bronze impurities in H_xWO_3 so that a better comparison could be made between M_xWO_3 and WO_3. Using the synthesis described in Chapters 2 through 4, WO_3 films were made except flowing 100% O_2 was passed over the films during the annealing step. The purpose of the flowing O_2 was to chemically remove proton bronze impurities and obtain WO_3.

$$4\,HWO_3 + O_2 \xrightarrow{\Delta} 4\,WO_3 + 2\,H_2O \tag{5.3}$$

It must be noted that this treatments likely also removes oxygen vacancies which also contribute to the donor density. This is acceptable because the change in observable photoelectrochemical metrics such as photocurrent density, photocurrent stability, and onset potential due to electrochromic effects should not be dependent on the extent of oxygen vacancies. In Figure 5.1, an oxygen annealed tungsten oxide film (O_2-WO_3) was used to observe the change in photocurrent density after photo-driven formation of proton bronze. The O_2-WO_3 film was irradiated by AM 1.5 G solar simulated light in a solution of water set to pH 1 with sulfuric acid. For the first four hours, the O_2-WO_3 film was poised at 0.98 V vs Ag/AgCl and the CPC photocurrent density was recorded in the black trace of Figure 5.1. The photocurrent density shows an initially steep drop

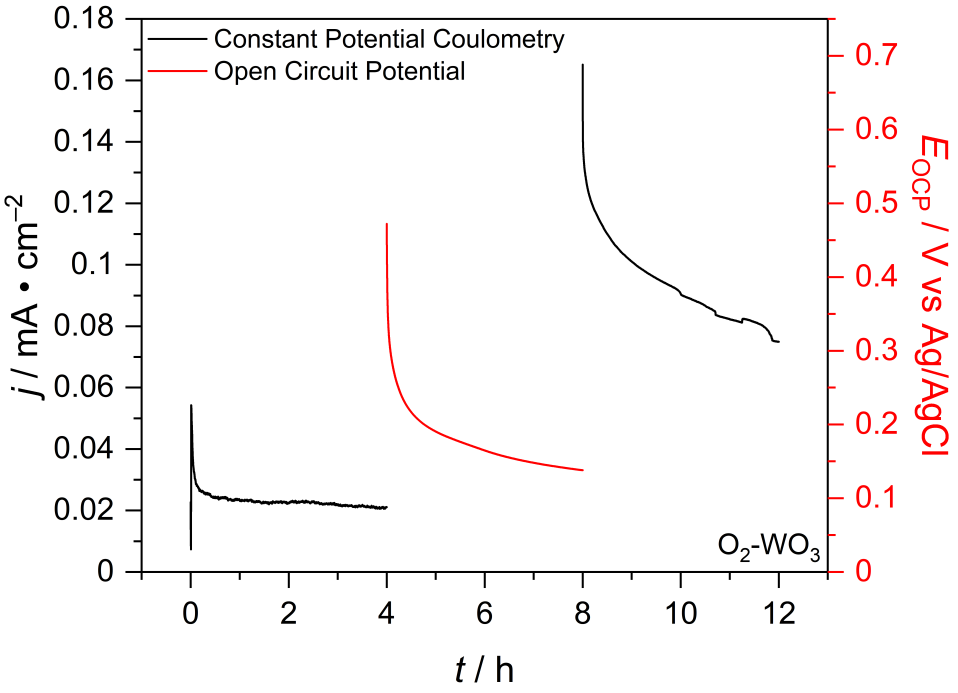

Figure 5.1: CPC at 0.98 V vs Ag/AgCl (black) and the measured open circuit potential (red) of oxygen annealed WO_3 films.

during the first twenty minutes but the response quickly flattens. After this initialy period, the stability is much higher than what is normally observed with H_xWO_3 films. The photocurrent density is much lower than what is typically observed with H_xWO_3 films. This result is unsurprising considering the oxygen thermal treatment was done to remove donor species from the material. After the initial four hour CPC experiment, the film was allowed to sit under AM 1.5 G illumination for an additional four hours while measuring the open circuit potential. The measured OCP is shown in the red trace of Figure 5.1. The OCP starts at high positive potential and initially trends sharply towards negative potentials. There is a delay between the end of the first 4-hour CPC experiment and the start of the OCP experiments due to the time required to save the data and begin the subsequent experiment. When the second CPC experiment starts at $t = 8$ h, the initial photocurrent density is nearly three times larger than the peak photocurrent density observed during the first CPC experiment ($0 \leq t \leq 4$). This behavior was described in Chapter 2. The data in Figure 5.1 demonstrates that O_2-WO_3 possesses lower donor density than H_xWO_3 which was synthesized throughout this work

due to the preemptive shift in the composition from H_xWO_3 to WO_3 caused by the change in annealing gas during synthesis. An increase is stability is seen at the expense of photocurrent density. This result is expected based on the conclusions from Chapter 2. Without proton bronze impurities to lose, the photocurrent density is more stable but the overall photocurrent density is lower because the donor density is lower. By allowing the O_2-WO_3 film to sit under AM 1.5 G illumination for four hours (Figure 5.1, red trace), the donor density is increased by the photochromic mechanism described in Chapter 2. The increase in donor density causes the photocurrent density observed at the start of the second CPC interval to be much higher than at any point during the first CPC interval. The O_2-WO_3 can form proton bronze just like what was seen with tungsten oxide films and powders in Chapter 2. The data in Figure 5.1 suggests that it is possible to alter the donor density during the chemical synthesis of the metal oxide.

Calcium nitrate salts were added to the ammonium metatungstate spin coat solution and the films were annealed in air to make doped H_xWO_3 and also under flowing O_2 to make doped O_2-WO_3. Chopped light linear sweep voltammograms were performed in a pH 1 sulfate solution under AM 1.5 G illumination to monitor any changes. The

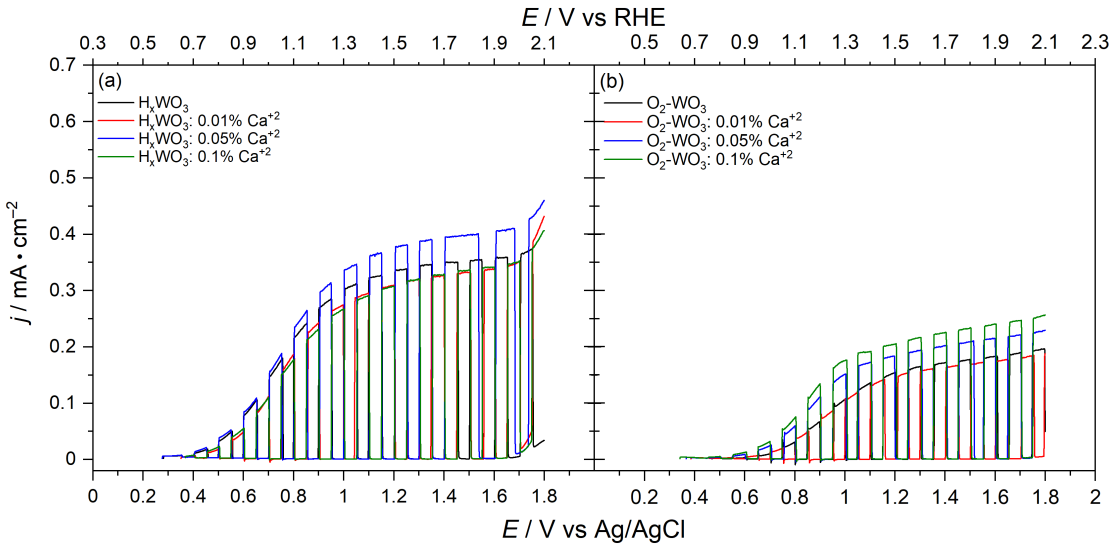

Figure 5.2: Chopped light linear sweep voltammogram comparison of calcium doped (a) H_xWO_3 and (b) O_2-WO_3 films in pH 1 sulfate solution.

photocurrent response is shown in Figure 5.2 for different levels of calcium doping as

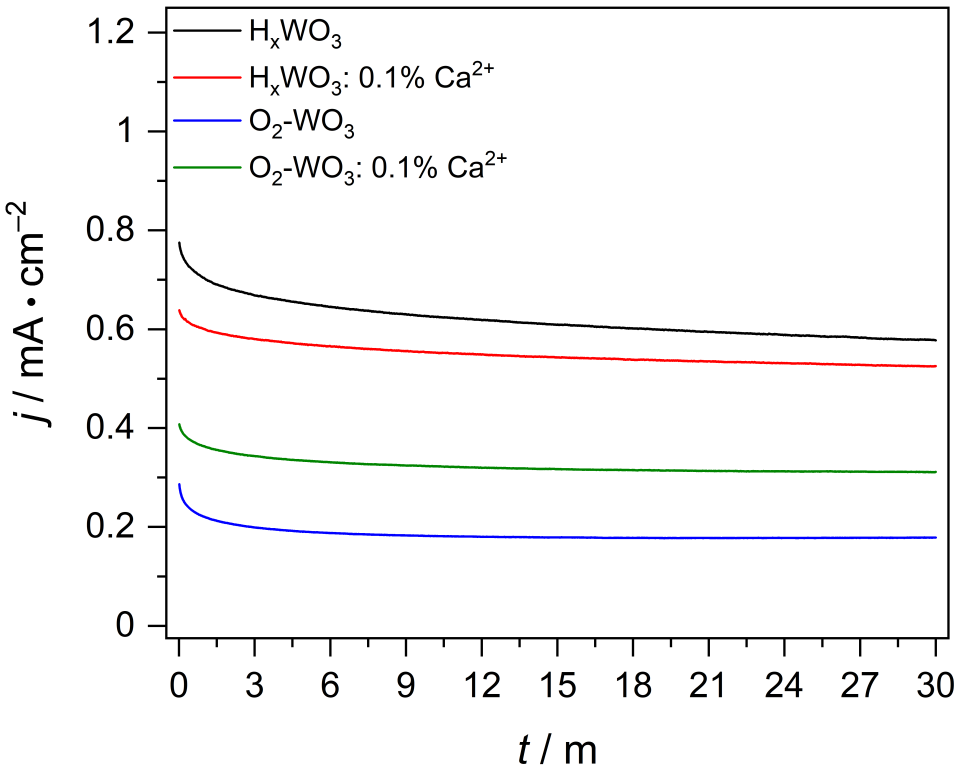

Figure 5.3: Stability test of H_xWO_3 (black) and O_2-WO_3 (blue) compared against 0.1% Ca^{2+} H_xWO_3 (red) and O_2-WO_3 (green) by CPC at 0.98 V vs Ag/AgCl in pH 1 sulfate solution.

measured by mole %. Although electrochromic tungsten oxide chemistry is generally illustrated with Group I cations, the synthesis approach to doping allowed for use of divalent cations. The hypothesis was that increased charge density of divalent cations would cause a stronger interaction with the metal oxide lattice, slowing the rate of deintercalation. The effect of adding calcium nitrate to the spin coat solution when making H_xWO_3 is shown in Figure 5.2a and is essentially negligible. In the case of O_2-WO_3 doped with calcium (Figure 5.2b), the addition of calcium appears to enhance the photocurrent density. An increase in photocurrent density is observed when 0.05% and 0.1% Ca^{2+} is added. These traces also exhibit a more negative onset potential for photocurrent compared to the undoped control and 0.01% Ca^{2+} trace. It should be noted that even 0.01 mole% Ca^{2+} ($\approx$ 20 ppm Ca^{2+}) is a large dopant concentration. Dopant levels are generally on the order of ppb. It does not seem that large levels of cation dopant strongly affects the photocurrent response. The effect of the calcium

dopants were also investigated with thirty minute CPC experiments which are shown in Figure 5.3. The largest photocurrent density was demonstrated by H_xWO_3 (Figure 5.3, black) but this also showed the largest decay in photocurrent. It appears as the though rate of decay of 0.1% Ca^{2+} (Figure 5.3, red) mirrors the rate of decay of H_xWO_3. The preemptive removal of tungsten bronze by oxygen annealing (Equation 5.3) causes high stability in the photocurrent density of O_2-WO_3 as shown by the blue trace in Figure 5.3. Addition of 0.1% calcium to O_2-WO_3 (Figure 5.3, green) increases the photocurrent density by about 70% when comparing the region at $t > 20$ minutes. The addition of calcium to O_2-WO_3 also exhibits the elevated stability in the photocurrent density. Calcium is larger and more charge dense than protons and these attributes may reduce the rate of oxidation and deintercalation. Thirty minutes is short amount of time and more exhaustive stability tests need to be performed.

Cesium was also incorporated into the ammonium metatungstate spin coat solution by dissolving $CsNO_3$ into the solution. The Cs^+ concentration was 0.5 mole % relative to the dissolved tungsten. Annealing was done using flowing O_2 during annealing to produce $O_2-Cs_xWO_3$, just as was done in Figure 5.1. In Figure D.1, a comparison between O_2-WO_3 and O_2-WO_3 is shown. No change in the photocurrent onset potential is observed, which is unexpected considering formation of proton bronze was shown to affect the onset potential in Chapter 2. However, a sharper rise in photocurrent is observed in the $O_2-Cs_xWO_3$ trace (Figure D.1, red trace) compared to the control O_2-WO_3 (Figure D.1, black trace).

5.2.2. Tungsten Bronze by Electrochemical Intercalation

The electrochemical formation of tungsten bronzes was also investigated and different treatments were compared based on the effect on photocurrent density and the onset potential of photocurrent. Because tungsten oxide is soluble in basic media

$$WO_3(s) + OH^-(aq) \longrightarrow {WO_4}^{2-}(aq) + H^+(aq) \tag{5.4}$$

Aqueous electrochemical experiments must take place in acidic media to maintain the chemical stability of WO_3. Electrochemical experiments in acidic media means that

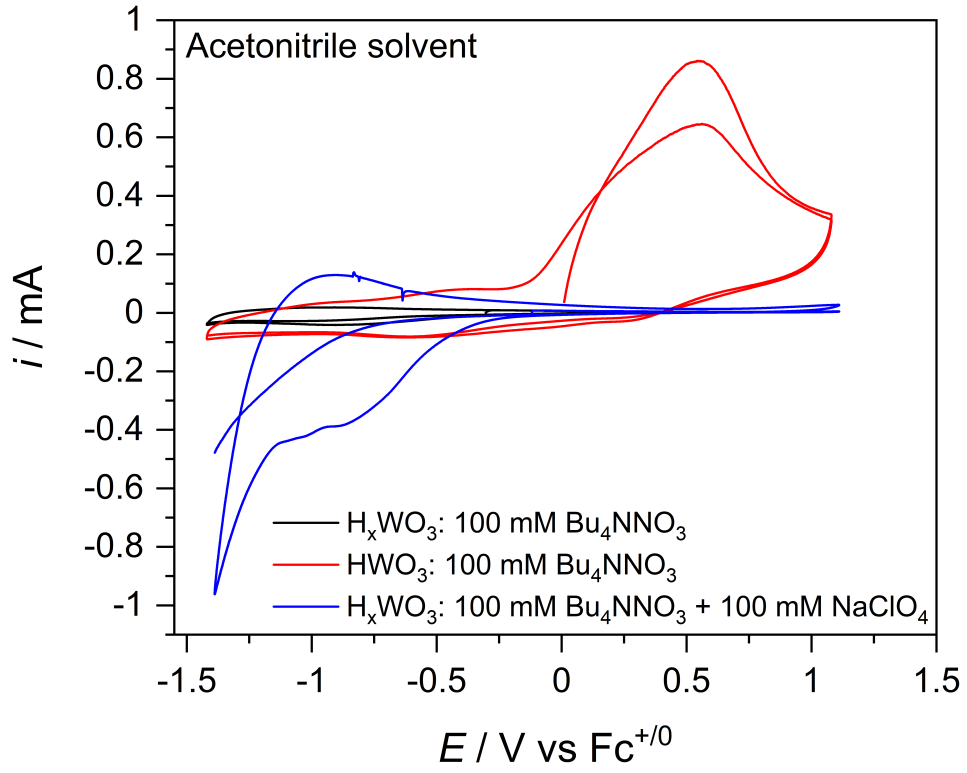

Figure 5.4: CV of different tungsten bronze materials in acetonitrile with Bu_4NNO_3 electrolyte. The bronzes investigated are H_xWO_3 (black), HWO_3 (red), and $NaWO_3$ (blue).

proton activity may interfere with measurements. To prevent this, acetonitrile can be used as the solvent to suppress proton activity. Using 100 mM tetrabutylammonium nitrate (Bu_4NNO_3) as the electrolyte, the cyclic voltammograms (CV) shown in Figure 5.4 were performed to determine how the cation identity affected the W^{+5} to W^{+6} oxidation. The CV traces scan towards positive potential initially and end at -1.5 V vs $Fc^{+/0}$. The CV traces are reported versus the ferrocenium/ferrocene reduction potential. The CV trace for a H_xWO_3 electrode is shown in black and exhibits a very small redox wave near -1 V vs $Fc^{+/0}$. The proton bronze concentration in H_xWO_3 was shown to be 0.02% in Chapter 3 and we do not expect a large oxidation event. A H_xWO_3 electrode was loaded with proton bronze in an aqueous 1 M H_2SO_4 solution by performing a CV and ending at -1 V vs Ag/AgCl. This is sufficient to turn the electrode deep blue due to the formation of HWO_3. This HWO_3 electrode was then taken and placed into the 100 mM Bu_4NNO_3 acetonitrile solution and the CV was performed again, displayed in

the red trace. The onset potential for oxidation of proton bronze is at about 0 V vs $Fc^{+/0}$ and shows a large wave due to the degree of reduction in the aqueous 1 M H_2SO_4 solution. A CV was also performed in the electrolyte solution with $NaClO_4$ added. This allowed for the observation of the sodium intercalation and deintercalation in acetonitrile (Figure 5.4, blue) which occurs at -1 V vs $Fc^{+/0}$. Proton bronze oxidation occurs at a more positive potential vs $Fc^{+/0}$ compared to sodium bronze, which occurs at -1 V vs $Fc^{+/0}$. It may be that large cations do not stabilize the W^{+5} species as effectively as protons and so the oxidation of sodium bronze occurs more negative than proton bronze. A more positive potential vs $Fc^{+/0}$ is required to oxidize proton tungsten bronze than sodium tungsten bronze. From these results, proton tungsten bronze would be expected to be more stable relative to a sodium tungsten bronze based on the potential vs $Fc^{+/0}$

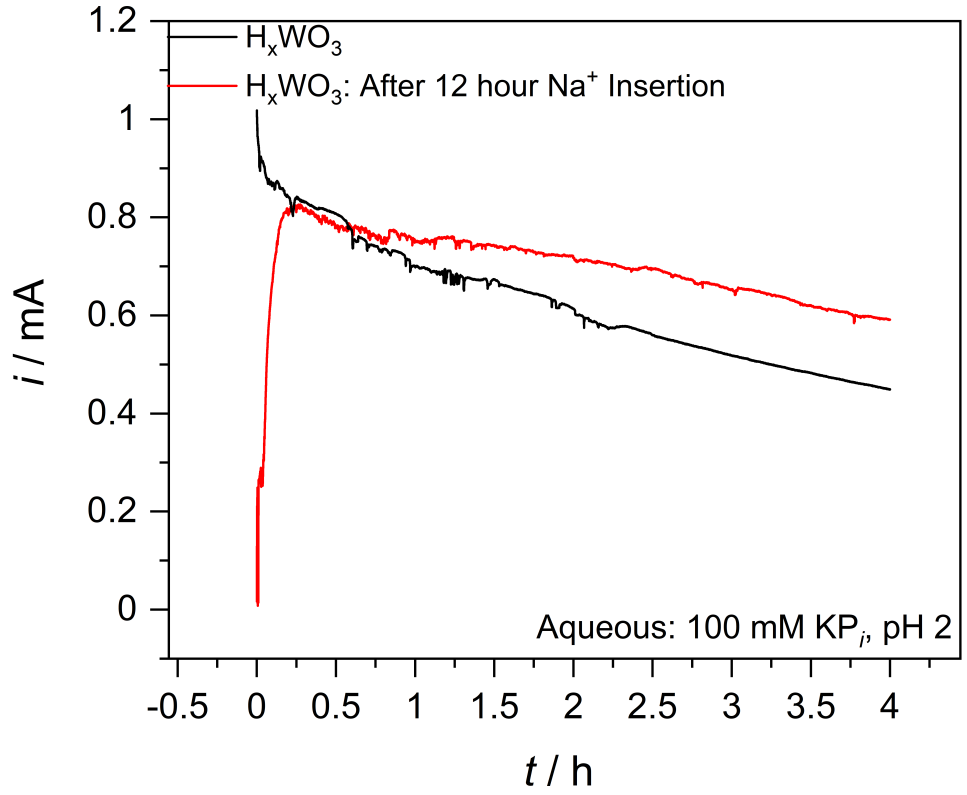

Figure 5.5: Comparison of CPC behavior from H_xWO_3 (black) and H_xWO_3 (red) after galvanostatic sodium intercalation. Electrodes poised at 0.98 V vs Ag/AgCl and illuminated by AM 1.5 G light.

required to oxidize the bronze. However, this conclusion comes from a comparison of

sodium intercalation in acetonitrile with the oxidation of HWO_3 in acetontrile.

Using a 100 mM Bu_4NNO_3, 100 mM $NaClO_4$ in acetonitrile solution, sodium was intercalated into H_xWO_3. 10 nA of cathodic current was passed through the H_xWO_3 film galvanostatically for twelve hours to slowly introduce sodium into the material. At the end of the twelve hour galvanostatic experiment, the film was placed into a 100 mM potassium phosphate solution set to pH 2. The film was illuminated by AM 1.5 G illumination. The film was then poised at 0.98 V vs Ag/AgCl and the photocurrent was measured. Figure 5.5 shows the photocurrent response of H_xWO_3 in black and also the photocurrent response of H_xNaWO_3 after galvanostatic intercalation of sodium in red. The photocurrent of H_xNaWO_3 begins near zero but slowly increases with time until it peaks at about $t = 15$ min. Tungsten bronze become metallic if the concentration of bronze gets too high.[1] If too much sodium had been intercalated galvanostatically, then the rise in photocurrent may be due to the oxidation of excess sodium bronze and the drop in donor density to semiconductor levels. The H_xNaWO_3 film exhibits greater photocurrent stability over the four hour CPC experiment. This experiment was done with magnesium as well. Using a 100 mM $Mg(ClO_4)_2$, 100 mM Bu_4NNO_3 acetonitrile solution, 5 nA was passed cathodically in a galvanostatic experiment. A the end of the twelve hours, a CPC experiment in 100 mM potassium phosphate set to pH 2 was performed. The film was illuminated with AM 1.5 G light and poised at 0.98 V vs Ag/AgCl. The photocurrent response is shown in Figure D.2. The photocurrent of H_xMgWO_3 (Figure D.2, red) is higher than H_xWO_3 (Figure D.2, black) but appears to decay at the same rate as the H_xWO_3 control.

5.2.3. Future Directions With Tungsten Bronze

While incorporation of cations into tungsten oxide consistently increased the observed photocurrent, increasing the stability in photocurrent was found to be more challenging. An effective strategy may be to employ a gradient in the tungsten bronze concentration. The work in Chapter 2 demonstrated that increasing the donor density with proton bronze raised the Fermi level. This can be exploited in the synthesis of light absorbing tungsten oxide films. If the concentration of tungsten bronze near the back contact is low while the concentration of tungsten bronze near the WO_3–solution interface is high,

a gradient in the Fermi level will be created that will assist in separating photogenerated charge carriers. To address the problems with stability, the findings in Chapter 3 suggest that after the optimal synthesis of a tungsten bronze doped WO_3 has been found, depositing an electrocatalyst like FeOOH will help to prevent oxidation of the beneficial tungsten bronze impurities.

5.3. Photocatalyzed Anelli-Montanari Protocol

In Chapter 3 we demonstrated the enhanced stability afforded by chloride oxidation over water oxidation. In Chapter 4, we used the hypochlorous acid product to oxidize ethanol and 2-propanol. This work was directed by the Anelli-Montanari protocol, which employs TEMPO (2,2,6,6-tetramethylpiperidinyloxyl) to perform selective oxidations. TEMPO is the species which peforms the oxidation but the reaction requires

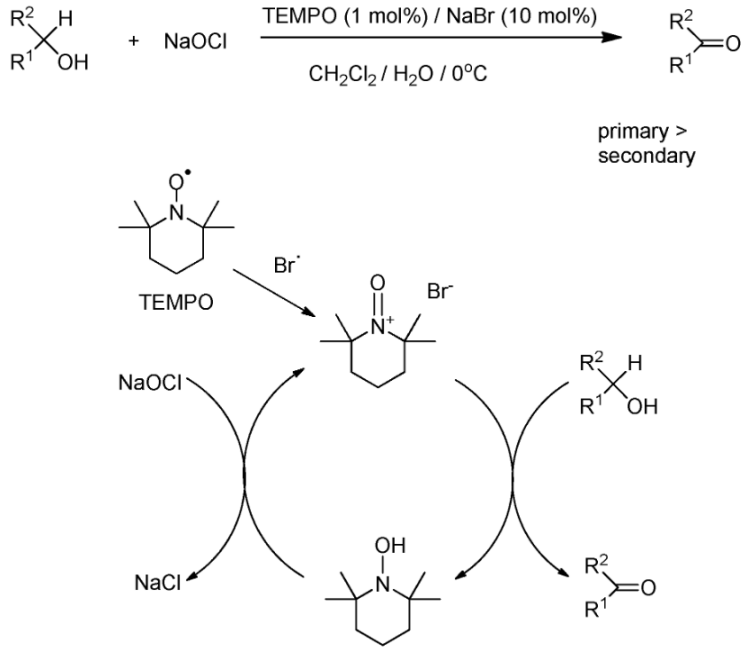

Figure 5.6: TEMPO catalyzed oxidations of alcohols using hypochlorite anion as the terminal oxidant. Reproduced from reference 2

stoichiometric quantities of free chlorine oxidant to drive the reaction.[3] Hypochlorous acid is highly reactive but generally non-selective. The results from Chapter 4 are extremely promising for incorporation of chloride oxidation on H_xWO_3. An initial attempt

was made to use TEMPO with the procedure outlined in Chapter 4. The experiment was not performed at 0 °C as illustrated by the conditions in Figure 5.6. A two compartment cell separated by Nafion was used with 35 mL of electrolyte in each compartment. The conditions were the same as those used for H_xWO_3 photodriven oxidations of alcohols described in Chapter 4. In this attempt, only 49% of the charge passed resulted in oxidation of the ethanol. Without TEMPO, about 90% of the charge passed by H_xWO_3 goes to ethanol oxidation (see Chapter 4). TEMPO is makes the aqueous solution slightly orange and after the alcohol oxidation experiment, all orange color from the working electrode compartment. The color of the counter electrode compartment was unaffected. Together, these results suggest that TEMPO was destroyed during the reaction. Successfully incorporating TEMPO into chloride oxdiation on H_xWO_3 will likely require performing the photoreaction at 0 °C as described in Figure 5.6.

5.4. Concluding Remarks

The results presented here represent the investigation of how two different fuel forming reaction occur on a single material. The majority of solar fuel research has focused on the water oxidation reaction while ignoring the chloralkali process. Water oxidation may proceed through separate one-electron transfer processes, which means the 1.23 V vs NHE value does not reflect the potential required to reach these one-electron transfer intermediates. Therefore, it may be that chloride oxidation occurs with thermodynamic advantage over water oxidation.

References

[1] Bullett, D. W. Bulk and surface electron states in WO_3 and tungsten bronzes. *J. Phys. C: Solid State Phys.* **1983**, *16*, 2197–2207.

[2] Sheldon, R. Fundamentals of Green Chemistry: Efficiency in Reaction Design. *Chem. Soc. Rev.* **2012**, *41*, 1437–51.

[3] Anelli, P.; Biffi, C.; Montanari, F.; Quici, S. Fast and selective oxidation of primary alcohols to aldehydes or to carboxylic acids and of secondary alcohols to ketones mediated by oxoammonium salts under two-phase conditions. *Journal of Organic Chemistry* **1987**, *52*, 2559–2562.

Appendix A.

Supporting Information for Chapter 2

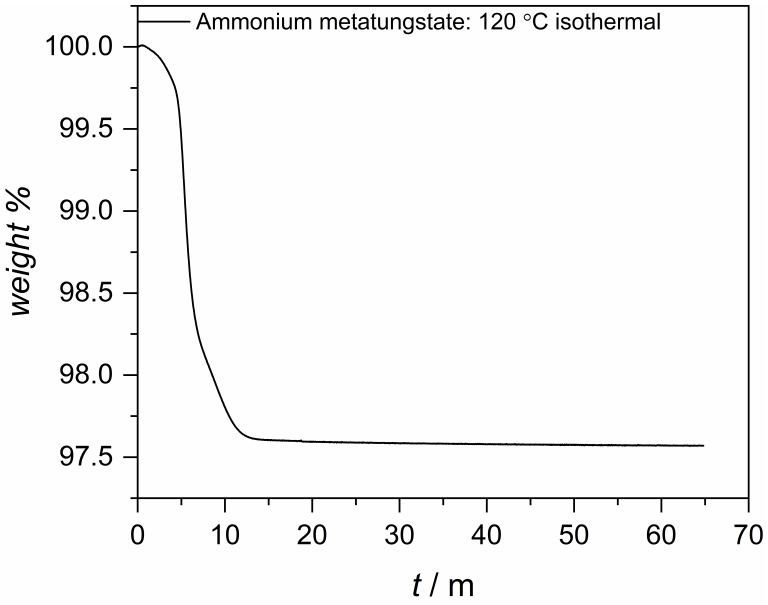

Figure A.1: Thermogravimetric analysis of ammonium metatungstate (AMT) powder purchased from Sigma-Aldrich. 20 °C / minute ramp rate to 120 °C isothermal holding temperature. Performed under N_2 gas flowing at 60 mL / minute. Found to contain 3.1 moles H_2O per mole AMT.

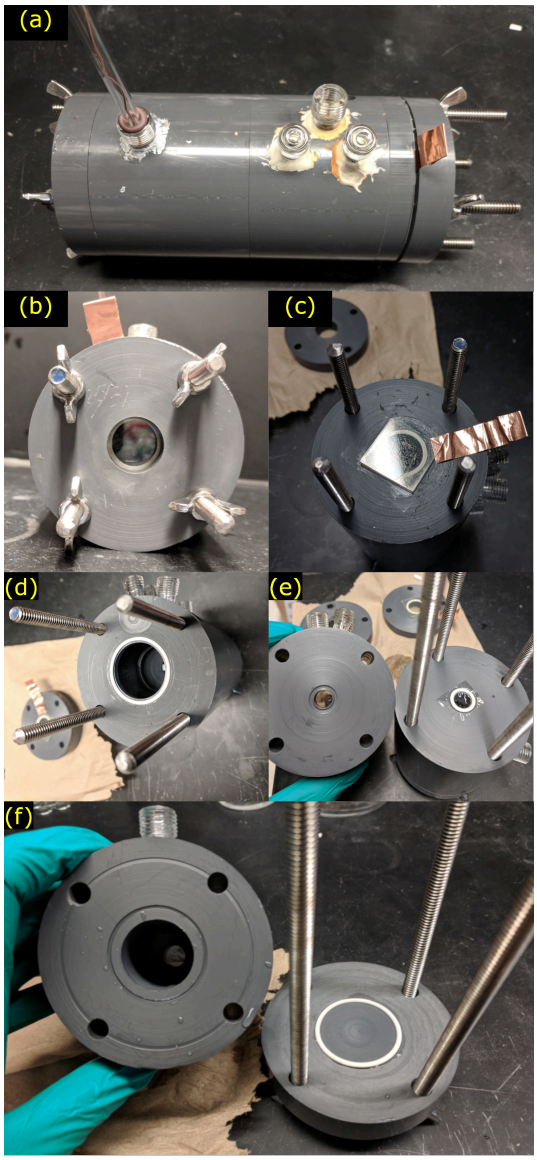

Figure A.2: Oxygen flow cell used for determining oxygen production rate. Machined from PVC, the cell is composed of two components separated by a Nafion™ membrane from Fuel Cell Earth. Assembled cell (a) compressed by four threaded rods. Front image (b) showing exposed WO_3 and showing copper tape connected to electrode (c). Working electrode compartment (d) and O-ring grooves are shown for working electrode compartment (e, left) as well as the counter electrode compartment with Nafion™ and O-ring (e, right). O-ring kept on working electrode compartment side. The inside of the counter electrode compartment (f, left) is shown with the back plate and O-ring (f, right).

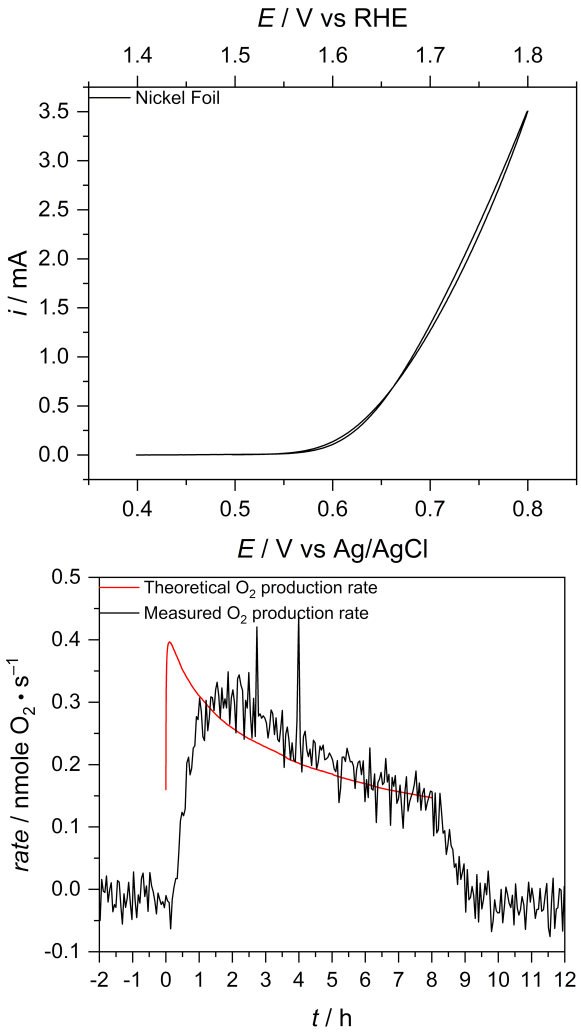

Figure A.3: Assessment of the oxygen flow cell performed with nickel foil (electrode foil area approximately 0.01 cm^2) in 1 M NaOH. Cyclic voltammetry (top) performed at 10 mV $\cdot$ s^{-1} was used to determine the potential to apply during electrolysis. 0.6 V vs Ag/AgCl was chosen to achieve an oxygen production rate lower than 0.5 nmole O2 $\cdot$ s^{-1} because this rate is below the oxygen production rate of the WO_3 photoelectrodes used in this work. The control experiment (bottom) was performed by applying 0.6 V vs Ag/AgCl to the Ni foil electrode in 1 M NaOH and measuring the oxygen production rate by flow cell analysis. Measured Faradaic efficiency determined by dividing area under measured rate (black trace) by the theoretical rate (red trace). Limits of integration for black trace start at beginning of electrolysis ($t = 0$) and end when the measured rate crosses the x-axis. 99.5% Faradaic efficiency measured on Ni foil in 1 M NaOH by flow cell analysis, validating the experimental design.

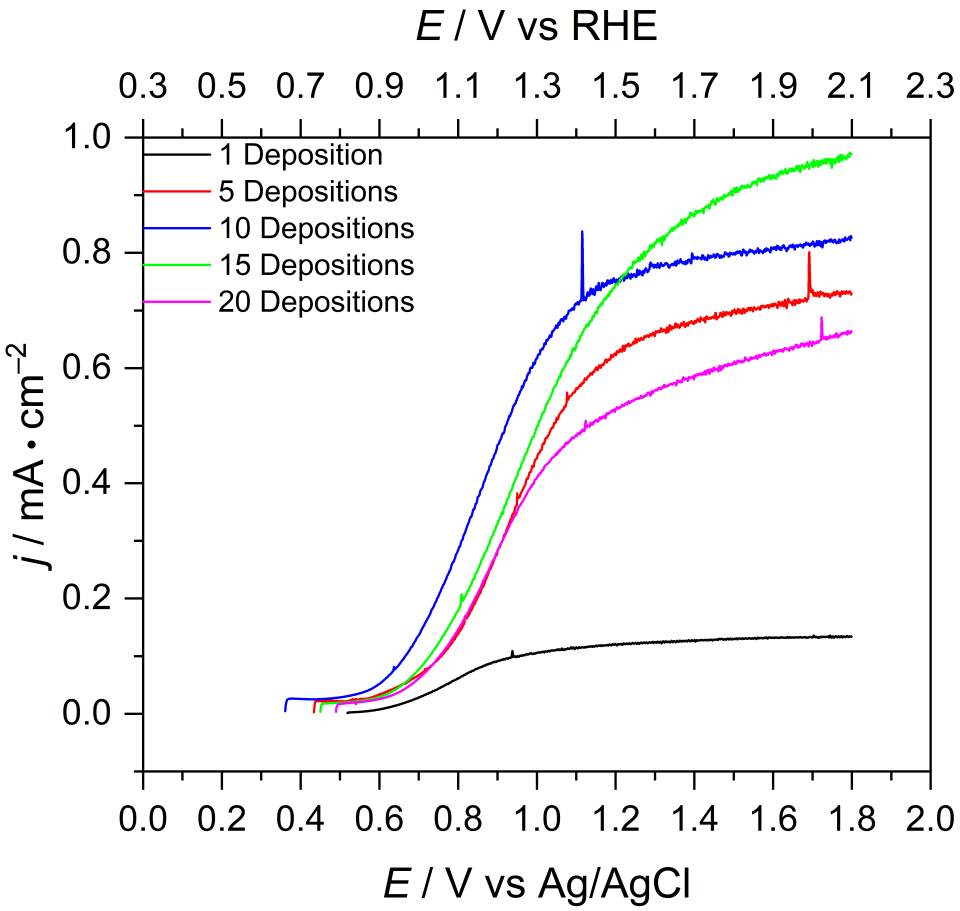

Figure A.4: Linear sweep voltammograms to determine the appropriate number of depositions when making WO_3 films. A given number of depositions was performed on clean FTO substrates and the LSV was recorded for each trial in pH 1 sulfate solution under 100 mW · cm^{-2} AM1.5G illumination. 10 cycles of deposition followed by annealing at 500 °C afforded films with highest photocurrent at 1.23 V vs RHE.

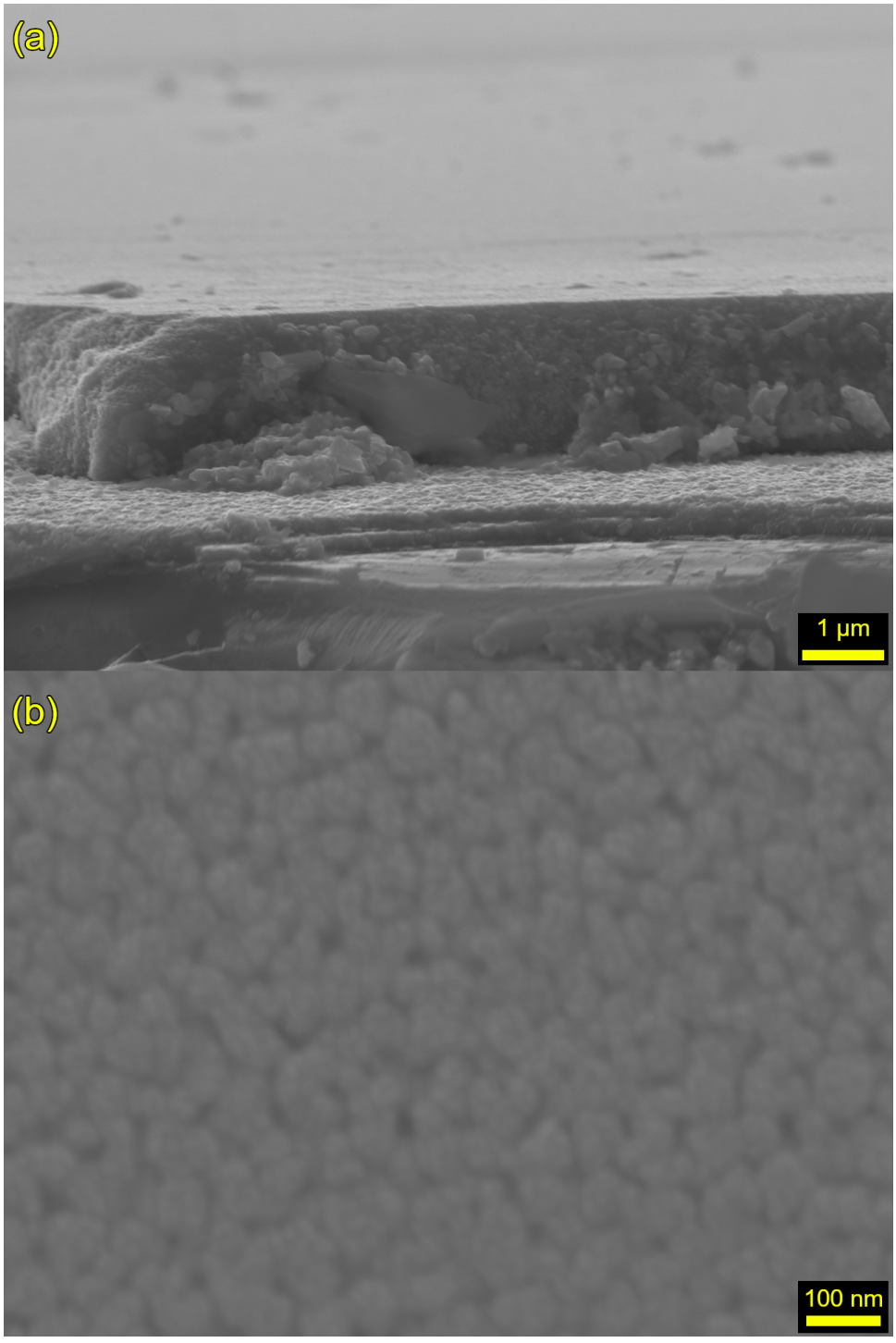

Figure A.5: SEM image of WO_3 deposited on FTO substrate (a) side-on with 5° stage tilt showing an approximate 2 micrometer thickness and (b) top down showing surface structure.

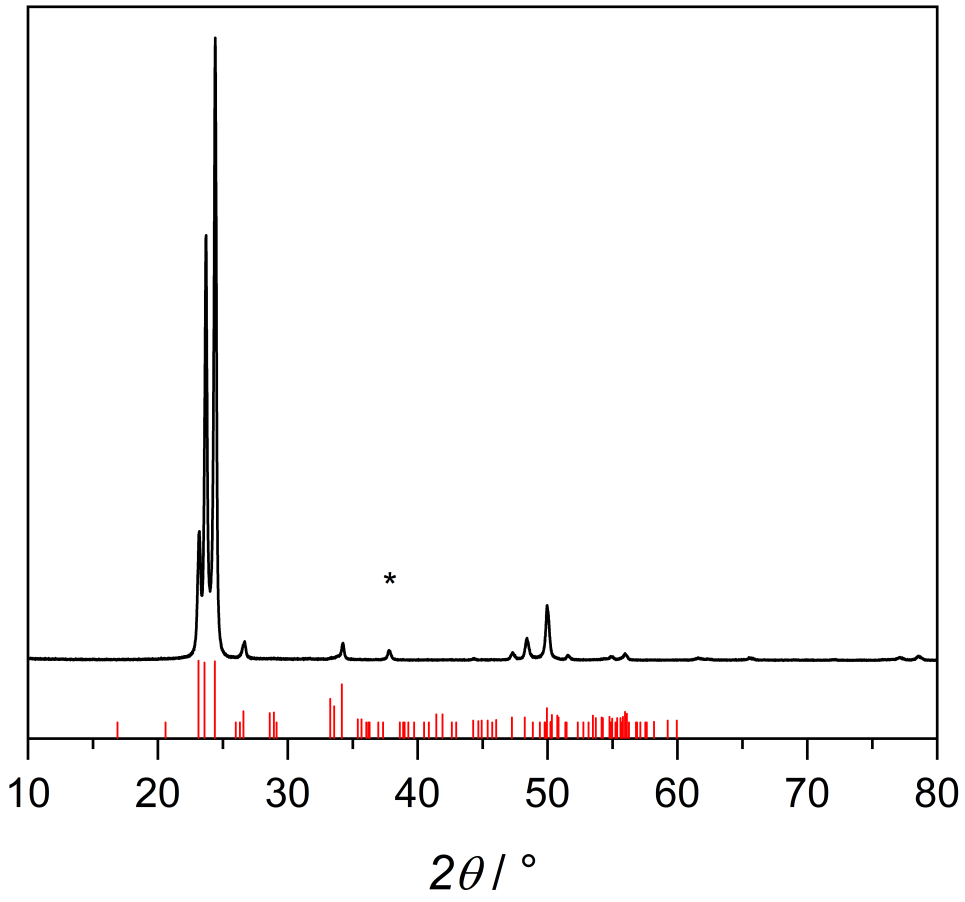

Figure A.6: XRD of WO3 deposited on FTO substrate. Vertical red lines represent indexed monoclinic Bragg reflection from JCPDF 72-0677. Asterisk denotes peak from FTO substrate.

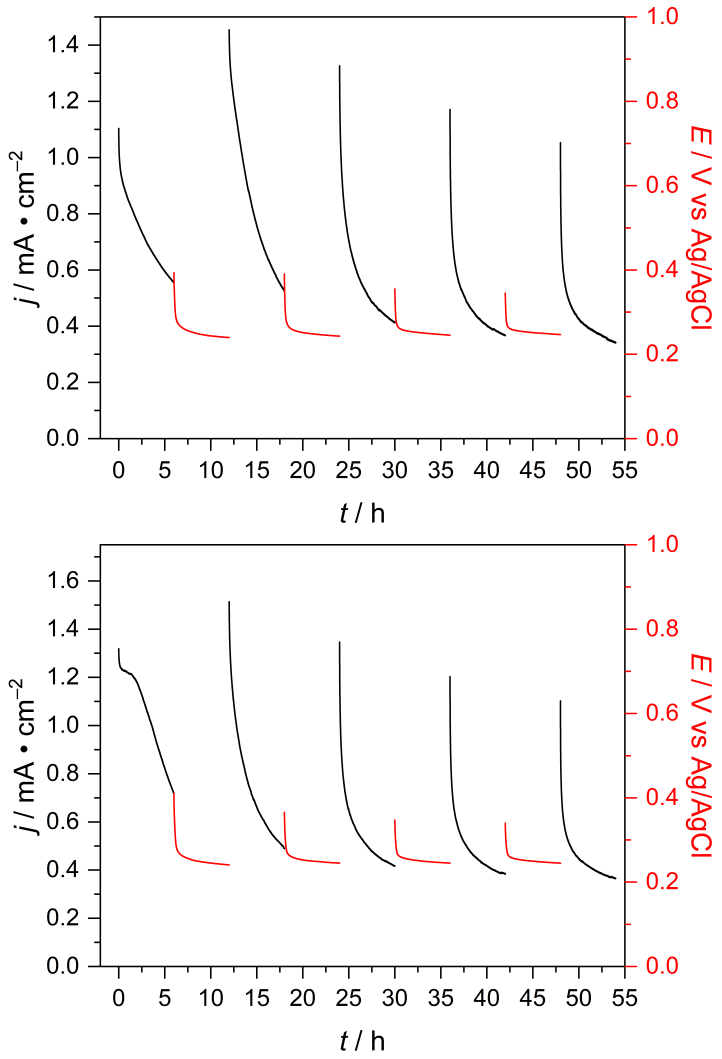

Figure A.7: Replicate experiments of Figure 2.1. Performed in pH 1 sulfuric acid solution under 2-sun AM1.5G illumination. Four cycles of CPC at 0.98 V vs Ag/AgCl for 6 hours followed by 6 hours at open circuit under illumination. A final CPC experiment was performed after the fourth CPC/OCP cycle. The photocurrent profile of first CPC measurement is variable but subsequent CPC measurements show the same general current profile across different trials. Recovery of photocurrent is seen consistently after extended illumination at open circuit. Open circuit potential measurements consistently show a negative shift in the OCP during illuminated rest.

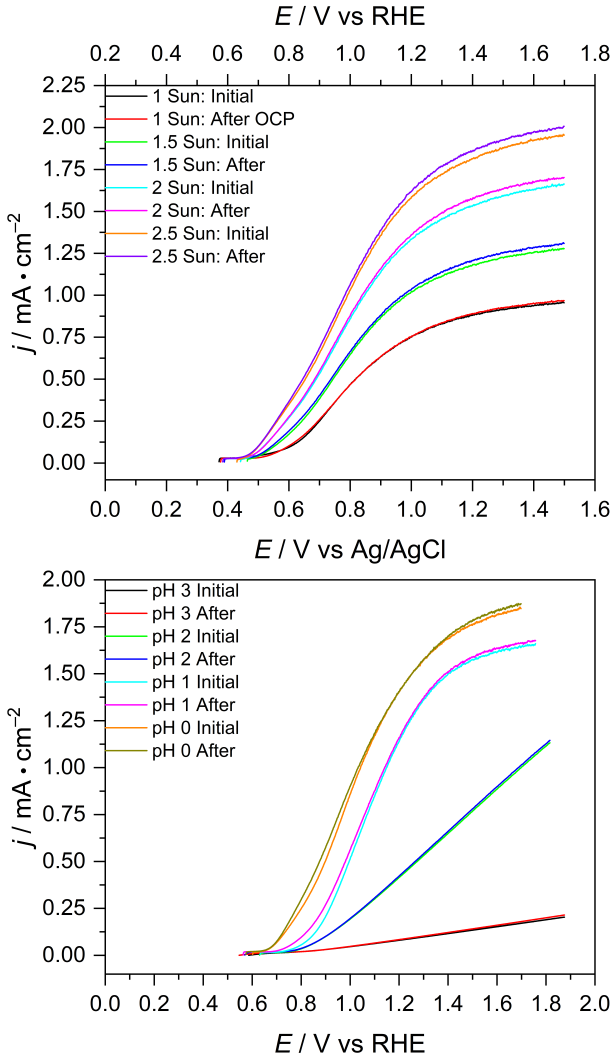

Figure A.8: (Top) Effect of light intensity on increase in LSV photocurrent in pH 0 sulfuric acid solution. Starting with 1 sun light intensity, an initial LSV sweep was taken from open circuit potential to 1.5 V vs Ag/AgCl. After the first LSV measurement, the electrode sat at open circuit potential for 15 minutes under the same light intensity. After the illuminated rest, the LSV sweep was retaken again. The light intensity was then increased, and the process was repeated for the next light intensity. (Bottom) Performed under 2 sun illumination. Starting with pH 3 sulfuric acid electrolyte solution, the cell was rinsed with approximately 400 mL of electrolyte solution and then filled. An initial LSV sweep was recorded and the film sat at open circuit conditions for 15 minutes. After the 15-minute rest, the LSV sweep was measured again. The cell was then rinsed with the subsequent electrolyte before filling. For both the top and bottom plots, the photocurrent at 1.5 V vs Ag/AgCl after 15 minutes rest was compared against the photocurrent at 1.5 V vs Ag/AgCl in the initial LSV measurement.

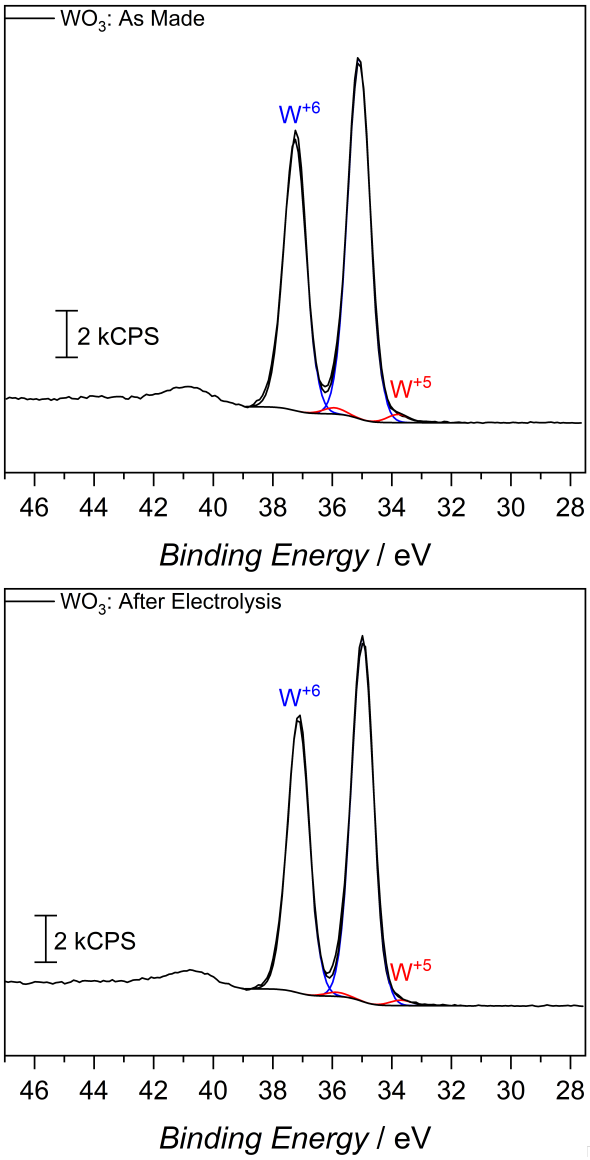

Figure A.9: XPS spectra of the WO_3 films used in this work. Top spectra taken before and bottom spectra taken after 24 hour chronoamperometry under 100 $mW \cdot cm^{-2}$ AM1.5G illumination in pH 1 sulfate solution. Surface tungsten states were measured to be 2.2% W^{+5} before chronoamperometry and decreased to 1.4% W^{+5} after electrolysis.

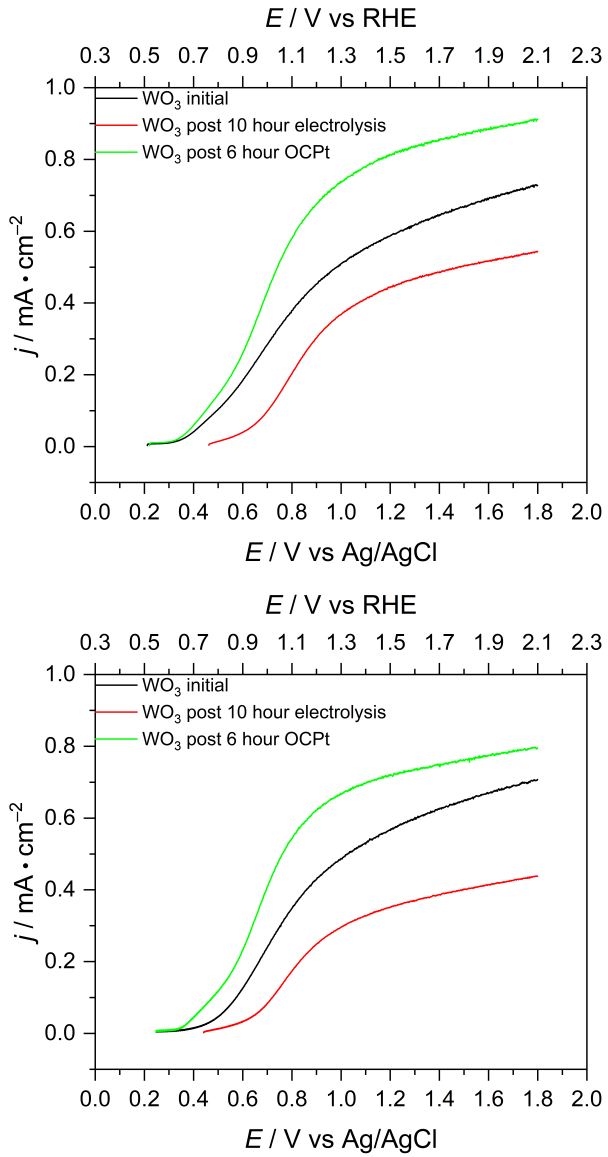

Figure A.10: Replicate experiments of Figure 2.7. Performed in pH 1 sulfuric acid under 1-sun AM1.5G illumination. Shown in each plot is the LSV response of a single H_xWO_3 film at different timepoints. The as-prepared (black) LSV response drops in performance after 10 hours of CPC at 0.98 V vs Ag/AgCl when the LSV is retaken (red). Following 6 hours of rest at open circuit under 1-sun illumination, the LSV response (green) shows elevated current response compared to the as-prepared response.

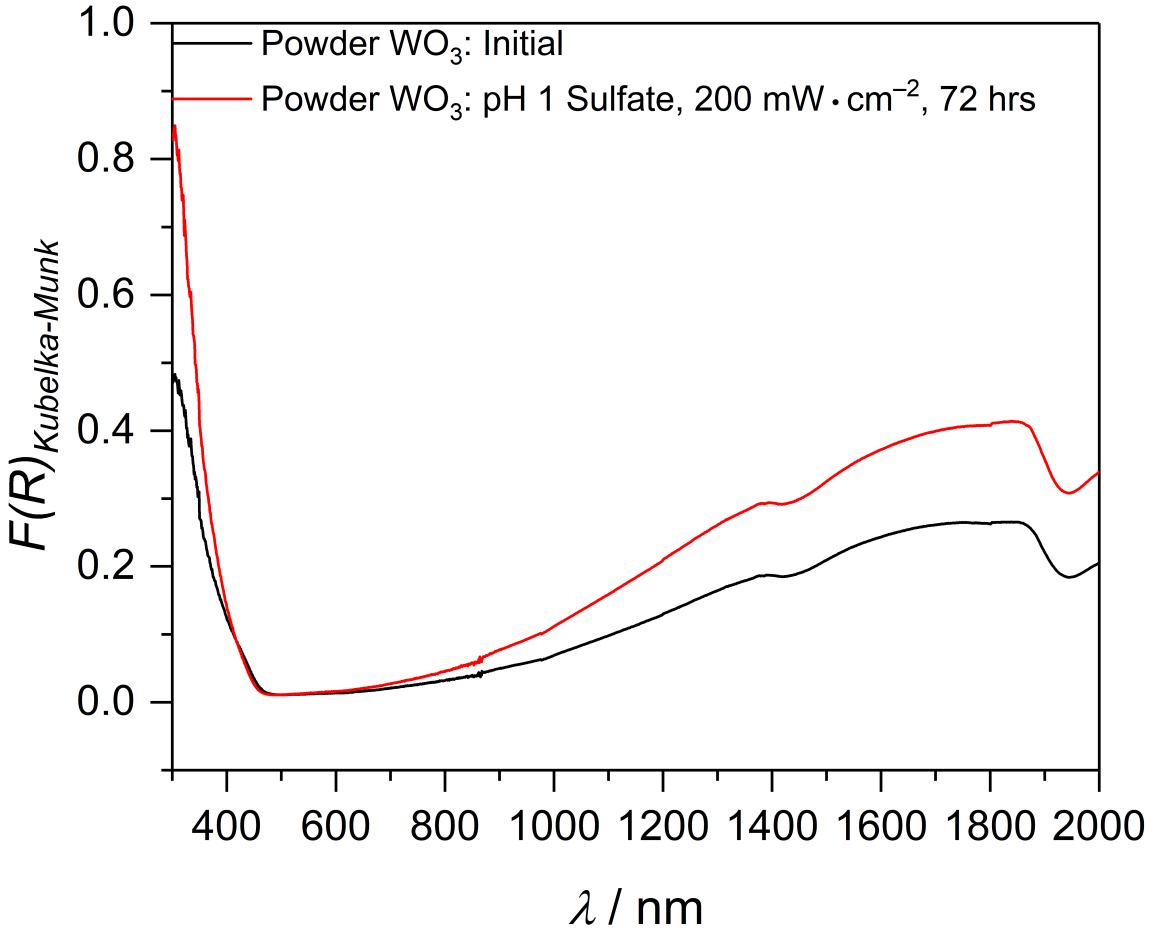

Figure A.11: UV-Vis-NIR diffuse reflectance measurement of WO_3 powder purchased from Sigma-Aldrich. Initial trace from the bottle (black trace) exhibits an increase in absorption following illumination. After 72 hours in pH 1 sulfuric acid solution under 2-sun illumination, WO_3 powder (red trace) shows an increase in NIR absorption due to electrochromic H_xWO_3 as well as an increase in the <420 nm light region due to an increase in charge carriers. UV-Vis samples prepared by thoroughly grinding 10 mg of WO_3 powder with 90 mg of $BaSO_4$ powder.

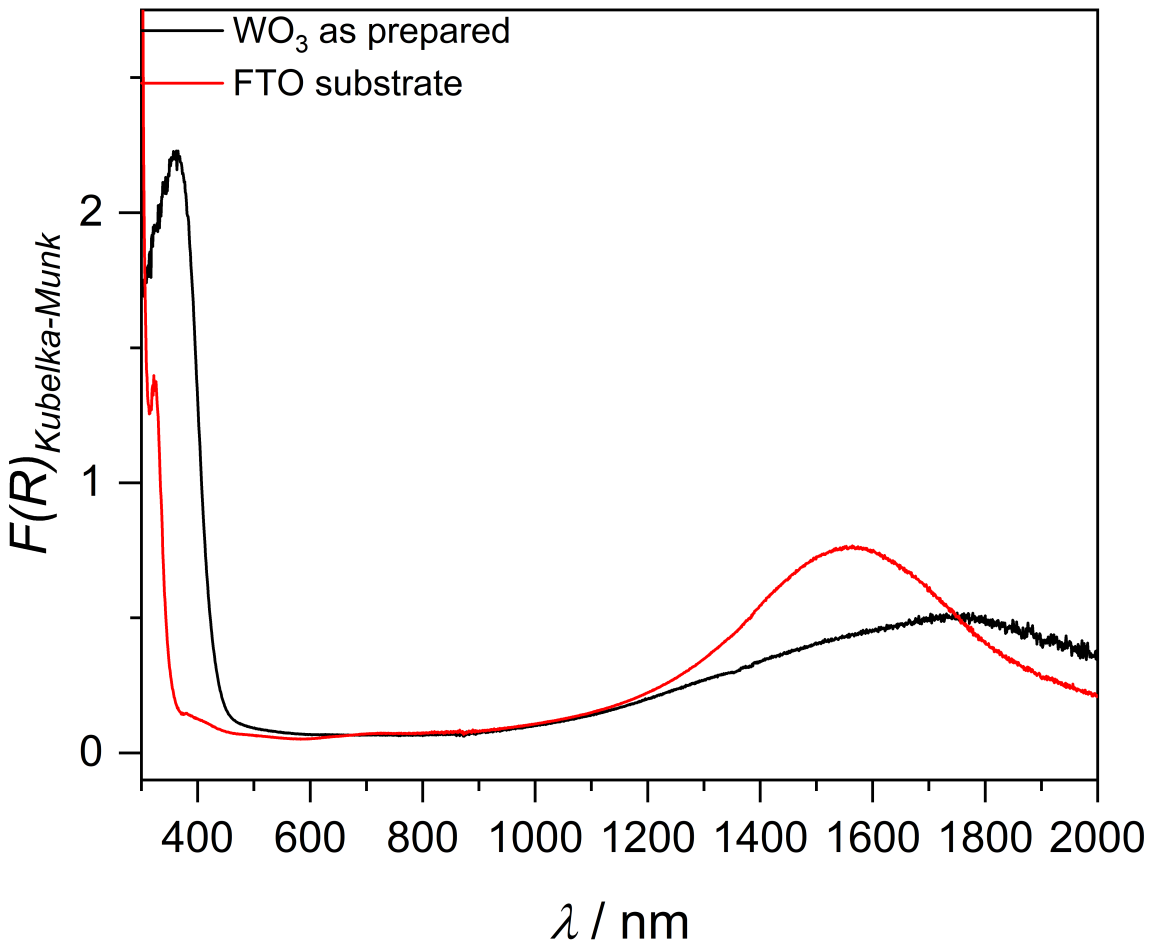

Figure A.12: UV-Vis-NIR vis diffuse reflectance measurement of spin coated WO_3 on FTO substrate. NIR absorption is observed in these films as prepared. The films used are transmissive. Included is diffuse reflectance of the FTO substrate which shows its own NIR absorption, although shifted from the WO_3 signal.

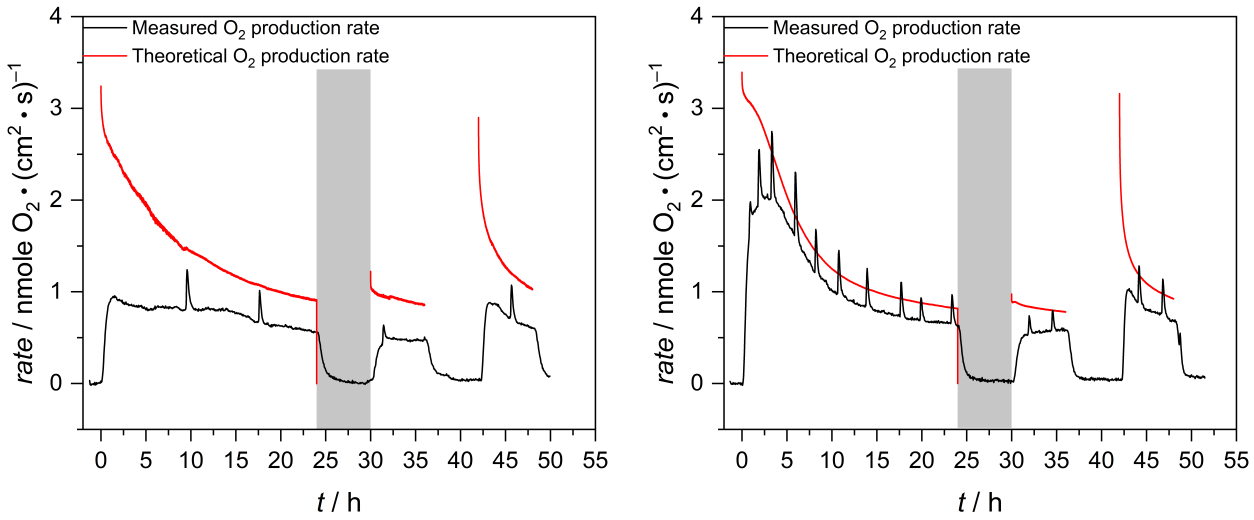

Figure A.13: Replicates of Figure 2.8. Performed in pH 1 sulfuric acid solution with an exposed area of 2.41 cm^{-2}. The grey region corresponds to the dark and all other regions are under 2-sun AM 1.5 G illumination. Faradaic efficiency of the first replicate (left) was 52.3% for the first 24-hour CPC, 57.3% for the second 6-hour CPC, and 57.2% for the final 6-hour CPC measurement. Faradaic efficiency of the second replicate (right) was 80% for the first 24-hours of CPC, 76% for the second 6-hour CPC, and 76% for the final 6-hour CPC measurement.

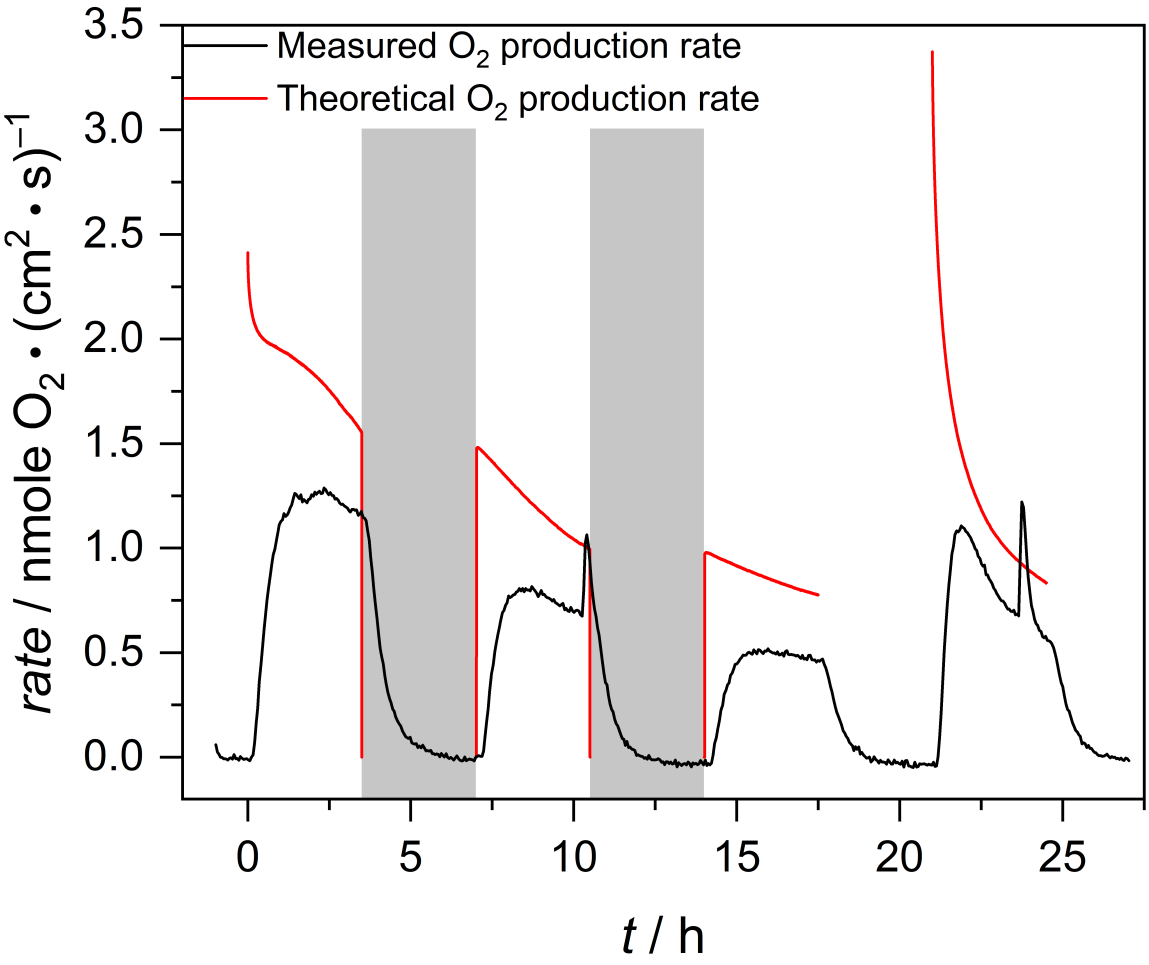

Figure A.14: Measured oxygen production on H_xWO_3 electrodes in pH 1 sulfuric acid. CPC was performed a total of 4 times for 3.5 hours at 0.98 V vs Ag/AgCl. Oxygen production was measured during the entire experiment. The electrode rested at open circuit for the 3.5-hour periods between CPC measurements. Regions in grey are under the dark, all other regions are under 2-sun AM 1.5 G illumination. This data was collected at the same time as the data used in Figure 2.2, meaning that the theoretical O_2 production rate in this figure was calculated using the current density shown in Figure 2.2. Faradaic efficiency was measured as 67% for the first CPC measurement, 64% for the second, 56% for the third. After resting at open circuit conditions under illumination for 3.5 hours, the fourth CPC measurement exhibited a Faradaic efficiency of 68% and a recovery in photocurrent which coincided with a recovery in the rate of OER.

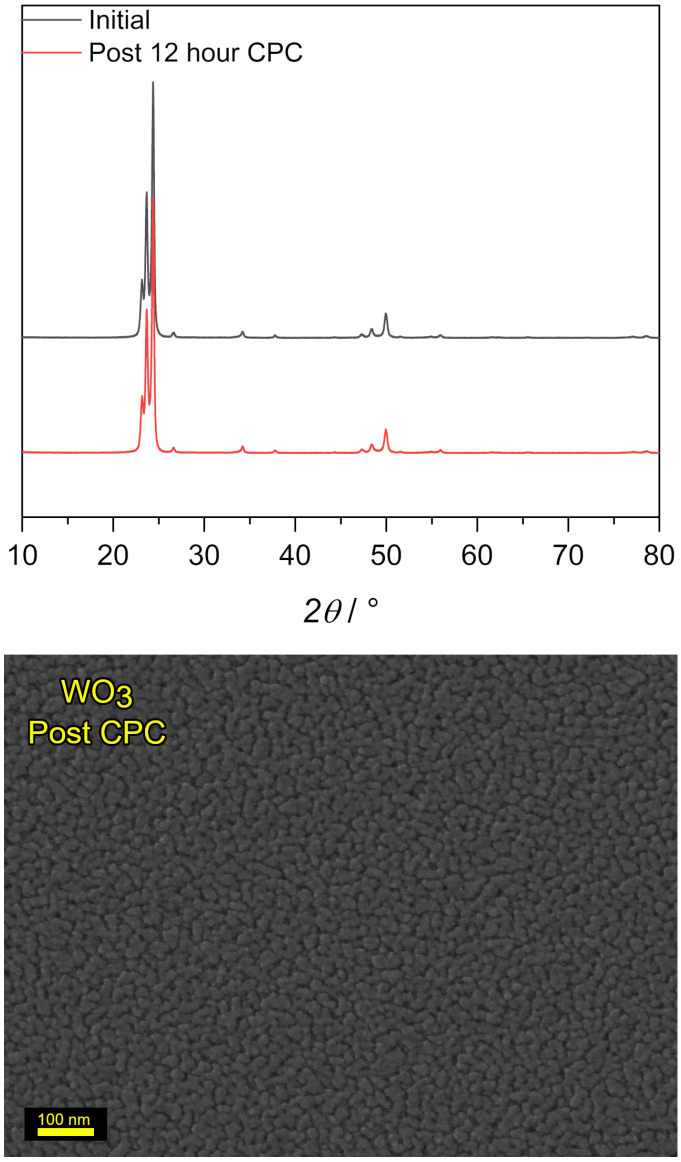

Figure A.15: Powder XRD pattern (top) and SEM image (bottom) of WO_3 recorded after 12 hours of CPC at 0.98 V vs AgCl under 1-sun illumination in pH 1 sulfuric acid solution. Relative peak intensities are preserved before and after CPC in the XRD patterns. The lack of new peaks forming or peaks disappearing suggests preservation of bulk morphology. By SEM, the surface morphology appears to be unchanged when compared to the SEM image presented in Figure B.8b. Together, these results further support a non-destructive mechanism when describing the loss of photoactivity seen in WO3 photoelectrodes during PEC OER operation in aqueous media.

Appendix B.

Supporting Information for Chapter 3

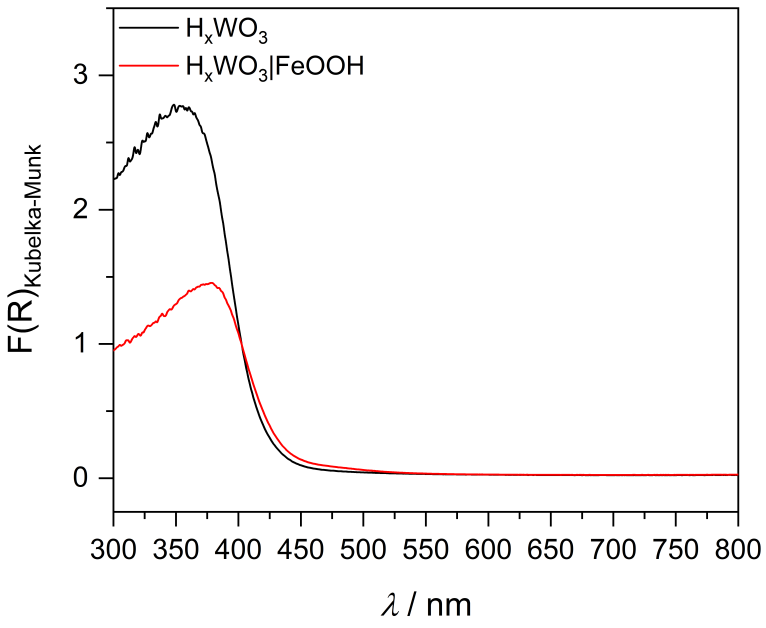

Figure B.1: UV-Vis diffuse reflectance of H_xWO_3 and H_xWO_3|FeOOH. The deposition of FeOOH leads to parasitic light absorption, resulting in a lower absorption for light < 400 nm

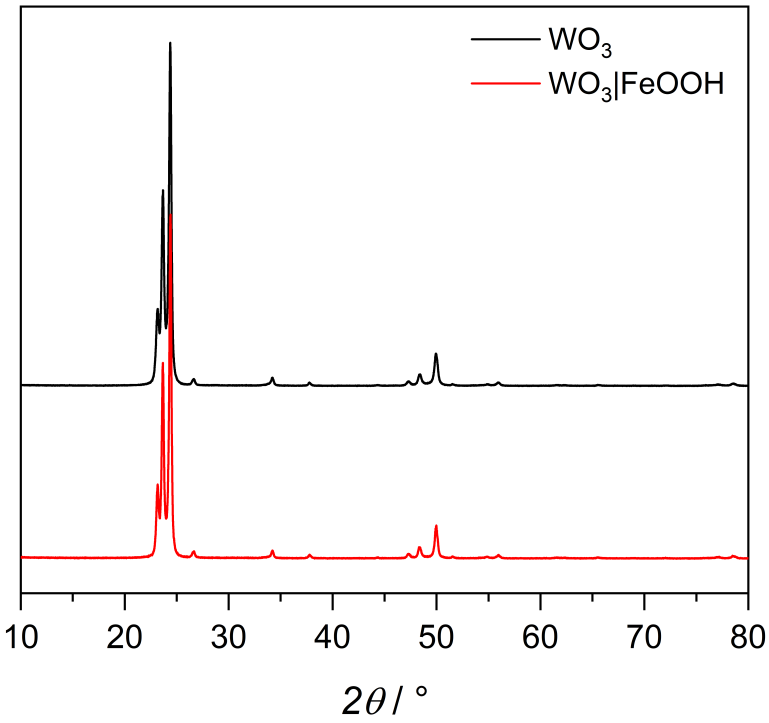

Figure B.2: XRD of WO_3 and WO_3|FeOOH deposited on FTO substrate.

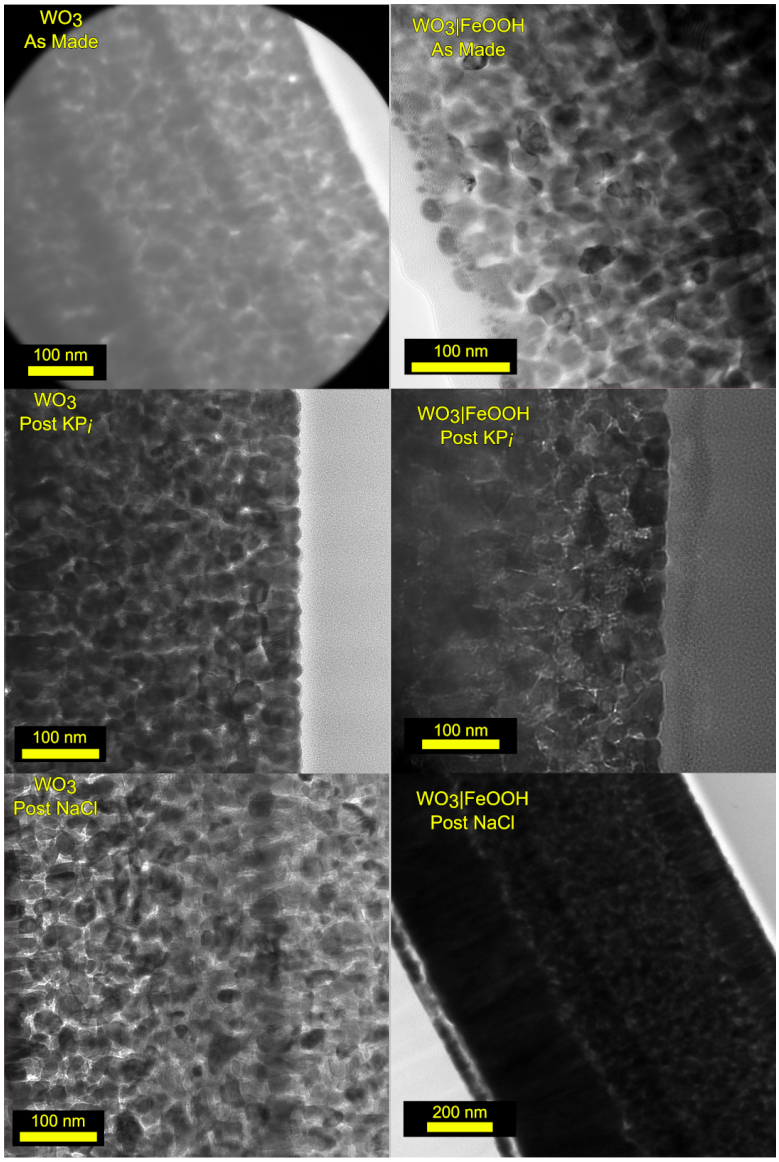

Figure B.3: Transmission electron micrographs of WO_3 and WO_3|FeOOH. Included are micrographs taken after CPC in each electrolyte. A negligible change in morphology compared to the original WO3 is seen in all cases.

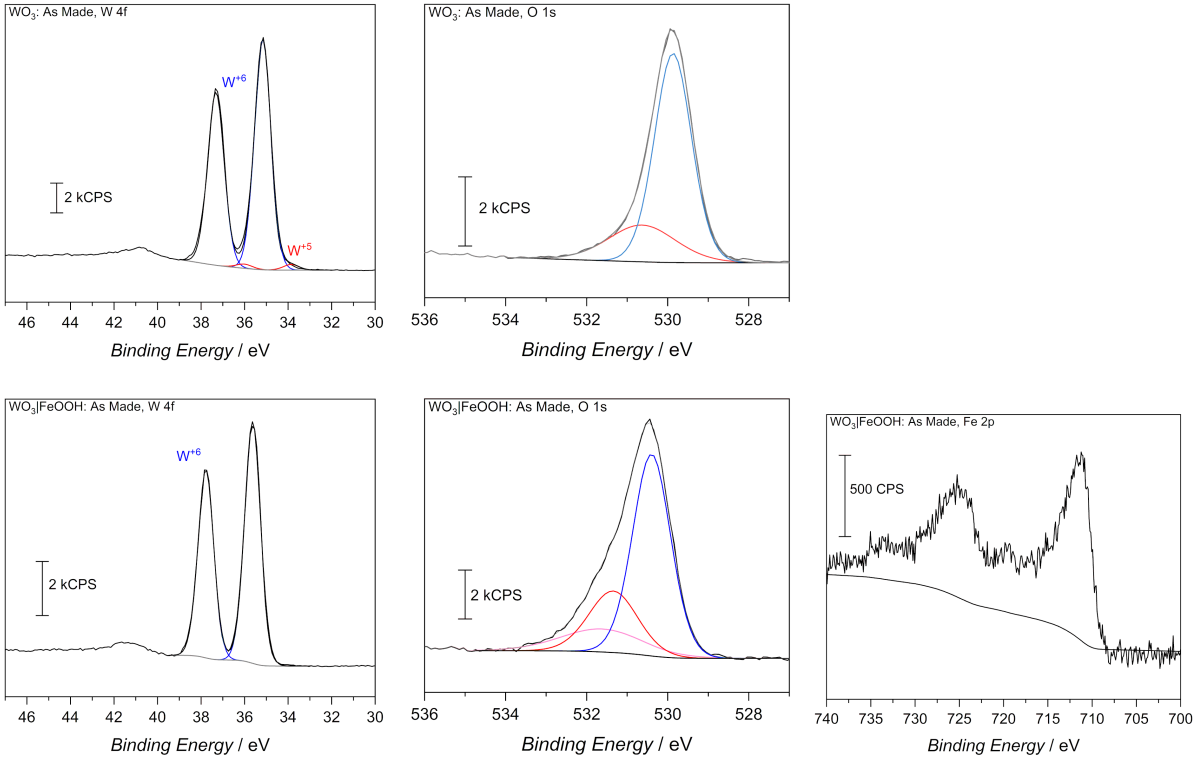

Figure B.4: XPS spectra of WO_3 as well as WO_3|FeOOH before and after CPC in the electrolytes used in this chapters work. In the W(4f) spectra, the W+5 signal can be seen in the WO3 spectrum but is missing from all of the WO3|FeOOH spectra. The conditions for FeOOH deposition are sufficient to remove surface W^{+5} species which are within the XPS sampling volume. We do not see a large decrease in photoactivity when comparing WO_3 trials against WO_3|FeOOH for the same electrolyte, indicating that the more kinetically hindered W^{+5} species deeper in the film are unaffected.

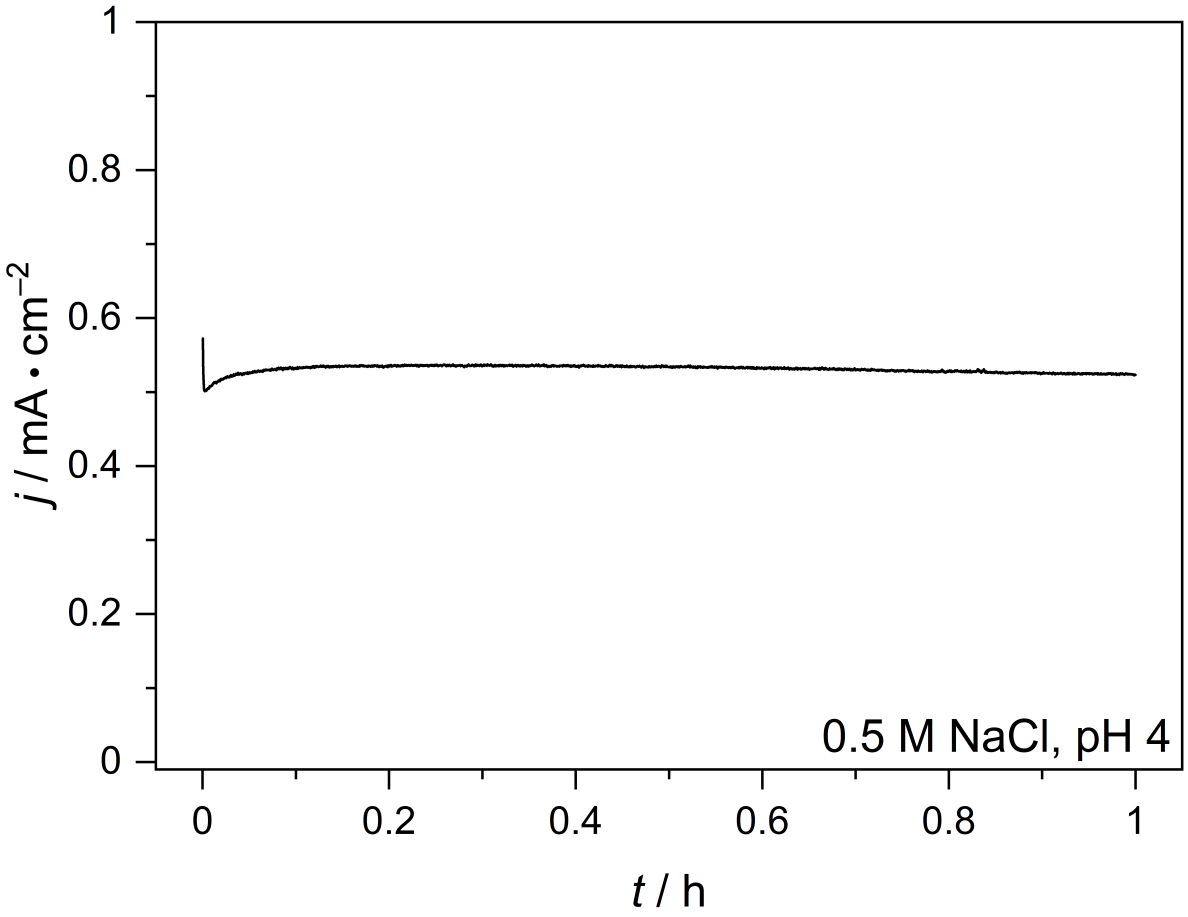

Figure B.5: 1-hour CPC of H_xWO_3 in 0.5 M NaCl, pH 4, performed in a 35 mL volume of electrolyte in the working compartment. After the CPC experiment was performed, 25 mL of the working compartment electrolyte was used measure the electrolyte free chlorine content by a starch-iodine test.

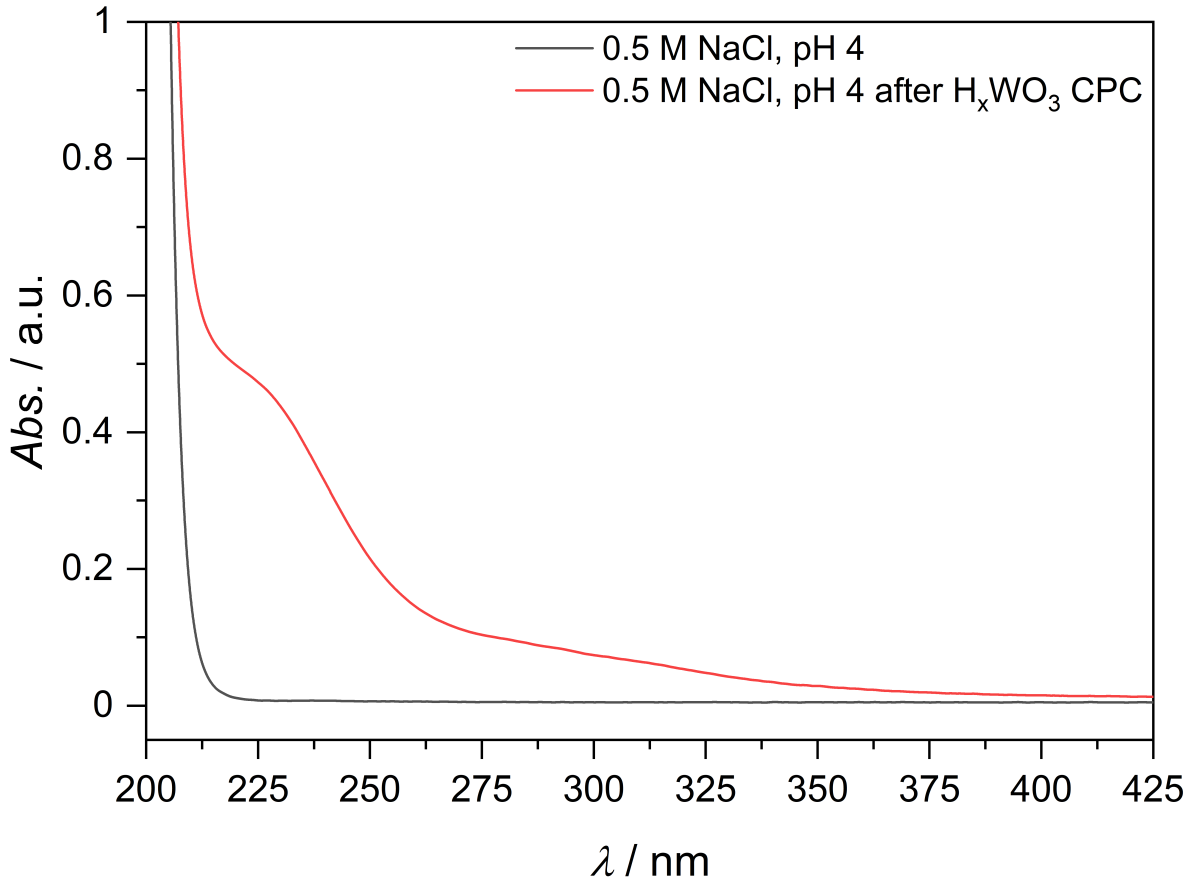

Figure B.6: The solution UV-Vis spectra of the 0.5 M NaCl, pH 4 electrolyte was taken before and after a 1-hour CPC experiment with a H_xWO_3 electrode. The UV-Vis spectrum taken after the CPC experiment shows an increase in absorption of UV light.

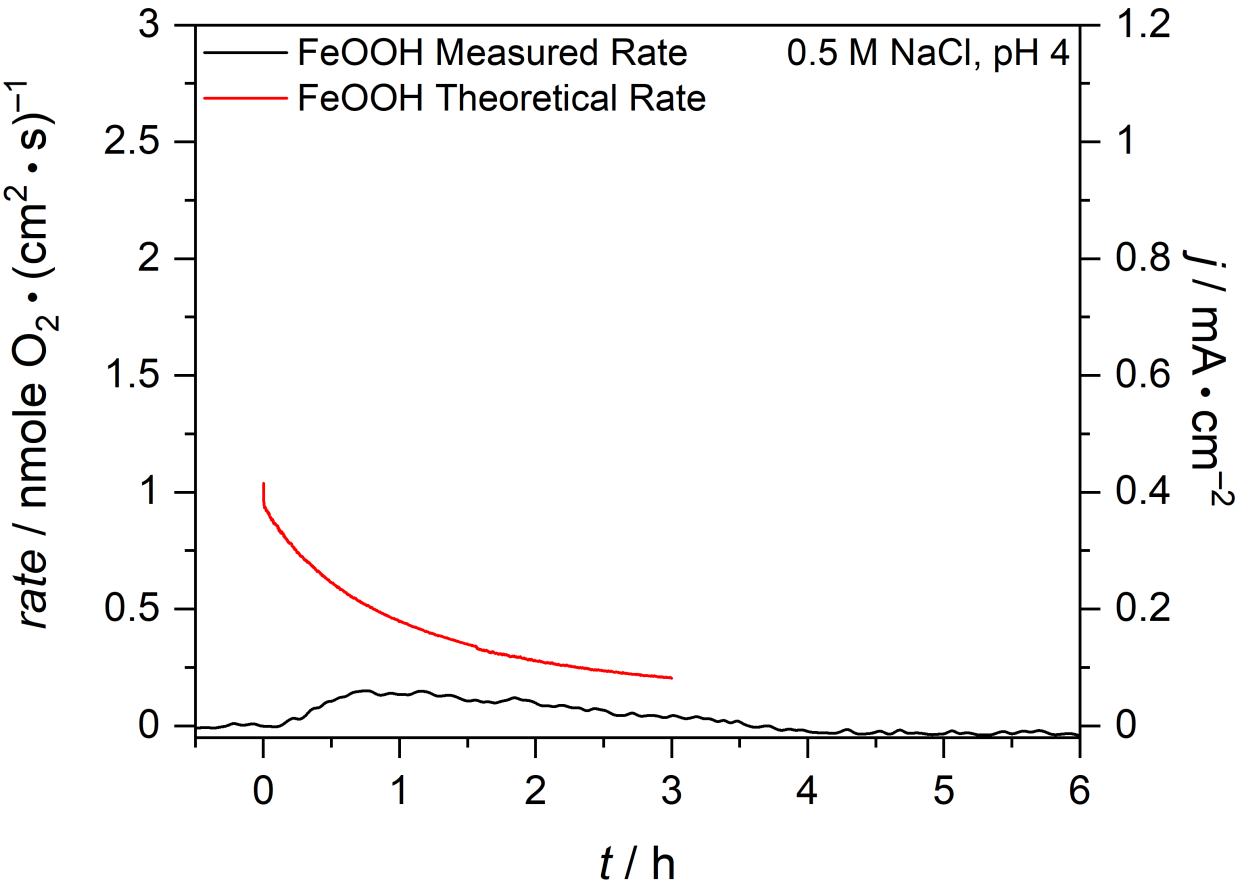

Figure B.7: CPC of FeOOH deposited on FTO in pH 4 0.5 M NaCl electrolyte. The FeOOH electrode was poised at 2 V vs RHE and was under zero illumination for the experiment.

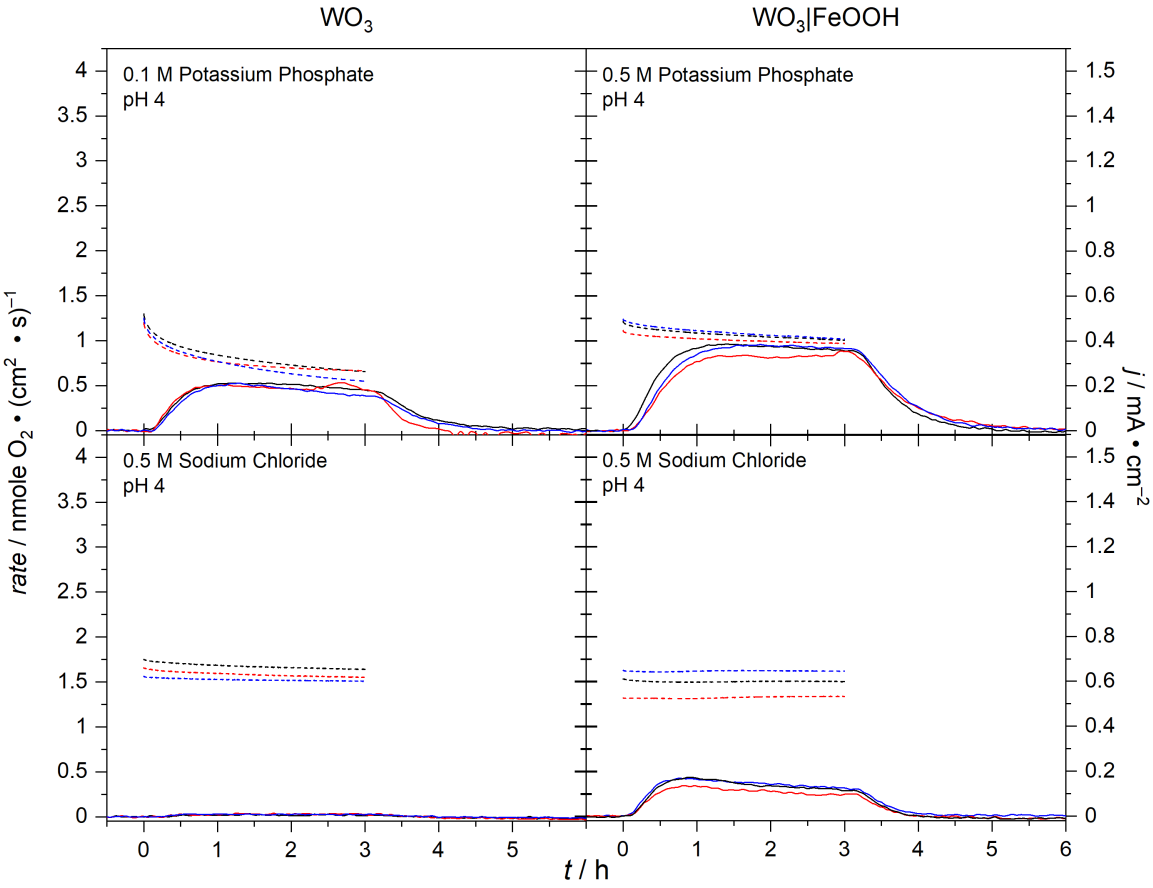

Figure B.8: Replicate experiments for Figures 3.2 and 3.3 in the chapter text. The black trace is the same data presented in the main text and is included for comparison. All experiments performed under 1-sun AM 1.5 G illumination.

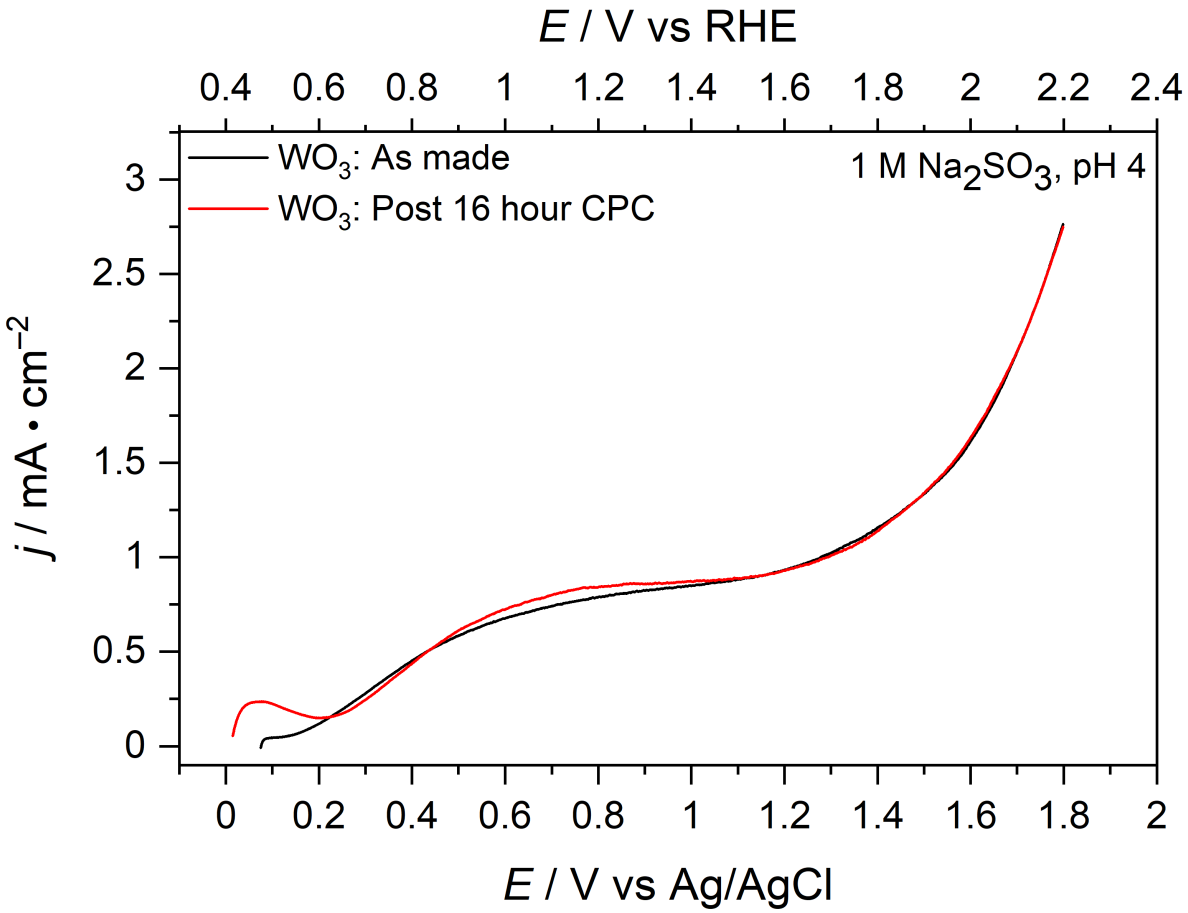

Figure B.9: LSV traces of WO_3 before (black trace) and immediately after (red trace) a 16-hour CPC experiment at 1.23 V vs RHE under AM 1.5 G illumination in pH 4 1 M sodium sulfite. The 16-hour CPC experiment is shown in Figure 3.4 of chapter text. An earlier onset for photocurrent and a slightly elevated saturated photocurrent density suggests a slight reduction of the WO_3 light absorber.

Appendix C.

Supporting Information for Chapter 4

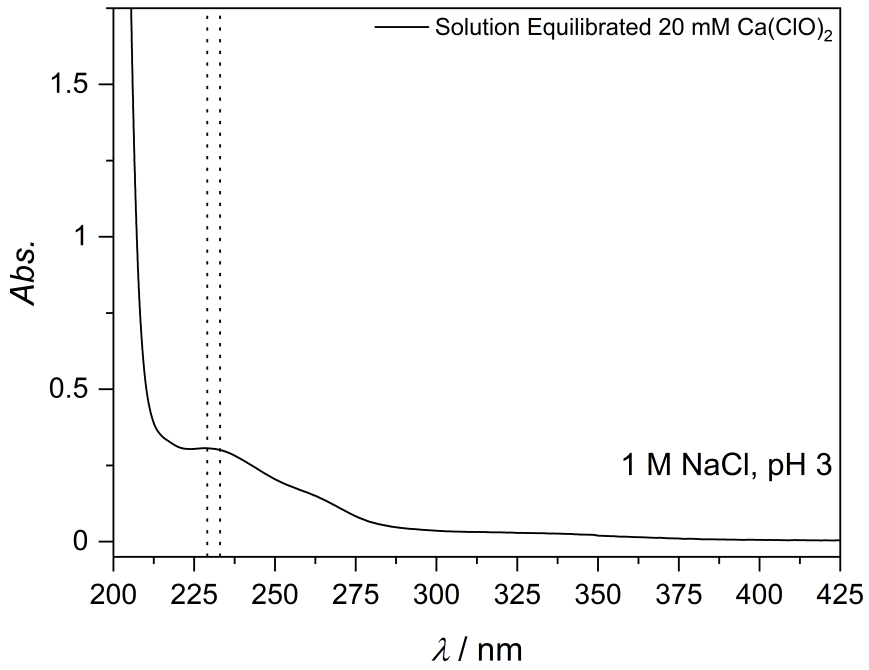

Figure C.1: UV-Vis absorbance of $Ca(ClO)_2$ dissolved in 1 M NaCl after allowing to equilibrate for forty-five minutes. Solution was set to pH 3 with hydrochloric acid after the $Ca(ClO)_2$ had fully dissolved in 1 M NaCl and again at the end of the forty-five minute equilibration time to compensate for the rise in pH due to consumption of H^+ by comproportionation of HClO and Cl^-. The vertical dashed lines show the λ_{max} for Cl_2 (λ_{max} = 229 nm) and HClO (λ_{max} = 233 nm) for reference. The UV-Vis spectrum of $Ca(ClO)_2$ in pH 3, 1 M NaCl taken immediately after dissolution of $Ca(ClO)_2$ is shown in Figure 4.3 and features a sharp peak centered at 233 nm. A broadening of the UV-Vis response and a shift of λ_{max} towards shorter wavelengths is observed here due to comproportionation of HClO and Cl^- to form Cl_2.

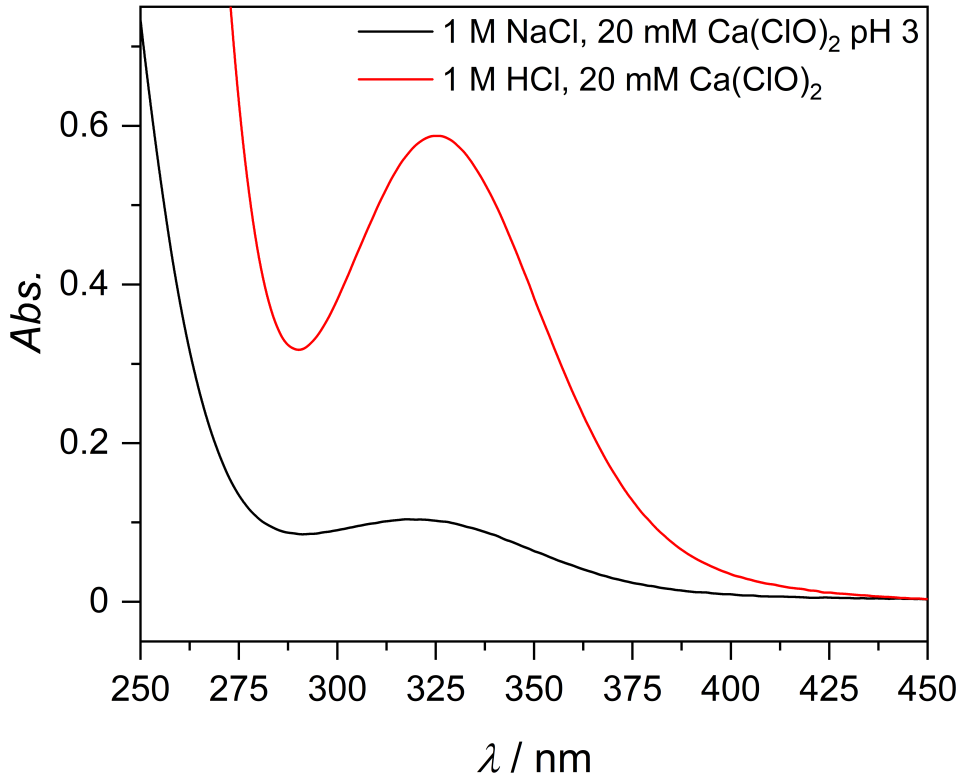

Figure C.2: UV-Vis absorbance of 20 mM $Ca(ClO)_2$ dissolved in 1 M NaCl set to pH 3 and 1 M HCl, displaying a broad absorbance ($\lambda_{max} = 326$ nm) with a tail extending past 405 nm.

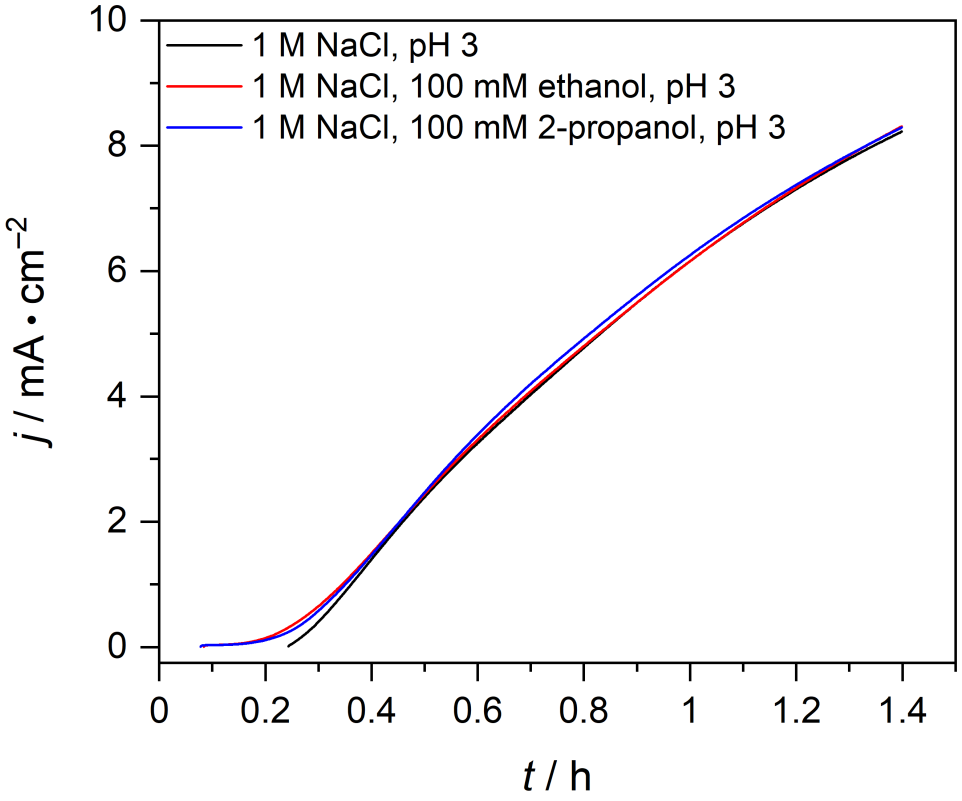

Figure C.3: Linear sweep voltammograms of H_xWO_3 in 1 M NaCl, pH 3 with and without ethanol or 2-propanol substrate. No Nafion™ was used to separate the working electrode compartment from the counter electrode compartment.

Appendix D.

Supporting Information for Chapter 5

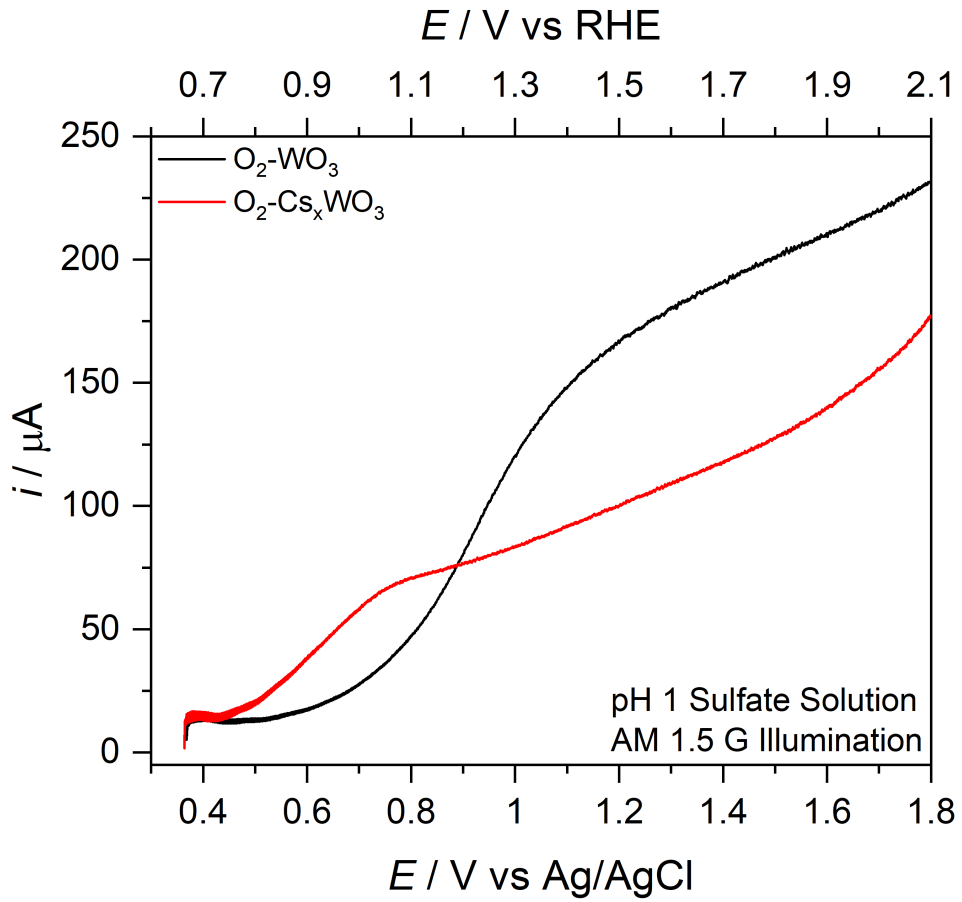

Figure D.1: Linear Sweep Voltammogram of H_xWO_3 after annealing under 100% O_2 compared against a H_xWO_3 film with 0.5% Cs^+ content, also annealed under 100% O_2. Performed in a pH 1 aqueous sulfate solution.

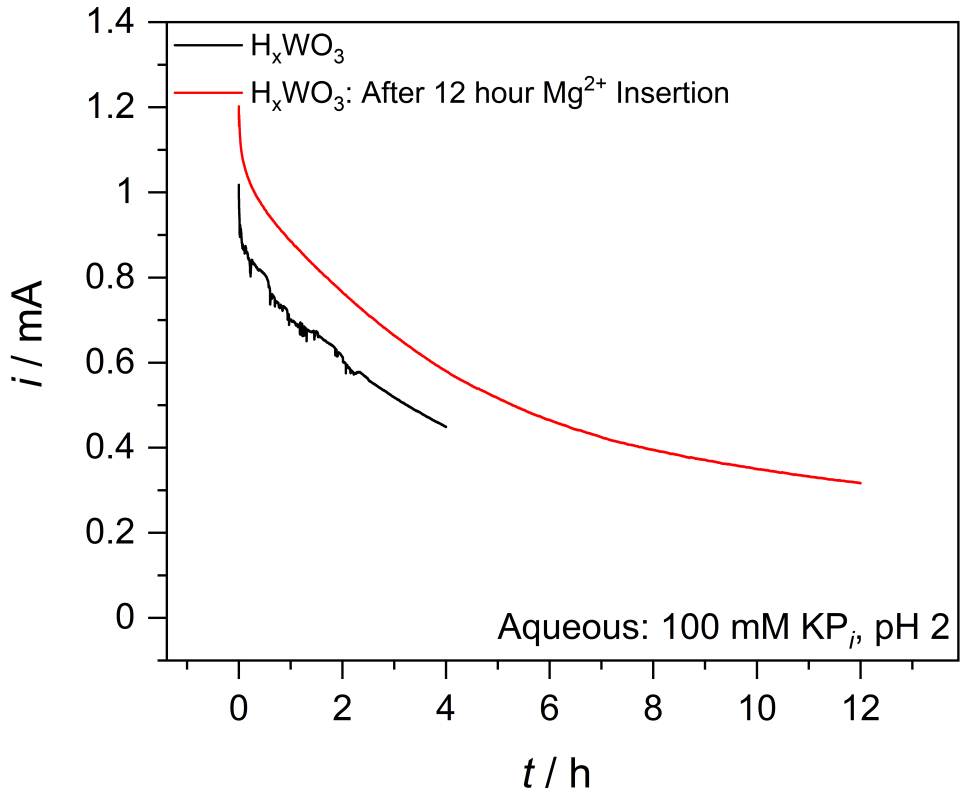

Figure D.2: Comparison of CPC behavior from H_xWO_3 (black) and H_xWO_3 (red) after galvanostatic magnesium intercalation. Electrodes poised at 0.98 V vs Ag/AgCl and illuminated by AM 1.5 G light.